UNIVERSITÀ DEGLI STUDI DI UDINE
hic sunt futura

www.uniud.it

Corso di dottorato di ricerca in:

"Informatica e scienze Matematiche e Fisiche"

Ciclo 35°

"The observational potentials of the advanced detector system of the HERMES Pathfinder mission, an assessment"

Dottorando

Dott. Giovanni Della Casa

Supervisore

Prof.ssa Barbara De Lotto

Co-supervisore

Prof. Andrea Vacchi
Dott. Fabrizio Fiore

Anno 2023

Abstract

HERMES (High Energy Rapid Modular Ensemble of Satellites) Pathfinder is a space-borne mission based on a constellation of 3U CubeSats, flying in a low-Earth orbit, equipped with a novel specifically designed detector obtained by the combination of silicon drift detectors and GAGG:Ce crystal scintillators, exploiting the "siswich" architecture. HERMES Pathfinder main scientific goal is the study of bright high-energy transients, the gamma-ray bursts, in a broad energy band (few keV to few MeV) with an unprecedented time resolution and a precise localization. The first constellation of six nanosatellites should be launched towards the end of 2023/early 2024.

The crystal scintillator chosen for the HERMES Pathfinder detector presents an intense and long lasting residual emission (afterglow) after being exposed to ionizing radiation. This phenomenon might affect the HERMES Pathfinder detectors, impairing their proper functioning. In this study the crystal afterglow has been characterized and it was verified that, in orbital conditions, the correct functioning of the detector is guaranteed.

In preparation for the nanosatellites launch, the qualification performed during the assembling of the detector and the final calibration of the HERMES Pathfinder payload at several temperature have been performed. The methods and the results obtained for the first flight models are presented in this study.

Finally, a tool was developed to study the lightcurve variability of a GRB and to identify its shortest variability in order to provide new insights on the central engine. It was tested on a large set of bursts observed by Fermi GBM. Finally, using simulated data, it is demonstrated that variability of the order of microseconds could be identified with this tool.

Contents

Introduction

The doctoral work presented in this thesis revolves around the HERMES (High Energy Rapid Modular Ensemble of Satellites) Pathfinder mission. HERMES Pathfinder is a project that aims to develop a constellation of nanosatellites, equipped with a novel specifically designed detector, to study astronomical transient sources, such as gamma-ray bursts, in the X and soft γ range. The first six units, expected to be launched in orbit towards the end of 2023/early 2024, are being developed in the context of the pathfinder mission HERMES-TP/SP. An additional unit is developed within the SpIRIT mission, also scheduled for the end of 2023. With this initial fleet the objective is to demonstrate the potential of the HERMES Pathfinder approach for the study of gamma-ray bursts. Within this phase of the project it was possible to work on both the hardware and the scientific aspect of the HERMES Pathfinder mission.

The first two chapters contain an overview respectively on the gamma-ray bursts and on the HERMES Pathfinder mission. More in details, the first chapter describes the general characteristics of the gamma-ray bursts and presents the historical steps in their discovery. The following chapter is focused in describing the HERMES Pathfinder nanosatellites and the objectives of the mission.

The first aspect of my direct contribution discussed in this thesis, in chapter 3.1, is a study conducted to characterize the GAGG:Ce scintillation crystals. The detector installed onboard the HERMES Pathfinder nanosatellites exploits the "siswich" architecture, consisting in coupling a silicon detector with a scintillation crystal. To fulfill the requirements of the mission the choice for the silicon detector fell on the silicon drift detector, while for the scintillation crystal the best candidate is the GAGG:Ce ($Gd_3Al_2Ga_3O_{12}$:Ce, Cerium-doped Gadolinium Aluminium Gallium Garnet), a novel inorganic scintillator, with fast response, high atomic number and high light output per keV compared to other scintillators with similar densities (e.g. BGO). About the GAGG:Ce, it has been observed that following its exposure to ionizing radiation, an unusually intense and long-lasting (even for several days) residual emission (afterglow) is produced by the crystal.

The presence of energetic charged particles, trapped in the Van Allen belts, along the predicted orbit for the nanosatellites leads to the need to verify that the current generated by the afterglow in the detectors does not compromize the correct functioning of the HERMES Pathfinder electronics. To improve the results obtained in a previous campaign (Dilillo et al., 2022), a new one was planned, with the construction of a sophisticated experimental apparatus and the development of an enhanced empirical model to describe the mechanism underlying the residual luminescence. This model was then applied to the HERMES Pathfinder orbital worst case scenario. The results obtained proved that there should be no critical situations for the HERMES Pathfinder detectors.

My second contribution described in chapter 3.2, is again related to the hardware aspect of the mission, in particular to the calibration tests performed on the HERMES Pathfinder detector unit. There are two stages of calibrations that are carried out: the first phase verify the functionality of the HERMES Pathfinder detector after each step of the assembling of the detector system, when it is still possible to apply modifications, while the second phase is focused on the performance of the fully assembled payload at several temperatures. This knowledge is necessary before proceeding to the environmental tests (e.g. vibration test) to understand how these affects the detector, and also to eventually figure out the causes of anomalies in the observations once in orbit. The analysis of the data acquired using a pulser signal and radioactive sources required the development of a software, that calculates the gain and offset of the electronic (called X-mode calibration) and the effective light output (S-mode calibration) for each channel. This work led to the publication of [49].

The last argument that I have embraced during this thesis work, described in chapter 3.3, concerns the scientific objective of the HERMES Pathfinder mission, the study of gamma-ray bursts with an unprecedented timing capability, crucial for HERMES objectives like GRBs localization or Lorentz invariance violation testing. The attention was put on the development of a tool to study GRBs variability, searching for the minimum timescales (microvariability) over which it can be observed. Once the method was defined, it was applied on a large set of bursts detected by Fermi GBM to obtain a good statistic and individuate general behaviours, and compared to the results obtained with the method developed by Golkhou et al. (2015), provided by doctor N. R. Butler. For the cases in which the redshift is available, the study was extended with a comparison between the microvariability calculated in the source frame and other quantities like the isotropic energy. Finally, considering HERMES Pathfinder improved time resolution compared to the satellites actually active, it was successfully verified that a variability of the order of microseconds could be identified with the method developed.

Acknowledgements

All along my doctoral work I had the opportunity to interact and work with many incredible people, despite the outbreak of a pandemic, whom I must thank for their precious help and support. First of all my "ex-supervisor" Andrea Vacchi, who guided me through this adventure, and helped me to increasingly take the initiative. I thank also my co-supervisor, Fabrizio Fiore, who offered me the opportunity to work for the HERMES Pathfinder project, and for his wise guide in the study of GRBs.

I must say thank you to my doctoral fellows, Giuseppe Dilillo, Daniela Cirrincione, Marco Baruzzo, Riccardo Crupi, Michele Palatiello and Marco Citossi whom welcomed me among them in Udine, and became very good friends, always available when needed.
This doctorate offered me the opportunity to work directly on the HERMES Pathfinder nanosatellites, and encountering in this way Riccardo Campana, Ezequiel Marchesini, Fabio Fuschino, Evgeny Demenev and Yuri Evangelista. They all contributed to my growth in this work environment, and taught me a lot about the hardware aspect of the HERMES Pathfinder.
Thank you to Simone Monzani, Giovanni Pauletta, Alberto Sabatini and Diego Cauz, who contributed to the realization of the experimental layout for the GAGG:Ce characterization. I also thank Barbara De Lotto, who accepted to become my supervisor for the last part of my work.
I also had the opportunity to discuss about the microvariability with Nathaniel R. Butler, who provided me very useful informations for my microvariability work.

Last but not least, I must thank Nicola Zampa. He mentored me with much patience and commitment through the GAGG:Ce characterization work, helping me in the organization and the analysis of this work. His advices have always been crucial to me, and I am very thankful for having the opportunity to work with him.

To all of you (and to those that I forgot to cite, I sincerely apologize for that) really, really thank you !

Chapter 1

The science of gamma-ray bursts

The study of the universe and the phenomena happening in it has always fascinated the human minds, from the first civilizations, when it inspired many religions and cults, up to today, with human beings being sent into space and more and more sofisticated instruments constructed both to explore the Universe from the Earth or directly from the space. Everyday new discoveries are made, like the first gravitanional wave or the first image of a black hole. And it will keep amazing the human species with new goals to achieve like new space voyages, the first human beings on other planets, maybe even the colonisation of new planets, the discovery of new phoenomena in the Universe.

One of the most recent and interesting chapter in the study of the Universe is related to Gamma-Ray Bursts (GRBs), the main subject of this work.

Gamma-Ray Bursts are the most luminous events (more than $10^{53}(\Omega/4\pi)$ erg released) in the Universe and very likely the signature of the birth of stellar mass black holes. Since the GRB science is quite recent (more or less 50 years old), there are many things that are still unknown and many theories proposed that still need a confirmation or to be improved, as it will be seen.

The GRB emission can be divided in two different phases. The first one is called prompt, it can last from less than a second to even tens of minutes (but generally less than a minute) and corresponds to an initial burst of high energy emitted by an ultra-relativistic jet. The second phase is the afterglow, a long-lasting multiwavelenght fading emission due to the interaction of the jet with the ambient medium, that can last days or even months depending on the energy band observed.

1.1 Observation of GRBs through decades

Gamma-Ray Bursts were detected for the first time in 1967 (GRB 670702) by the Vela satellite network, a group of american military satellites (Klebesadel, Strong and Olson, 1973). This first detection was totally accidental, since the aim of the Vela satellites was to look for any nuclear activity from the URSS, in the context of the Cold War. However, because of the casuality in time and position of the transient event, it is impossible to predict where and when the next one will appear. For the following 30 years, despite few missions developed from different countries that brought to the first Inter-Planetary Network (IPN), no important discoveries were made. The reason is that the sources were vanishing too fast for those instruments to reposition, and since gamma rays are hard to focus it was difficult to obtain clear images and positions.

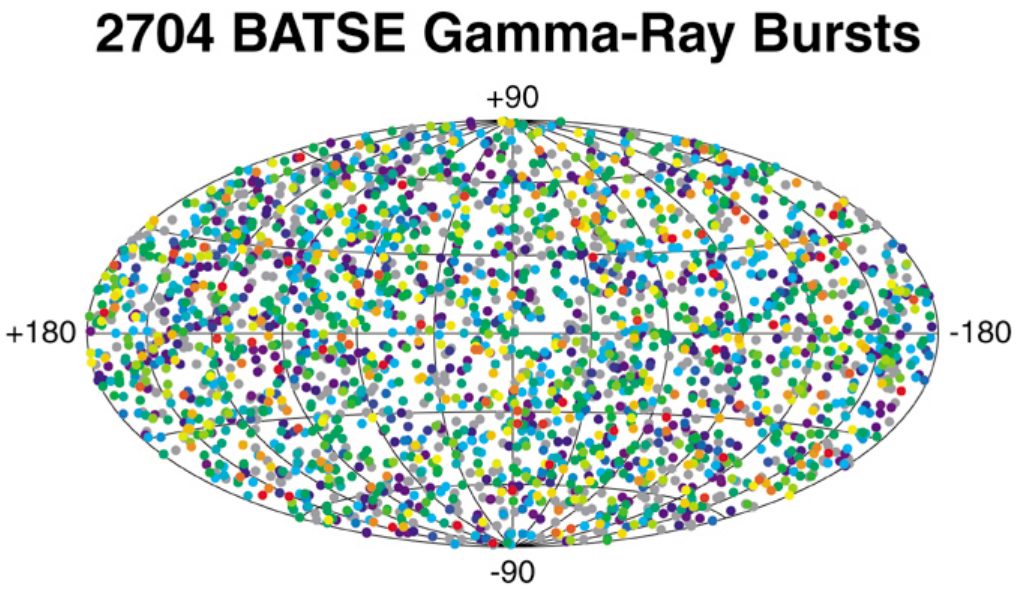

Figure 1.1: Sky map of the GRBs detected by BATSE [1].

The advent of the BATSE (Burst And Transient Source Experiment) telescope (1991-2000), which was one of the four instruments on board of the Compton Gamma-Ray Observatory (CGRO), allowed to finally make important progresses. For example, up to that moment, many theories about the GRBs presumed a galactic origin. BATSE played an important role in supporting the theory of the extragalactic origin. This was a consequence of the isotropic distribution of the thousands of GRBs seen by BATSE during its period of activity, thanks to the more advanced technologies that allowed the telescope to find about 1 GRB/day. The

high number of GRBs seen (more than 2700 at the end of its journey, Figure 1.1) was made possible thanks to the 8 detector modules pointing in different directions, that would give a nearly full sky coverage. Each one of these modules used crystal scintillator (NaI, sodium iodide) coupled with a photomultiplier tube. This allowed to study the GRB emission spectrum in an energy range going from 20 keV to 8 MeV. The isotropy of GRBs was an important proof against the galactic origin, since the Milky way is very thin. Consequently we would expect a distribution of GRBs more important along the disk of the galaxy, instead of isotropic. Actually, there were already some evidences of this isotropy found precedently by the Venera satellites. However this was still not enough to determine the extragalactic origin of GRBs, since they were still only looking in the gamma energy band.
Another important discovery made by BATSE is the division between short and long GRB, again possible thanks to the high number of GRBs detected that allowed to finally have a solid statistic of the phenomena.

The arrival of BeppoSAX (Satellite per Astronomia X, Beppo in honor of Giuseppe Occhialini), a dutch/italian satellite launched in 1996, allowed to make a further step ahead. Beyond the broad energy band that it was able to observe (0.1-300 keV), Beppo's contribution was crucial since it could observe in the X energy range. Thanks to its two low energies telescopes LECS (0.1-10 keV) and MECS (1-10 keV), it was able to measure for the first time the X counterpart of a GRB (GRB970228 [2]), the X-ray afterglow. In concomitance with this crucial discovery, another team of scientists observed the afterglow in the optical energy range for the same GRB, using the William Herschel Telescope (WHT) situated in La Palma [3]. The discovery of the X-ray afterglow allowed indirectly to measure the distance of the GRB, searching for it in the X-ray band with better precision thanks to the specific instruments of BeppoSAX, compared to what was possible with the previous gamma instruments [4]. In this way, other telescopes could after point at that same position and measure the distance (or redshift), observing the host galaxy at optical and longer wavelenghts. This led to the first measured redshift a few months later, for the GRB970508, following a detection from Beppo-SAX [5]. The increasing number of redshift measured confirmed the extragalactic origin of the GRB, ending the discussion about the distance of GRBs, that culminated in the Great Debate of 1995 (opposing D. Lamb, galactic origin, to B. Paczynski, extragalactic origin).

The following important mission for the observation of GRBs is the Swift Gamma Ray Burst Explorer, operating since 2004. This satellite is composed of three main telescopes: Burst Alert Telescope (BAT, 15-150keV), X-Ray Telescope (XRT, 0.2-10 keV) and UltraViolet / Optical Telescope (UVOT, 170-600nm) (see Figure 1.2). The collaboration of these instruments with each other is fundamental

to provide rapid identification and multiwavelenght follow up of GRBs and their afterglow. The strategy adopted by Swift is to use BAT to initially locate a burst and trigger an autonomous spacecraft slew to repoint in the correct direction in less than a minute (but this can also happen after receiving the position of a GRB, identified by another satellite, from the TDRSS, an american network of comunication satellites and ground based stations). This allows the other two telescope to properly observe the afterglow of the GRBs, since the early stages [6]. Thanks to the higher level technology of Swift, like the use of a CdZnTe (CZT, a semiconductor) detector array and the larger sensitive area, compared to the previous telescopes, it has been possible to identify GRBs at high redshift up to z~8.2 using spectroscopy for the GRB090423 and z~9.4 using photometry for GRB 090429B [7]. These are still, up to today, the highest redshift GRBs detected. Swift was also very important in observing for the first time the afterglow of a short GRB. Before 2005, the X and optical electromagnetic counterpart for several long GRBs had been found, but never for a short one. This first short GRB afterglow observation allowed also the first redshift measurement for this type of GRBs [8]. Swift has since then become fundamental in obtaining evidences about GRBs progenitors, by observing the GRBs host galaxies also for the short ones since the afterglow was finally observable, and studying the interaction of the blast with the surroundings. It was observed that while the long GRBs are usually found in region with high star formation rate, the short one are instead localized in galaxied with low star formation rate. This led to the two progenitor models presented previously.

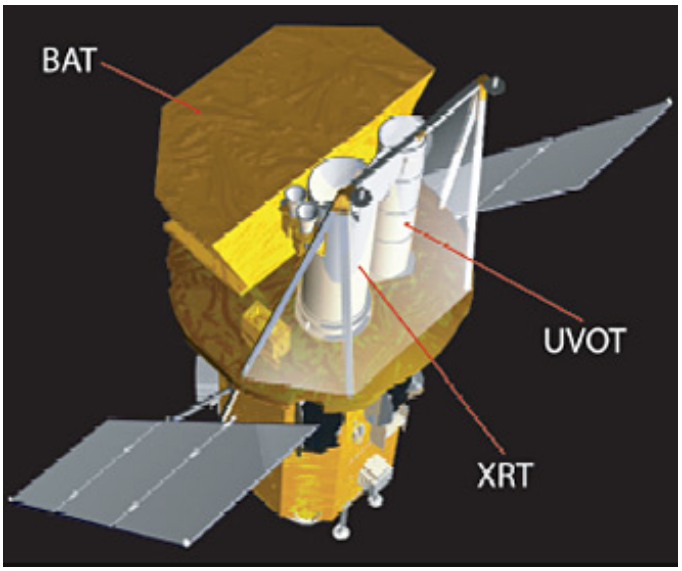

Figure 1.2: The three Swift telescopes.

Finally, the Fermi Gamma-Ray Space Telescope is a satellite observatory, launched in 2008, that covers a very large energy band going from 8 keV to 300 GeV. This is done thanks to the two telescopes on board: the Large Area Telescope (LAT) and the Gamma-ray Burst Monitor (GBM). While LAT is a pair production instrument, GBM is based on scintillators of NaI (sodium iodide) and BGM (Bismuth Germanate). This means that GBM covers the lower part of the band (from 8 keV to $\sim$ 40 MeV); LAT instead is able to detect gamma-rays in the interval between 20 MeV and more than 300 GeV. The working principle is different from all the other instruments seen up to now. The LAT instrument is composed of: a plastic anticoincidence detector that covers the rest of the telescope, allowing photons to pass freely but emitting a flash of light when a charged cosmic ray tries to enter the telescope; a tracker made of thin tungsten foils and of layers composed by silicon strip detectors, where the gamma-ray is converted in a pair electron-positron (tungsten) that is then tracked thanks to the creation of ions in the silicon strips; and a calorimeter of cesium iodide (CsI) to measure the total energy deposited. There is also a data acquistion system that uses all the information of the three detectors (anticoincidence, tracker and calorimeter) to form a trigger [9].

Thanks to this high energy instrument, it has been possible to find a new power-law component in the spectra of some GRBs, that was unseen for pre-Fermi GRBs, since none of the instruments reached these high energies. Moreover, Fermi played a crucial role in the discovery of the GRB170817A (Figure 1.3), which is the electromagnetic counterpart of the gravitational wave GW170817, detected by Virgo and LIGO about 1.7 s before [10].

There are also other missions that played or are still playing an important role in the study of GRBs, both from the ground (like MAGIC, HESS) and from the space (HETE2, AGILE), collaborating with the mission presented in this section. MAGIC has assumed a major role in the observation of GRBs at very high energies (VHE, $> \sim$ 300 GeV) with its two telescopes of 17 meters diameter situated in La Palma. These two telescopes operate between 25 GeV and a few tens of TeV, a lot higher than the majority of the other telescopes. MAGIC, together with Swift and Fermi, saw the most energetic GRB ever recorded, GRB190114C [11]. The photon observed by MAGIC reached for the first time energies of the order of teraelectronvolt, opening to new opportunities of scientific discoveries.

Right now, Swift and Fermi are still active in orbit, but are beginning to be old instruments. New technologies and ideas have been developed in the last 15 years, since Fermi launch. And it is even more important now, that the multimessenger era has arrived and a connection between gravitational waves and short GRBs has been identified, to be ready to observe GRBs, covering the largest energy

range possible with the best instruments at disposal. In this context, the HERMES Pathfinder project [12], described in the following chapter, has been developed and, hopefully, will be ready to give its contribute starting from 2023.

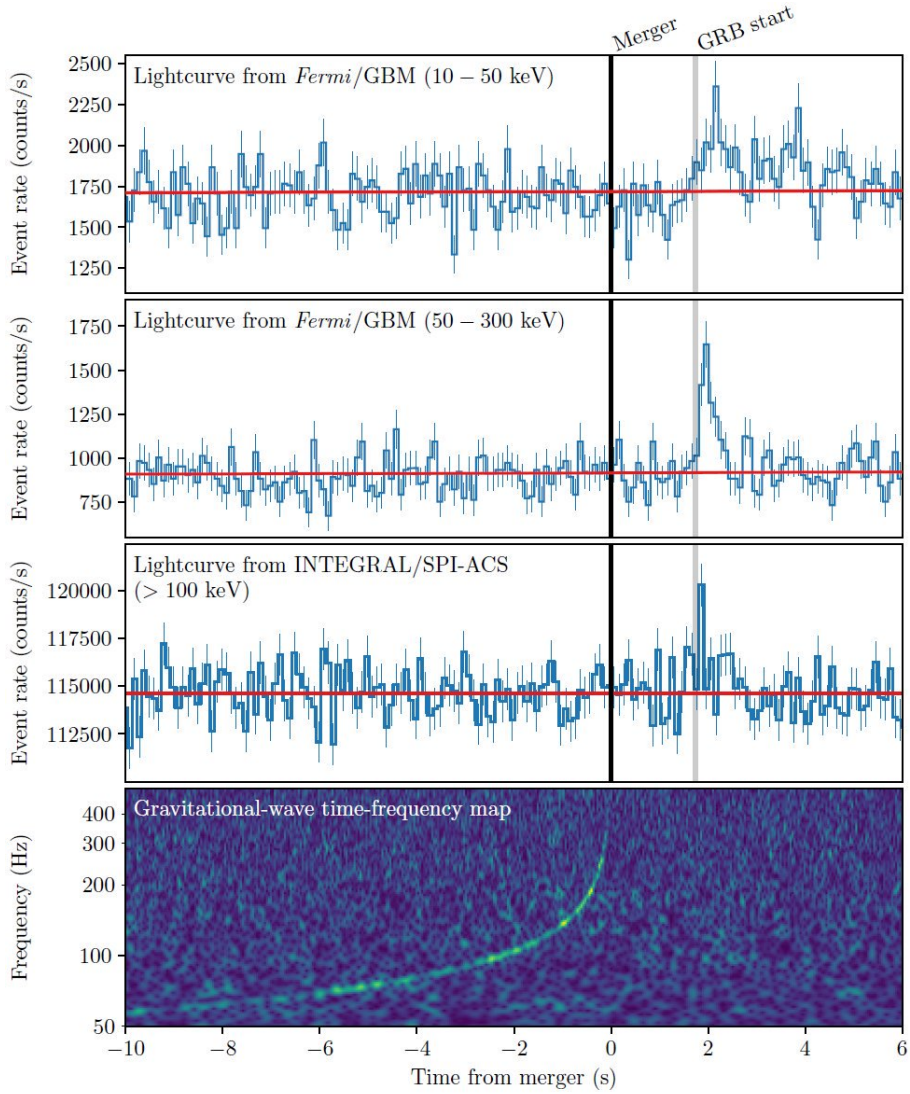

Figure 1.3: Observation of the GRB/GW 170817 by different detectors (credits LIGO).

Another upcoming mission that will play an important role in future observations is SVOM (Space-based multi-band astronomical Variable Objects Monitor) [13][14]. The Sino-French project, expected to be launched in 2023, will survey the sky searching for GRBs in the optical and X-ray band with the four instruments

(ECLAIRs and GRM for the prompt observation on a energy range between 4 keV and 5 MeV, MXT and VT for the follow-up observation respectively in the X and optical energy band) on board of the SVOM satellite, but also with a large number of ground telescopes (see Figure 1.4). At ground level, it is important to mention another project for gamma-ray observation in construction, the Cherenkov Telescope Array (CTA). With more than 100 telescopes located in two sites, one in the northern hemisphere and one in the southern one, it will be be able to observe the full night sky, with a broad energy coverage (from 20 GeV to 300 TeV) thanks to different types of telescopes employed [16].

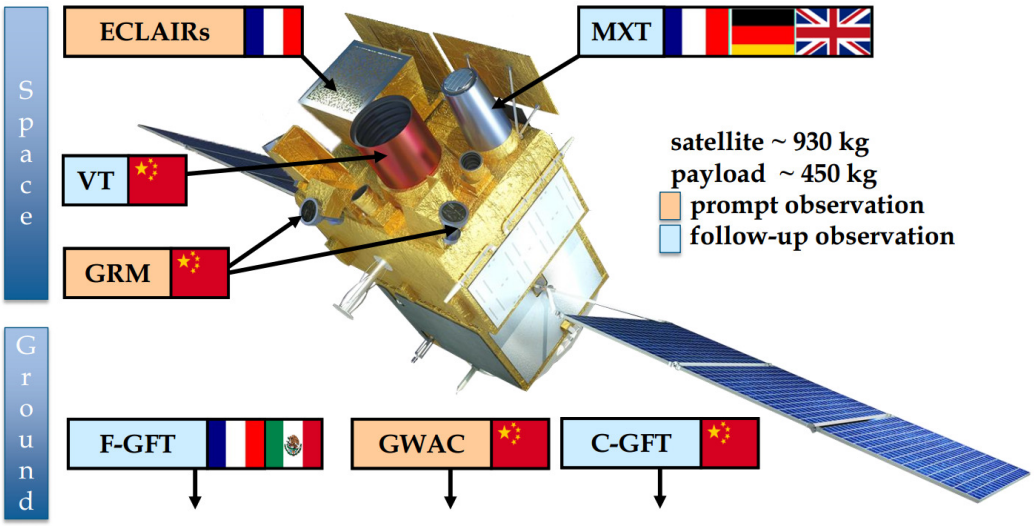

Figure 1.4: Scheme of the SVOM instruments, both space and ground level. [15].

Looking further ahead in time to the next decade, the THESEUS (Transient High-Energy Sky and Early Universe Surveyor) mission will hopefully play a major role [17][18]. Studied by ESA in 2018-2021 as candidate M5 mission, it has been resubmitted for ESA M7 call. The aim of the THESEUS is to study the Early Universe by detecting high redshift GRBs and to identify the electromagnetic counterparts to sources of gravitational waves, that will be detected more frequently in the future by the new facilities in development. It will be equipped with three instruments, to observe infrared (InfraRed Telescope, IRT), soft-X (Soft X-ray Imager, SXI) and X/Gamma rays (X/Gamma-rays Imaging Spectrometer, XGIS), and with fast slewing capabilities in order to provide prompt identification of the GRBs, with high precision ($\sim$ arcsec) on the localization.

There are many more missions that are being studied and developed, but it would be too long to go through all of them.

1.2 Prompt phase

The prompt phase represents one of the most compelling question about GRBs under many aspects. The lightcurve of the prompt phase is very different from GRB to GRB in both duration and number and shape of peaks of emission, making it difficult to define a general model. Some can present a very high variability, which is one of the aspect studied in this work and will be described more deeply later, others can have two peaks separated by a long quiet phase. Generally the peaks show a fast rising phase, and a slower decay phase. Some example of lightcurves are showed in Figure 1.5.

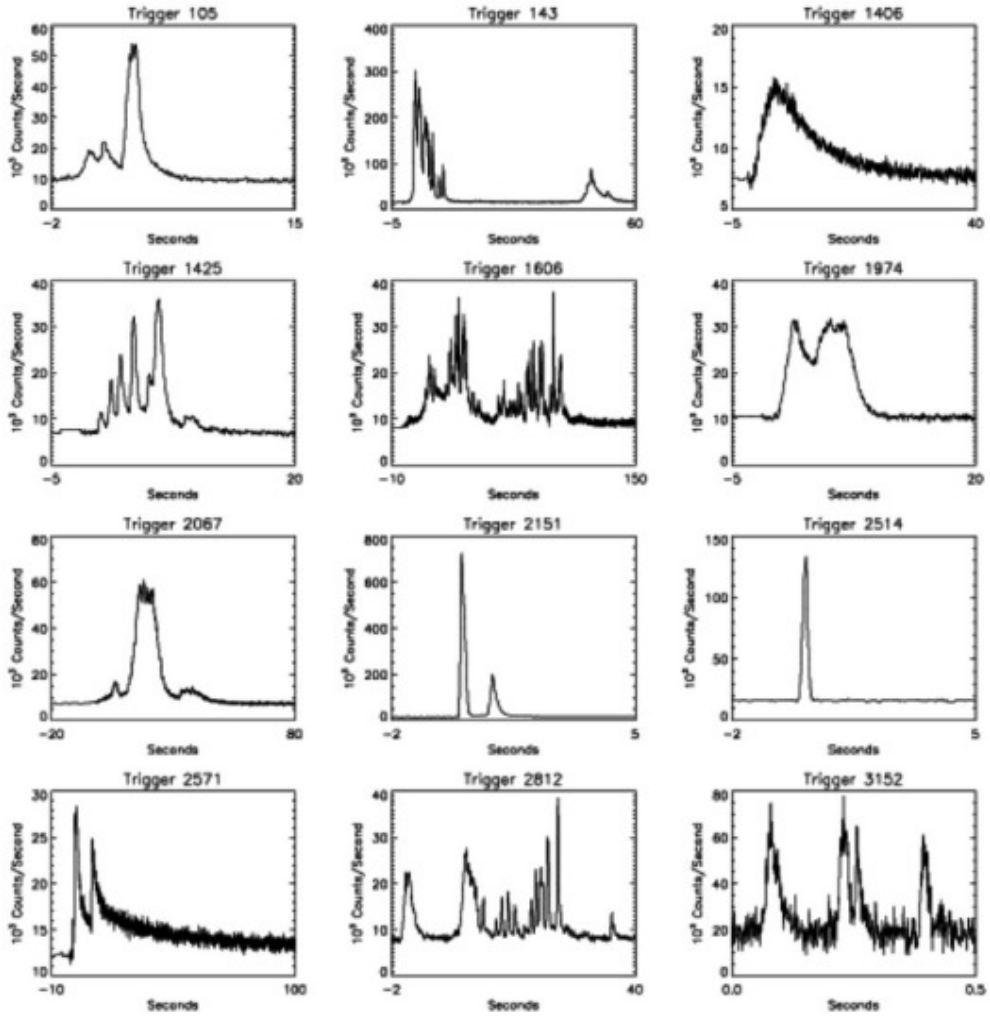

Figure 1.5: Examples of GRBs lightcurves (Fishman & Meegan, 1995) showing the large variety of GRBs

From the spectral point of view, the prompt radiation is mostly non-thermal emission. Altough they are mainly considered for their emission in the gamma energies and only this part has been known for a long time, GRBs emission covers a large part of the electromagnetic spectrum, going from GHz radio waves up to TeV gamma-rays, this new upper limit recently discovered. The energy peak can vary from a few keV for fainter GRBs up to the MeV region for the brighter ones. It is not straightforward to fit the spectrum, especially because it depends on the characteristics of the detector (band width, collecting area, ...). Traditionally, the spectra has been fitted with a smoothly-joined broken power-law, known as Band function [19]. However a few exceptions have been found, for examples for GRB 090902B and GRB 090510, that not only present a more narrower Band function as the time bins get smaller, but also show a power-law component, with positive slope, for higher energies. This brought to the conclusion that the spectra of a GRB can be made of three elemental components (Figure 1.6):

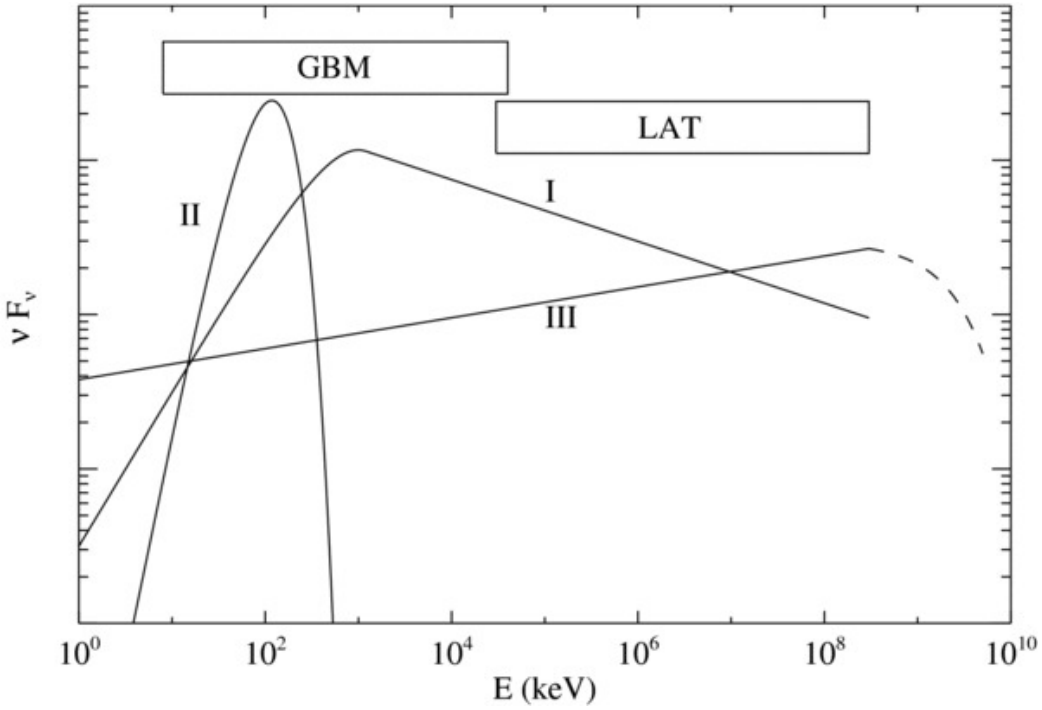

Figure 1.6: Representation of the three GRB spectral components. I:Band-function, II: Black-Body, III: Power-law [20].

- a Band-function (Band) component, that extend over several decades of energy, that must have a non thermal origin;

- a quasi-thermal component, around the Mev region, that can be approximated with a black-body(BB) (or several black-body) emission.
- a power-law (PL) component that has a positive slope, and extend to very high energies [20].

All the combinations of these three components are theoretically possible, however only a few of them have been seen. The majority of the GRB spectra are well described by the Band alone, sometimes also the combination of BB and PL provides good results. Actually, there is another particular GRB presented in [20], GRB090926A, which is better investigated in [21]. The particularity of this GRB is double: first it confirms the existence of the combination of the Band function with a PL; second it show a new feature, an exponential cutoff at the end of the PL, as it can be seen in Figure 1.7. Also, it shows another common feature of the GRBs observed by Fermi, a delay between the observation of GBM and LAT.

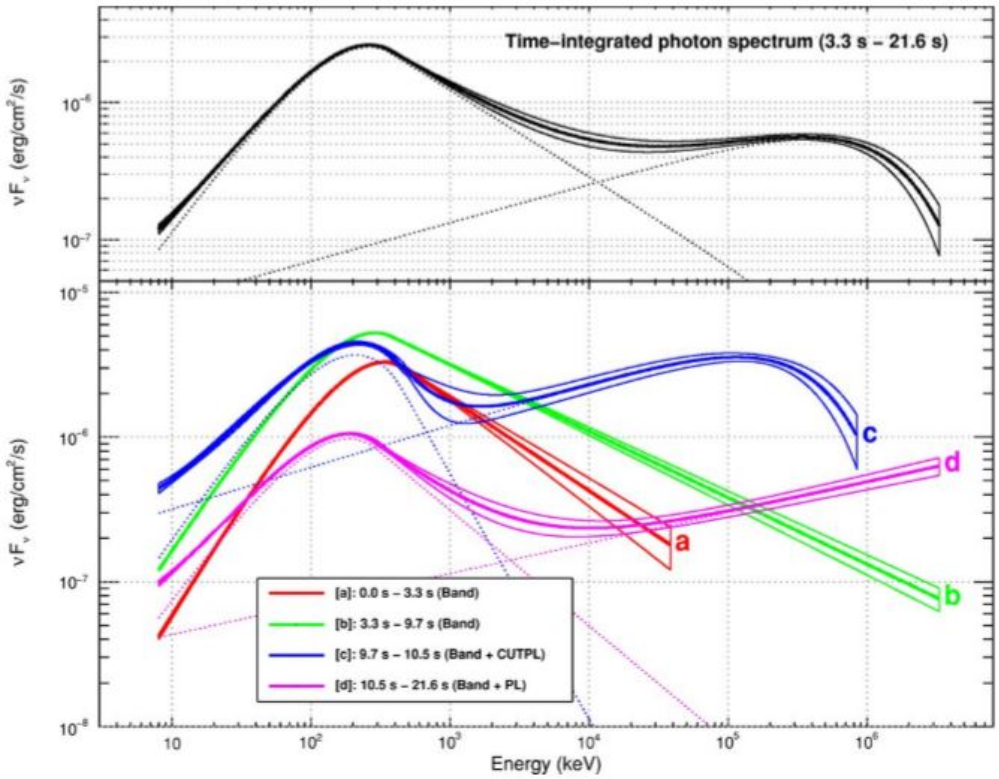

Figure 1.7: GRB 090926A spectrum observed by Fermi [21].

This exponential cutoff has also been seen in other GRB immediately after the peek (GRB 100724B and GRB 160509A) [22]. The analysis reported here

proves how complicate it is to define a general rule that defines the GRB spectrum behaviour.

What can generate those components ? As it is pretty clear at this point, there is not a unique possible answer. Many theories and models have been developed and proposed, and are still object of long discussions. It is not the scope of this work to go through all of them, so only a quick look will be given (see also Table 1.8). For the Band component, it has already been said that it must be due to a non-thermal process, since it can extend for six to seven orders of magnitude. Relativistic electrons, that are energized either by internal shocks or by magnetic dissipation, could be the answer. They are expected to radiate via synchrotron emission (Meszaros & Rees, 1993). However, many observations have found discrepancies between the keV-MeV spectral shape of the detected sources and the expected synchrotron spectrum. Recent results found that synchrotron radiation in a regime of moderately fast cooling could solve this problem [23].
For the BB or quasi-thermal component, the main candidate indicated for this emission is the photosphere, where the photons are emitted for Compton scattering, and it was predicted in one of the first model used to describe the central engine, the fireball model.

FIREBALL VARIANTS

Condition	Fireball Properties
$\sigma \lesssim \sigma_{c1}$.....	Kinetic-energy dominated, strong shocks possible
$\sigma_{c1} < \sigma \leq \sigma_{c2}$.....	Poynting dominated, MHD does not break globally, but may break locally, no strong shocks
$\sigma_{c2} < \sigma \leq \sigma_{c3}$.....	Completely Poynting dominated, MHD breaks globally, no strong shocks, baryon electrons dominant
$\sigma > \sigma_{c3}$.....	Completely Poynting dominated, MHD breaks globally, no strong shocks, baryon electrons negligible

Figure 1.8: Summary of different scenarios possible for the fireball model, in function of a parameter σ which represents the ratio between luminosity of the cold component and the hot component of the fireball. More details can be found at [24].

1.3 Afterglow phase

Contrary to what it would be legitimate to expect, since it was discovered few decades after the prompt emission, the afterglow emission is actually known a lot better.
The early afterglow (< 10hours) is characterized by: a steep decay phase (steeper than t^{-2}), which is the tail of the prompt emission, a plateau phase (slope > -0.5), a normal decay phase (t^{-1}), and a late steep decay phase(t^{-2} or steeper). Over all these phases, X-flares may appear, due to a restart of the GRB central engine. Not all GRBs afterglows show these features.
The late afterglow (> 10 hours) is generally well fitted by a broken power-law, with different behaviours depending on the observed band. While the optical emission is initially a powerlaw with exponent ~ -1 and after one day it become steeper (-2), the radio emission is initially growing and after ten days start to decline. The synchrotron radiation mechanism in external shock provides a good description of late time (t > 10hr) GRB afterglow radiation from radio to X-ray frequencies. For the early afterglow it is more complicated [25].

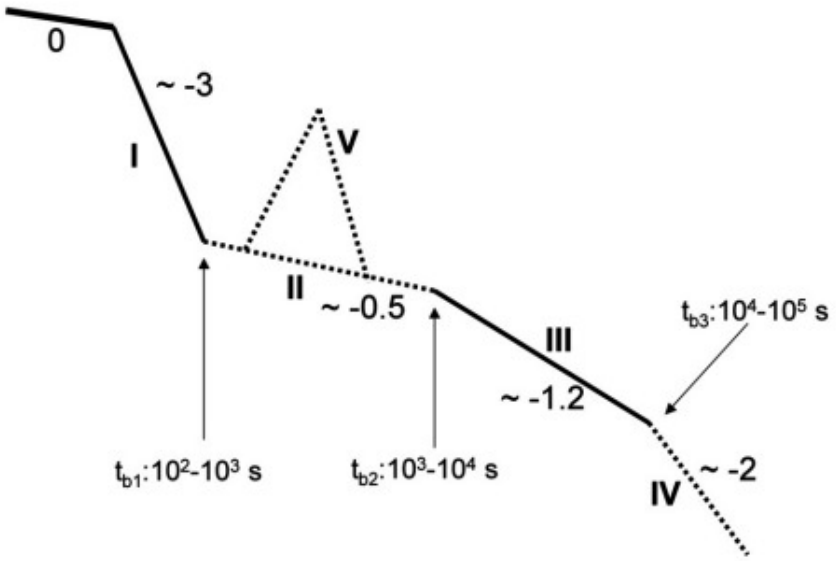

Figure 1.9: Modelization of an afterglow showing all the features presented in the text.

1.4 Short and Long GRB

GRBs are divided in two categories: short and long. This division is determined by the duration of the prompt phase of the GRB, more precisely of the T_{90} (the time in which 90% of the total fluence emitted from the GRB is detected): collecting the T_{90} of an important number of GRBs, two peaks can be found at 0.3s and at 30s, with a through at 2s. By consequence, short GRBs last less than 2 seconds, while long ones live longer. However this method to classify GRBs is not universally correct, since the T_{90} can change depending on the energy range selected. Especially in the border zone, a GRB can be short for one instrument and long for another one working at different energies. To this categorization, researchers tried to associate different origin models or progenitors. In particular, short bursts are thought to be originated by the merging of compact objects (NS-NS or NS-BH) since their host galaxies are usually elliptical or early-type, which means they have little star formation, and even when they are found in star forming galaxies, they present a large offset from the host galaxy (about 5 times larger then for long ones [26]), so again they are in a region of the galaxy with low star formation rate. On the other side,the long GRBs are due to core collapse of massive stars, in particular those producing SNe Ic, since these GRBs are usually found in highly star-forming, irregular or spiral galaxies, and their spectra shows no sign of hydrogen or helium emission. The progenitors could very likely be Wolf-Rayet stars. Not all SNe Ic will give rise to a GRB, less than 3% actually do.

However this division is not as precise as it has been presented. While there are some long GRBs for which the SN has been clearly spectroscopically identified, like GRB 980425/SN 1998bw, the first time that this association was made, and many others with different degree of confidence, there are also examples of long GRBs (GRB 060614 and 060505) that can not be associated to any massive star collapse. The majority of cases for which the SN-GRB correlation has been made concerns nearby events (low redshift), which are fainter in general. This is important since it allows to see the signal of a SN. This association has been seen also for a few brighter GRBs (GRBs 030329 and 130427A), always at low redshifts, allowing the hypothesis that even high redshift GRBs, usually very bright and for which it is impossible to observe a SN, are related so SNe Ic. Regarding GRB060614, as it has been said before, this GRB shows that there are exceptions in the model just defined. This GRB lasted approximatively 100s, putting it with enough confidence in the long GRBs category, and is one of the closer GRBs found (z=0.125). Despite that, follow up observations for the next tens of days did not show any SN emission, going against the predicted model. Moreover, it is similar to short bursts under many observational properties [27].

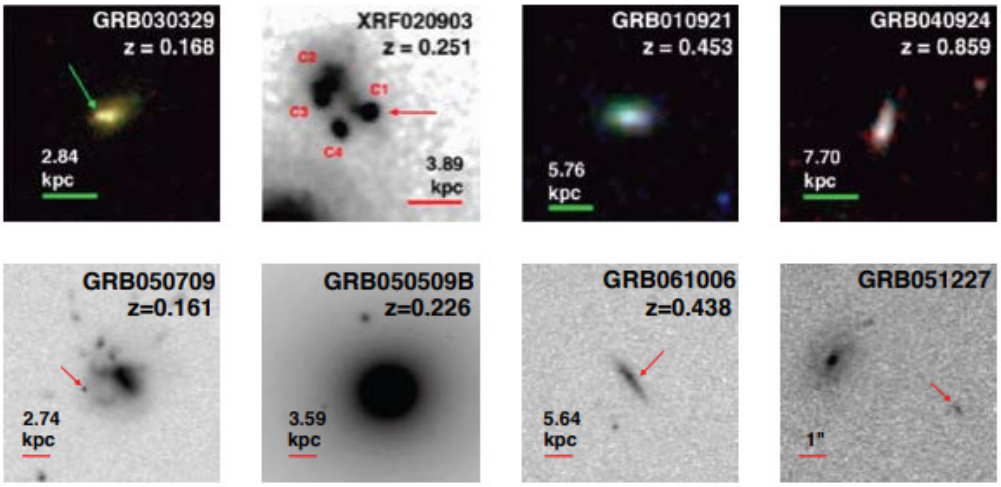

Figure 1.10: Host galaxies for both long GRBs (top row) and short GRBs (bottom row), imaged from the Hubble Space Telescope.

An interesting discussion about the difficulties in classifying the GRBs can be found in [28], related to GRB 200826A. Classified as short, since its T_{90} is of about 1 second, it presents several characteristics of long GRBs: first of all the progenitor seems to be a collapsing SN, since a SN bump was detected observing the afterglow; secondly, exploiting the Amati relation, it is clear that this GRB behaves like a long one. This paper presents alsoa different classification for GRBs (Type I and Type II) based on new criteria.

Why those two models ? It has been said that their host galaxy is favourable to these models. Another reason is the huge quantity of energy released during the explosion that requires very particular situations, in particular an enourmous amount of mass supply to activate the central engine since the efficiency of conversion of mass into energy is very low (up to ten percent at best). Both in the collapse of a massive star and in a binary merger system of compact objects this request is satisfied. These are not the only models that have been proposed, but they are the ones which have received more success and attention. Another important model for long GRBs is the magnetar model. Although it has some limits on the released energy, it also has some good points in explaining other features of the GRBs.

A more recent discovery, is the relation of short Gamma-Ray Bursts with Gravitational Waves (GWs, GW170817/GRB170817A) [29]. More precisely it seems that the short GRBs are the electromagnetic counterparts of GWs. This started the

era of multimessenger astrophysics and the collaboration of the GRB instruments with Virgo/LIGO, the GW instruments. (Figure 1.3)

In conclusion, there are many aspects of GRBs that still need to be explored and understood. Some examples already emerged from this short description of the gamma-ray bursts (but there are also many others aspects that still need to be explored):

- the mechanism responsible for the prompt emission spectrum of GRBs;
- the progenitor model;
- the correlation between GWs and short GRBs;
- and many more ...

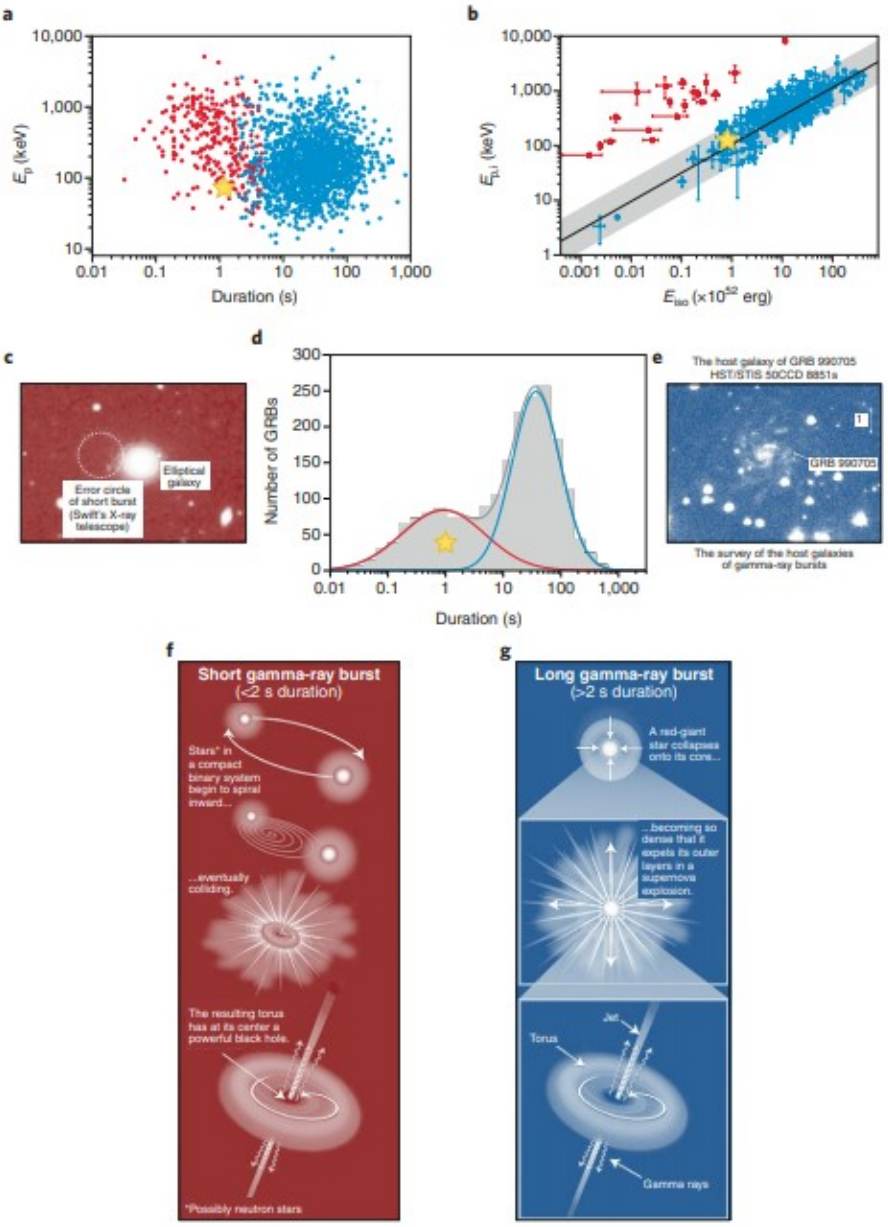

Figure 1.11: Main observational differences between short/type I and long/type II GRBs and standard scenarios for their origin. The spectral hardness–duration (a, obtained from GRBs in Fermi-GBM catalogue) and $E_{p,i}$˘E_{iso} (b, from GRBs of BeppoSAX, HETE-2, Swift/BAT, Konus-WIND and Fermi/GBM) planes used as criteria for the new classification in type I (f) and type II (g). Another criteria to be used is the location of the GRB in the host galaxy (c, e) and the properties of the host galaxy itself. Figure d (from CGRO/BATSE 4B catalogue) shows instead the bimodal distribution of the duration of GRBs. The yellow star is GRB200826A [28].

Chapter 2

The HERMES Pathfinder project

2.1 HERMES Pathfinder mission

HERMES (High Energy Rapid Modular Ensemble of Satellites) Pathfinder is a space-borne mission based on a constellation of nano-satellites, hosted on a low Earth orbit (LEO). These nano-satellites exploit a simple but innovative technique, described in the next section, to detect X and γ-ray emission coming from high-energy transient sources. These novel detectors will allow HERMES Pathfinder to reach its three main scientific goals:

- the accurate and fast localization of GRBs and other bright transients in the hard X-ray/soft γ-ray energy band, which is crucial, as it has been reported before, to study the electromagnetic counterpart of gravitational waves;
- exploring the temporal structure of the GRB lightcurve down to microseconds at X-ray energies for the first time thanks to its technology, in order to put better constraints on models of the GRB central engine;
- find evidences of quantum space-time scenarios, through measures of the time delay between GRB photons at different energies.

One of the key words in the HERMES acronym is Modular, that indicates the multiplicity of nanosatellites developed for the project. This is one of the main advantages since it avoids single points of failure: if one nanosatellites stops working, the others will not be affected; also it is easier to replace a malfunctioning nanosatellite, and with lower costs, compared to a regular satellite. The modular nature of the project brings also another advantage: since the nanosatellites are produced in sequence, the techniques used in their assembly can be improved after each nanosatellites, in order to improve the manufacturing process.

The strategy adopted by the HERMES Pathfinder collaboration is to initially produce a small fleet of nanosatellites to verify not only the hardware aspects but also the capacity of the instrument to observe GRBs and reach the planned goals, and then to expand the production of nano-satellites to reach a full constellation. HERMES TP-SP (Technological Pathfinder, HTP/Scientific Pathfinder, HSP) represents the project to produce the initial small fleet. They are funded by ASI (Agenzia Spaziale Italiana, Accordo Attuativo HERMES Technologic Pathfinder n. 2018-10-H.1-2020) the former, and by H2020 (European Union's Horizon 2020 Research and Innovation Programme, grant agreement HERMES-Scientific Pathfinder n. 821896) the latter. This first constellation is composed by six 3U CubeSat, that will work on an equatorial orbit. To these is added another nanosatellite, SpIRIT (Space Industry Responsive Intelligent Thermal), developed by the Australian Space Agency in collaboration with the University of Melbourne. It is a 6U CubeSat that will host one HERMES Pathfinder detector and will operate on a Polar Sun-synchronous orbit [30]. This will provide important information on how the detector behaves going over the South Atlantic Anomaly (SAA), whose impact is less relevant on an equatorial orbit. While the launch of SpIRIT is already fixed for november 2023 with Falcon 9, for the HERMES Pathfinder units the situation is less defined. Originally planned with Virgin Orbit, after its declaration of bankruptcy a new launcher must be found. The main objective of the HERMES Pathfinder mission is to prove that even using small detectors, to fit inside the nanosatellites, i.e. having reduced effective areas for the collection of photons, with reduced power supply possibilities, with costs at least one order of magnitude smaller compared to usual expenses for mission with similar scientific goals, and with only a few years for the development of the mission, it is perfectly possible to achieve the prefixed scientific goals. In particular, these first units will have to prove that they are able to:

- Detect GRBs even with their reduced surface detectors;
- Compute the cross correlation function between the arrival time of the GRB signal on different detectors to study all relevant statistical and systematic errors;
- localize, in a large Field of View, bright long GRBs and the majority of short GRBs with a precision going from a few degrees to fraction of degree for the GRBs offering the best conditions of observation.

Once these preliminary goals are satisfied, the HERMES Pathfinder constellation of nanosatellites can be expanded to reach the HERMES Full Constellation stage. It consists in tens or even more than a hundred nanosatellites that will guarantee continuous full-sky coverage in the search of transients. After the transient has been precisely localized, with all the necessary time-delay corrections,

the combined data of several nanosatellites will be equivalent to the data obtained from a satellite with a very large effective area, allowing for a better sensitivity. As it has been pointed out, one of the strenghts of HERMES Pathfinder is the fast and precise localization that it will provide thank to the multiple detectors deployed. The technique is the same that was used by the Vela satellites first and then by the IPN up to today. It consists in measuring the delay between the observation times of the different satellites that detected the same signal.

2.2 HERMES Pathfinder Payload description

The HERMES Pathfinder detector payload is represented by one CubeSat standard unit in a 3U nanosatellite ($30\times10\times10\,cm^3$). The payload must fulfill ambitious requirements in order to achieve the objectives of the HERMES Pathfinder project. These are to obtain the position information with a precision of 1 arcmin or less for bright long GRBs, and at least of 1° in the other cases, a broad energy band of observation, good efficiency and energy resolution. The details can be found in Figure 2.1.

Requirement	Condition	Value
Sensitivity	3–20 keV (GRB short/long)	≤ 1–2 ph/s/cm^2
	50–300 keV (GRB short/long)	≤ 0.4–1 ph/s/cm^2
Peak effective area	X-mode	≥ 50 cm^2
	S-mode	≥ 50 cm^2
Lower energy threshold		≤ 5 keV
Energy resolution EOL	between 5.0 and 6.0 keV	≤ 1 keV FWHM
	between 50.0 and 60.0 keV	≤ 5 keV FWHM
Time resolution (1σ)	X-mode	≤ 400 ns
	S-mode	≤ 250 ns
Time accuracy (1σ)	GPS locked	≤ 100 ns
	GPS unlocked (up to 1500 s)	≤ 200 ns
Field of view		≥ 3 sr FWHM
Background rate 50–300 keV		≤ 1.5 counts/s/cm^2
Background rate 20–300 keV		≤ 12 counts/s/cm^2
Background knowledge		≤ 5%
Maximum sustainable GRB flux		40000 counts/s
On-board memory		≥ 16 Gbit
Mass allocation		< 1.8 kg
Volume allocation		≤ 1.25 U
Power allocation		≤ 5W
Detector operative temperature range		−30° C — +10° C
P/L non operative temperature range		−40° C — +80° C

Figure 2.1: Requirements of the HERMES Pathfinder Payload . The X-mode refers to the technique for the direct observation of X-rays with the SDDs, while the S-mode refers to the observation of γ rays through the GAGG:Ce scintillation light.

All these characteristics of the HERMES Pathfinder nanosatellites must be obtained in a limited volume and mass, that is using different techniques and design than those normally adopted by larger satellites, that can also rely on more important power resources. For example, there is not enough space for an active control system of the temperature. The range of operative temperatures reported in Figure 2.1 is the balance between the space temperature and the heat generated by the on board systems. There are a few expedients that are used to lower the temperature as much as possible, e.g. low thermal resistance spacers between the PCB stack and the payload shear panels (see Figure 2.2) to dissipate the heat.

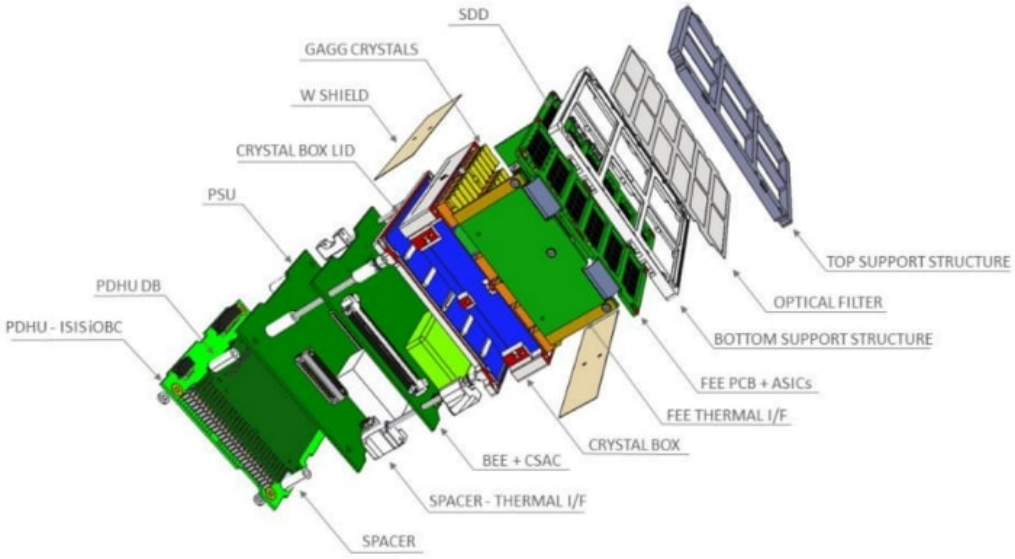

Figure 2.2: Exploded representation of the HERMES Pathfinder P/L.

The HERMES Pathfinder payload structure can be seen in Figure 2.2. It is composed by:

- Detector Assembly
- Back End Electronics (BEE) board
- Power Supply Unit (PSU) board
- Payload Data Handling Unit (PDHU) board
- Other components

The next paragraphs will describe all those major blocks, with particular focus on the Detector Assembly [31].

2.2.1 Detector Assembly

The detector assembly, as the name suggests, contains the detectors used to collect the photons in the hard x-ray/soft γ-ray band, i.e. the GAGG:Ce crystals and the Silicon Drift Detectors (SDDs), but also a support structure (including an optical filter to protect from direct visible, UV and IR light the SDD) and the Front End Electronics (FEE) board. From Figure 2.3 it is possible to see how the detector box is assembled.

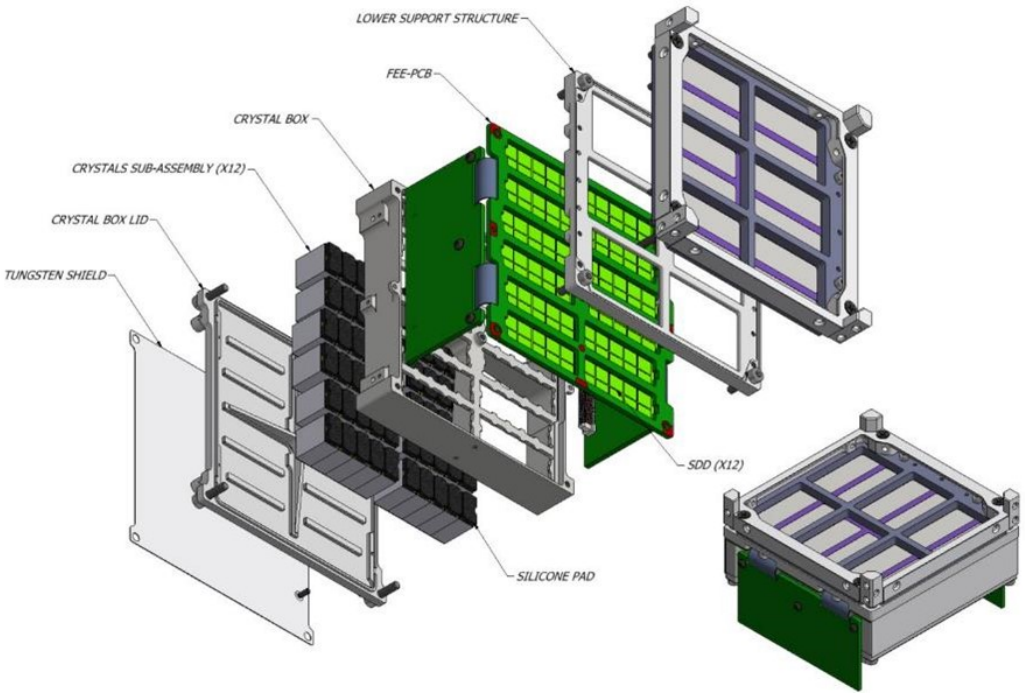

Figure 2.3: Exploded representation of the HERMES Pathfinder detector box

Before going through these structures in details, it is important to understand the detector working principle. The coupling of the SDD with an inorganic scintillator, based on the "siswich" concept [32][33], is crucial to study such a wide energetic band within a limited volume. Thanks to the geometry specifically designed for this project, where every single GAGG crystal is coupled with two cells of the SDD matrix, the SDD is able to play a double role: on one side it is used to directly detect the incoming lower energy photons (x-rays from a few keVs to ~50 keVs) incoming (X-mode observation), on the other side it will absorb

the light produced by the higher energy radiation (from 50 keV to a few MeVs) interacting with the scintillator (S-mode observation). Each GAGG:Ce crystal is coupled with two SDD cells, in order to distinguish the two cases: if the interaction takes place inside the scintillator (higher energy, γ-ray) both the SDD cells coupled with it will be equally irradiated, while in the other case, i.e. when the photon is directly detected by the SDD, the two channels will show different read out (since only one cell will interact with the x-ray).

2.2.1.1 Support structure

As it can be seen from Figure 2.3, the support structure is mounted on top of the detector, to allow its mechanical connection with the rest of the payload. It is composed of an upper and a lower support structure, both made of stainless steel, and an optical filter in the middle (see Figure 2.4).

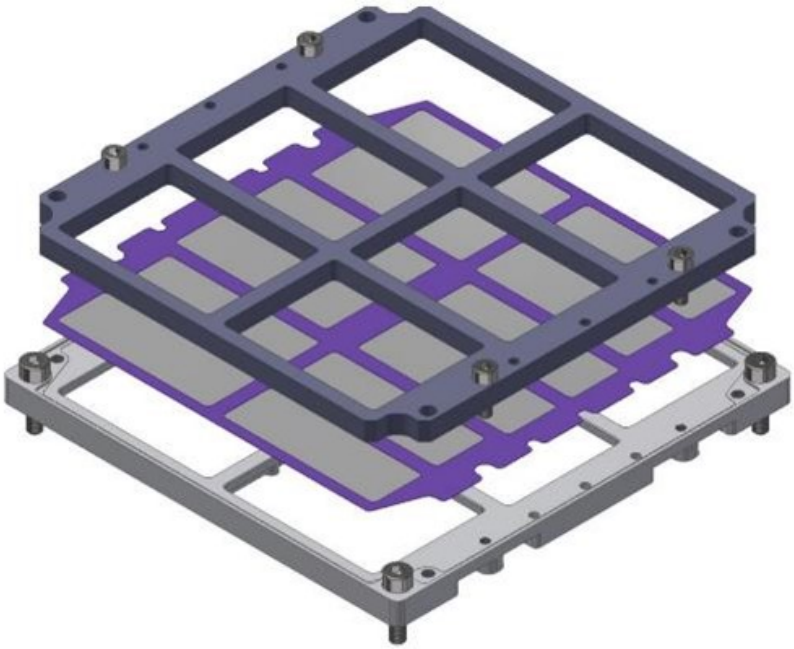

Figure 2.4: Exploded representation of the HERMES Pathfinder support structure

The optical filter plays an important role in preventing the optical and UV light from reaching the SDD, in order to reduce the induced dark current noise. This filtering is obtained by applying an aluminum deposition on a thin layer of Polymide. The thickness of both materials depends on the transparency required. After several tests, in which different possible configurations (in dimension and shape) have been used, a prototype made of a 300 nm thick aluminum layer and a

1 μm thick Polymide layer, has been chosen for the performance and qualification tests. The filter is mounted on a 100 μm thick nickel structure to obtain the required mechanical resistance.
The optical filter plays also a role in the thermal design of the payload, which is based on passive cooling (low or no energy consumption cooling system). It is important to maintain the SDD at a certain temperature for its correct functioning. For this scope, on top of the support structure there will also be a multilayer insulation (MLI) layer.

2.2.1.2 Silicon Drift Detector

Silicon Drift Detectors are the current state-of-the-art for high resolution, high count rate X-ray spectroscopy. First developed by Emilio Gatti in 1984 [34], the SDD is a peculiar silicon detector in which the surface electrodes, formed by p-n junctions, shape the electric field, within the fully depleted bulk of the detector, so to collect and drive the electrons, generated by the interacting radiation, towards small capacitance collecting anodes. In this way it allows the best possible match to the read-out electronics and optimal signal to noise ratio for low enery X-rays.

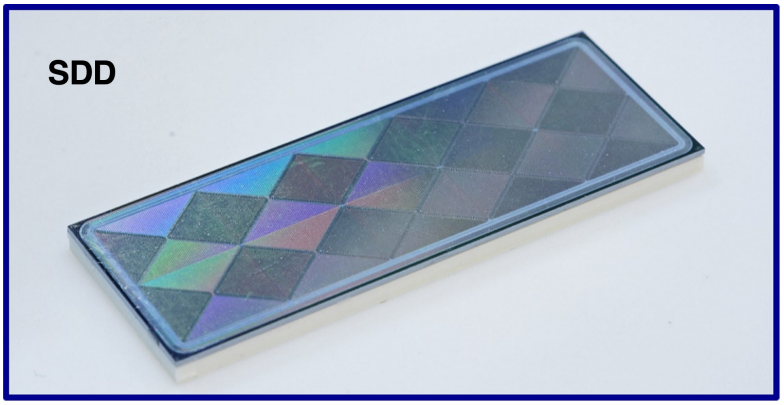

Figure 2.5: SDD array.

The SDDs used in HERMES Pathfinder nano-satellites are the results of the Italian ReDSoX collaboration. The use of the SDD, instead of other instruments, can be justified as follow. Compared to the photomultiplier tube (PMT), the efficiency of the former is significantly better (90% against 20%). Moreover, the volume of a PMT would be complicate to fit inside the 3U CubeSat and the power consumption is higher. Finally, the PMT is not able to observe in the X range, consequently the energy band observed would be significantly lower. Another comparison can be made with Silicon photomultipliers (SiPM): even if these de-

tectors have a faster response, they are very small, so it would be necessary to assemble a bigger number of units to obtain the requested area. By making small SDD cells, the difference in time response is kept low. Also, SDDs showed a better resistance to radiation compared to SiPM and are able to directly detect low energy X-rays, fundamental to guarantee the broadband required for this project.

The current state of the consolidated design/process concerns, for example, pitch and distance of the drift cathodes, low power consumption of sensors, extremely low dark current, high detection efficiency (both for ionizing radiation and optical photons), enhanced efficiency on the sensor edges, optimized charge collection efficiency. Because of its very low dark current and intrinsic low noise, that allow the SDD to detect low energy X-rays, the detector must be protected as much as from all possible sources of noise, both external and internal to the nanosatellite. Consequently, this affects the choices made for all the other components around the detectors.

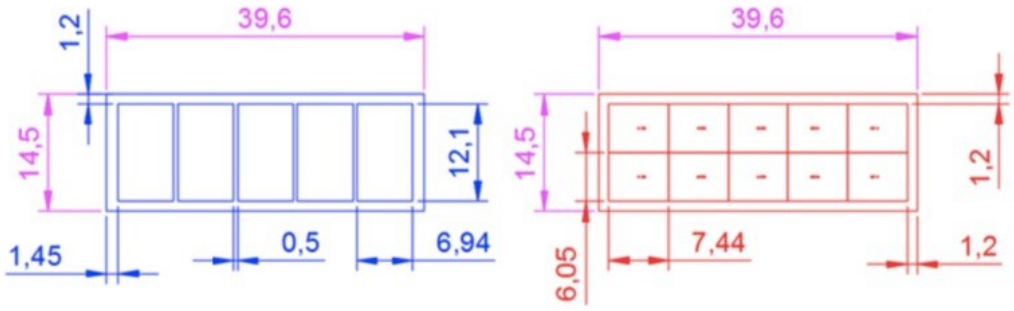

Figure 2.6: SDD design. Left: p-side showing the crystals arranged on the SDD array. Right: n-side showing the surface of the two collection zone of the SDD.

The SDD is the core element of the HERMES Pathfinder payload. The full detector on board of the CubeSat is composed of 120 SDD, grouped on 12 detectors, each one made of a 2×5 cells array. The cell size is 6.05×7.44 mm^2, with a thickness of 450 μm (see Figure 2.6). The area of a single cell is about 0.45 cm^2 in order to reach the low noise level required for the detection of X-ray up to 20-30 keV with a good efficiency. The n-side, which is the one exposed to the radiation, present the bonding pads, some of them in common to all cells, like the ground (GND), U-bias and Control Ring in the guard ring area surrounding the detector, others are unique for every cell, like the first cathode pad and the anode pad, in the middle of the cell. Instead, on the p-side, devoted to collect the light produced by higher energy radiation crossing the SDD interacting with GAGG:Ce crystal, the SDDs are optically coupled through thin siliconic mats with the scintillators, 2 cells for each crystal.

Finally, a frame made of Kovar (an iron, nickel and cobalt alloy), is glued on the p-side using an epoxy resin (Epo-Tek 301-2). This frame provides an optical separation between adjacent crystals and mechanical strength.

2.2.1.3 Front-End Electronics (FEE)

The front-end electronics board is a PCB specially realized using the Rigid-Flex technology, consisting of a central board and two lateral wing boards that can bend up to 90°. This design has been chosen in order to satisfy the constraints imposed by the small space available and the new read-out electronics.

The 12 SDD matrices are mounted on one side (bottom) of the central board of the PCB, while on the opposite side (top) there are 120 LYRA-FE chips, one for each SDD cell. This PCB carries several apertures, one for each array of SDDs, for a double reason: to improve the detection of soft X-rays (<30 keV) by reducing the materials that they have to pass through and to allow the electrical bonding between the SDDs and the LYRA-FE chips [35]. As for the wings, they house the 4 LYRA-BE chips, two for each wing, dividing the detector plane in 4 quadrants, named A and B on the left wing and C and D on the right one. In order to connect the wings, once they are folded at 90°, to the rest of the detector payload unit, a Samtec ERM8-06-02 connector is mounted on each wing. (Figure 2.7)

The reason why there are 32 input adresses is that the design of the analog ASICs FEE used in HERMES Pathfinder comes from the VEGA ASIC project [36], developed within the ReDSoX collaboration during the LOFT Phase-A study. The HERMES Pathfinder LYRA ASIC is made of 32+1 Integrated Chips (ICs). The first 32 (although only 30 are used in a HERMES Pathfinder quadrant) are Front-End ICs, they include a preamplifier, a first shaping stage and a signal line-transmitter. Every LYRA-FE chip is made of two indipendent circuits, but only one will be actually used. The second one is spare. Those small ICs (0.9×0.6 mm^2) are placed as close as possible to the SDD anodes, to reduce the system noise due to the stray capacitances of the detector-preamplifier connection and maximize the effective-to-geometric area ratio for the detector plane. The last IC, instead, is a LYRA-BE, a 32-input mixed signal ASIC with all the remaining circuits required to complete the signal processing chain: second stage of the shaping amplifier, threshold discriminator, peak and hold circuit, analog output multiplexer.

The LYRA-BE has two working modes: configuration and operation. The first mode allows to set all the parameters, like the threshold of the trigger, or the switched-on channels. When the second mode is active, the ASIC will send out an

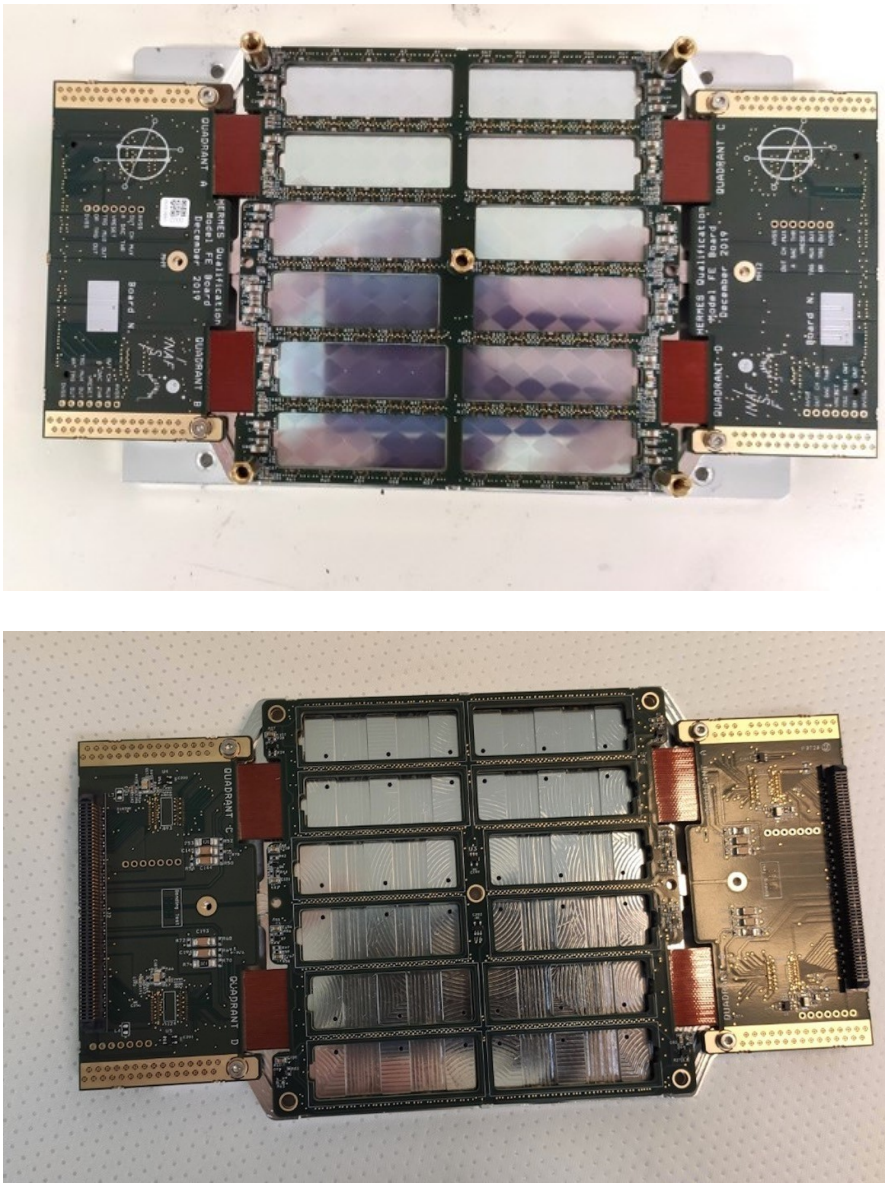

Figure 2.7: Front End Electronic board, top side on the upper image, with all the electronics (LYRA FE), which adjoins the support structure, bottom side on the lower image, where the SDDs are glued. Notice also the two wings, here deployed, but bend at 90° in the final configuration.

OR-trigger signal if a channel reports a signal above the threshold and the analog signal of the Peak-Stretcher will go through the output via the multiplexer.

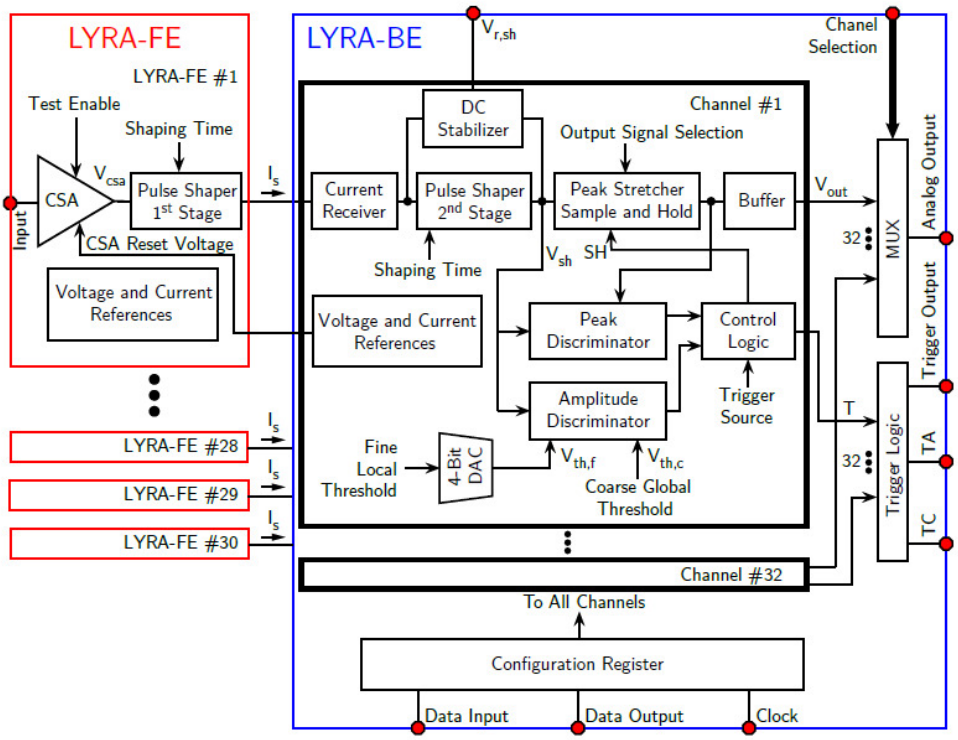

Figure 2.8: Block diagram of the LYRA ASIC chipset.

2.2.1.4 GAGG:Ce scintillator crystal

The choice of the GAGG:Ce (cerium-doped gadolinium-aluminum-gallium garnet, $Gd_3Al_2GA_3O_{12}$) as the crystal scintillator to be coupled with the SDDs, is due to several characteristics of this crystal that respond to the requests of the mission. More in details, it has an high intrinsic light output ($\sim$ 57 ph/keV), with an emission peak at 520 nm, no intrinsic background, no hygroscopicity (no water absorption), a fast radiation decay time ($\sim$ 90 ns), a high density and a mean atomic number of 54.4. These features make the GAGG:Ce the best choice among the commonly used scintillators for the HERMES Pathfinder detector. Each crystal has a 6.94×12.1 mm^2 cross-section and is 15 mm thick. In order to optimize the scintillation light collection to the SDD cells, the scintillators are wrapped in a reflective material (thickness $\sim$ 105 μm), leaving uncovered only the face that will be optically coupled with p-side of the SDD detector. The outline of the wrapping can be seen in Figure 2.10. The coupling is done inserting a silicone pad (Dow Corning 93-500) about 3.32 mm thick, that can be pressed to guarantee an optimal optical and mechanical coupling between GAGG:Ce and SDD.

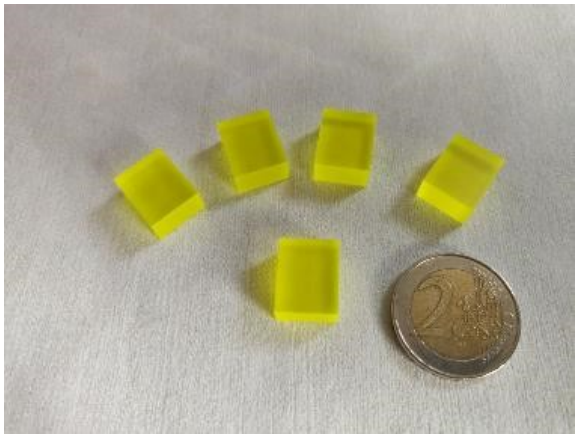

Figure 2.9: GAGG:Ce crystals

However, once the crystals will be sent in a low-Earth orbit, the amount of high-energy radiation present there could lead to a degradation of the performances of the crystals. In particular, a residual luminescence (afterglow, that will be better described in chapter 3.1) has been noticed and studied as one of the main topic of this thesis.

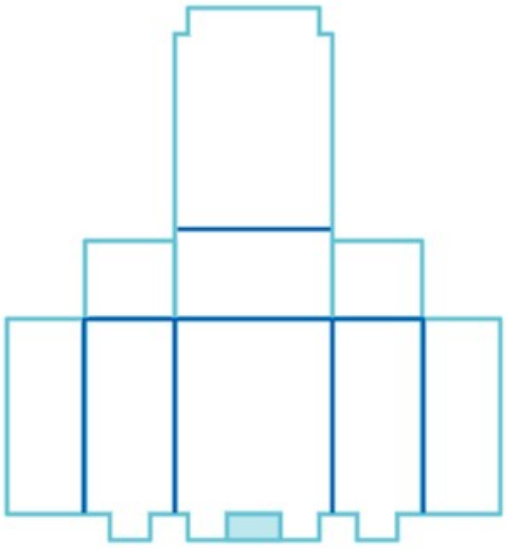

Figure 2.10: Model of the wrapping used for the GAGG crystals.

The full package of 60 crystals, grouped 5 by 5, is contained inside the Crystal box in order to obtain the required darkness for the scintillator. This box is made in AISI 316 stainless steel. On the top of the box, between the GAGG:Ce and the

SDDs, there is a thin layer with holes in correspondence to the GAGG crystals positions. Inside these holes protrude 10 tips, to prevent the crystals from weighing directly on the SDDs. On the bottom and, partially, on the sides (2 out of 4) of the box there is also a layer of tungsten ($\sim$ 200 μm) to minimize the particle induced background (see Figure 2.2).

2.2.2 Back-End Electronics (BEE)

For this section and the following ones, the description is less detailed, since those are not components of the nanosatellites directly studied by the author. However, some of the tests done on the nanosatellites, for this doctoral work, were carried out after these components have been integrated to the detector assembly so it is useful to illustrate them.

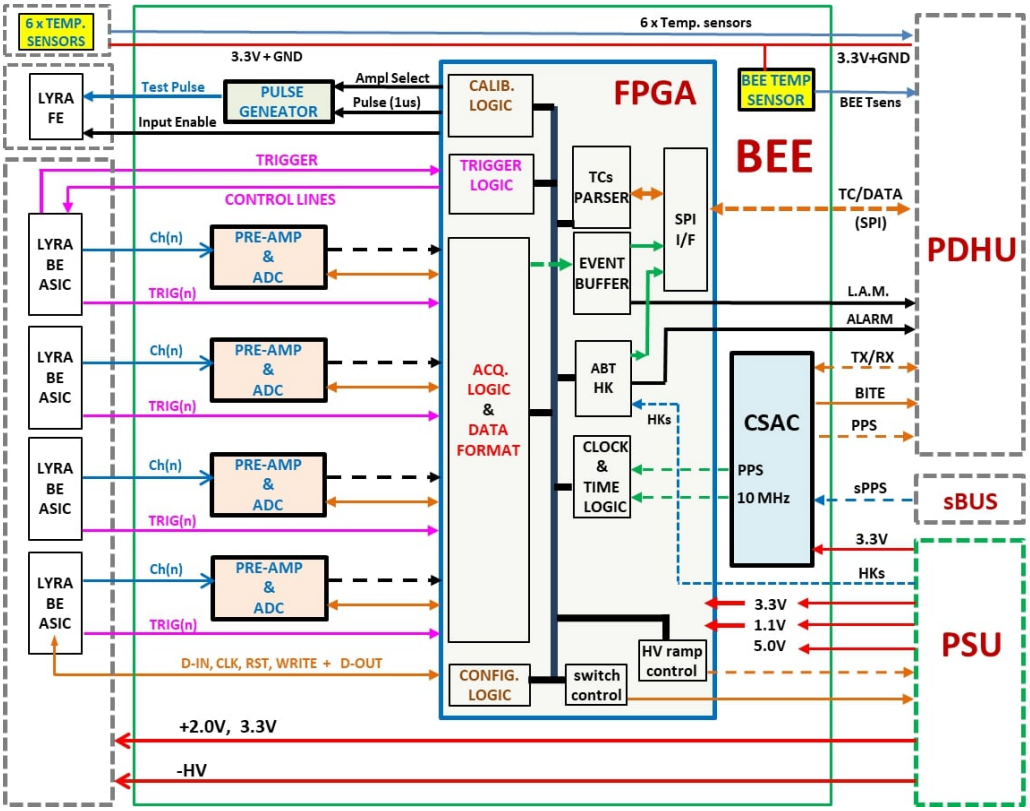

Figure 2.11: Block diagram of the BEE.

The Back-End Electronic (BEE) is the "brain" of the payload. It is the logic block placed between the FEE and the Payload Data Handling Unit and it is from here that the majority of the comands are given. The BEE take care of configuring

the ASICs, HKs (House Keepings) collection (status of the payload, voltages, temperatures, ...), switching ON/OFF of the power lines required by the FEE, logic for event trigger detection and acquisition, generation of a test pulse for calibration, transmit science data and HKs to the PDHU as well as to receive and decode telecommands sent by the PDHU. The BEE board also hosts the Chip Scale Atomic Clock (CSAC) that, together with the GPS/PPS signal, will provide the on-board timing reference. About the CSAC, it has to satisfy the general requisite to fit in a nanosatellite: low power consumption, small volume and light weight. The onboard clock must also guarantee an extreme accuracy on the observation time of the photons in order to obtain the required precision in tracking the position of an event by combining the data from different nanosatellites.

For each of the four quadrants, the BEE board has an ADC in order to be able to study multiple events. The configuration of the LYRA-BE ASICs, as well as all the comunications about data exchanges (both events and HKs) and changes in the operational mode, are made from the PDHU through a serial line (SPI). In particular, regarding the data acquired by the BEE, they are intially collected in a buffer, and then transfered every second to the PDHU, unless the buffer saturate before. In this case a signal is generated in the BEE to make the PDHU read the event buffer before the end of the second.

2.2.3 Power Supply Unit (PSU)

The PSU board contains all the voltage generators utilized by the payload. In particular there are 3 lines of power supply:

- +12 V line, to power the high voltage (HV) DC/DC converter, which is necessary to provide the SDDs of the negative bias voltage (~ -120 V) to work properly;
- +5 V line, which provides 3 different voltages (2.0 V, 3.3 V-A and 3.3 V-D) to power all 120 LYRA-FE and the 4 LYRA-BE.
- +3.3 V line, connected to BEE, PDHU and the Chip Scale Atomic Clock.

All three lines are controlled through electronic switches placed on the PSU. These in turn are controlled by the PDHU. The only open line is the one between the PSU and the PDHU. There is also a second set of switches placed in series with the first ones, that are comanded by the BEE FPGA, once it is turned on.

2.2.4 Payload Data Handler Unit (PDHU)

The crucial role of the Payload Data Handler Unit has been already pointed out in the previous sections. It interfaces with both BEE and PSU, but also with the CSAC, to which it provides the mission start date, and with the rest of the nanosatellite. It establishes the operational mode, it transforms the raw data collected by the BEE in a predefined format and controls the burst trigger logic.

The operational modes that have been established for the HERMES Pathfinder nanosatellites are the following:

- BOOT, this is the first mode after switching on the system;
- STANDBY, the PDHU move immediately to this mode after being powered, while the detector is still off. This mode is very useful to check up the status of the system;
- READY, the switches are turned on by the PDHU but the detector is still not operating. HKs and all interfaces are available;
- IDLE, the detector is finally powered on and from here it is possible to go in observation mode, and then return to this operational mode. Also it is possible to change the configuration of the BEE FPGA;
- OBSERVATION (and CALIBRATION), as the name suggest it is the mode in which the datas are collected by the detectors.

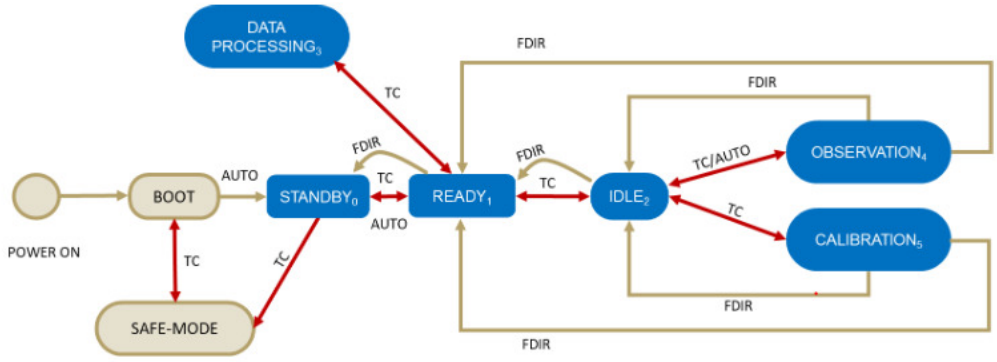

Figure 2.12: Schematic representation of the operational modes of the HERMES Pathfinder Payload.

There are also other possible modes to which the system can access in particular situations like a period of low power availability (POWER SAVE) or in cases

of major errors or malfunctions (SAFE-MODE). During the operational modes described above there is also an other pseudo-mode in act, the Fault Detection Isolation and Recovery (FDIR), ready to intervene in case of anomalies.

It is important to point out that it is not possible to jump from one mode to another randomly, but there is instead a well defined path to follow, which is given by the order of the operational mode in the list. All these transition are made through a telecommand.

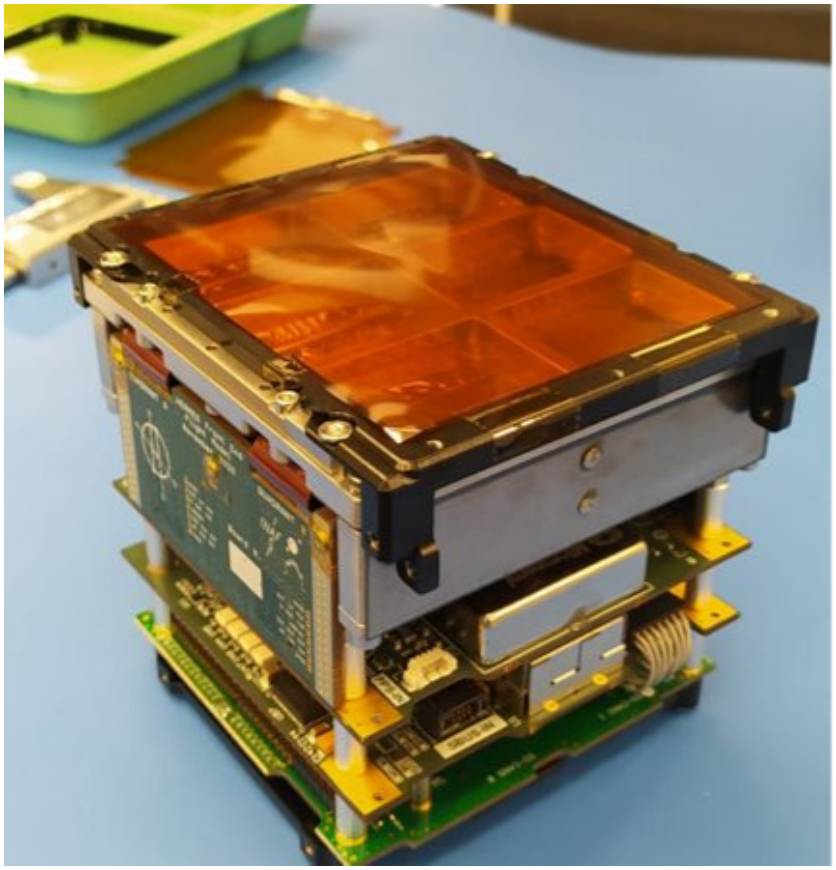

Figure 2.13: Detector Unit of the HERMES Pathfinder FM1/SpIRIT nanosatellite.

Chapter 3

Thesis works

3.1 Characterization of the GAGG-SDD detector

As explained in the previous chapter, the HERMES Pathfinder detector will exploit a new coupling of crystal scintillator (GAGG:Ce) and silicon detector (SDD), specifically thought and designed for the reduced dimensions of the nanosatellites and to study transient sources in the X and γ energy range. Since it is the first time that these two objects are combined together, it is necessary to deeply characterize them.
In particular, during the first tests with the GAGG:Ce crystal, it was noticed that, after being irradiated with photons or charged particles, the crystal shows a residual luminescence, or afterglow [37]. The luminescence is due to meta-stable states (or traps) that are generated inside the irradiated crystal and decay over time, as it will be explained better afterwards. This was studied for the first time in Dilillo et al., 2022 [38]. However, being the first study of its kind, many difficulties have arisen during its carrying out. The problems were of different kinds: there was no precise knowledge of the temperature and its variations during the measurements, the timing of the measurements with respect to the end of an irradiation step was not very accurate, the PMT bias voltage differed somewhat from a measurement set to the next, and the final results included the scintillation light due to nuclear decays in the crystal.

Thanks to the experience gained during the first GAGG:Ce irradiation campaign with protons, a second phase of tests was prepared. This time, the study is divided in two irradiation phases: a first set of irradiation steps using a LED light, then a second one using protons like in the first afterglow study. This is done in order to improve the current knowledge about the residual luminescence of the crystal, and its impact on the energy resolution of the detector, and eventually

discover radiation damage that could be caused by cosmic rays once in orbit.

3.1.1 Development of the experiment

A sophisticated apparatus was developed to fulfill the conditions necessary for the proper characterization of the HERMES Pathfinder detector.

The experiment consists in observing the light emitted by the crystal both while it is being excited and subsequently. Since the flux of photons it radiates changes dramatically, two different kinds of sensors are needed. The SDD cells designed for the HERMES Pathfinder detector are well suited to measure the scintillation light emitted by the crystal while it is irradiated, but become useless in studying the afterglow. Indeed, soon after the end of an irradiation the current induced by the residual luminescence on these sensors becomes smaller than their leakage current. For this reason a second sensor was coupled to the crystal face opposite to that optically coupled the SDD cells: the choice fell on a photomultiplier tube (PMT) that features a gain of 10^6. The drawback of this sensor is that it can be damaged by exposure to intense light, so it must be switched off during the irradiation steps. The continuous measurements of the crystal emission by the SDD cells address two important aspects of the experiment: they provide accurate timing (the anodic currents of the SDD cells and the PMT are sampled at the same times) for switching on the PMT, and allow to compare the LED measurements to the proton data by rescaling the former by the ratio of the currents induced on the SDD cells during the irradiation steps.
The GAGG:Ce crystal and the SDD used for this experiment correspond to those described in chapter 2. The only difference concerns the crystal wrapping, since there is a second detector, the PMT, optically coupled to the crystal. The same kind of silicon mat of 1 mm of thickness used between GAGG:Ce and SDD is also used to do the optical connection between the scintillator and the PMT. All the operations of optical coupling are done with extreme care in removing any kind of contamination that could alter the current measures. The silicon mat and the crystal are washed with alcol and compressed air. As for the PMT used in this experiment, it is a hamamatsu r4125 model with a base EMI C662-A, shielded using a magnetic shield, as shown in Figure 3.1.

The apparatus built around the detectors must fulfill two crucial conditions in order to improve the quality of the measurements. These conditions are darkness and and thermal insulation.

The first one is probably the more straightforward to understand: being the GAGG:Ce a scintillator, it would be impossible to characterize the afterglow

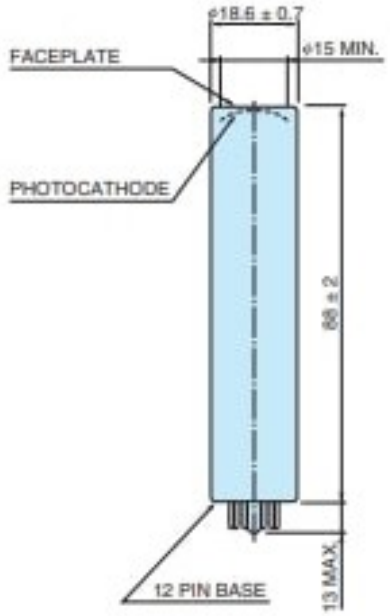

Figure 3.1: Photomultiplier tube, model r4125 Hamamatsu [39].

without obscuring ambient light since there would always be scintillation light; moreover, it would not be possible to characterize the afterglow without knowing precisely the amount of irradiation reaching the crystal, which can be done only isolating it from any uncontrolled source of light. There will always be cosmic rays arriving at the crystal, but their number is small and those events can be easily removed from the analysis.
The thermal insulation is required since both the dark current of the detectors and the afterglow current depend on the temperature. Going more into details, one of the main reasons of dark current in PMTs is the thermoionic emission of electrons, which happens also at room temperature. In order to avoid strong fluctuations in the measured afterglow currents, especially a long time after irradiating the crystal, it is important to control the temperature of the PMT. Regarding the GAGG:Ce crystal, during the analysis of the first irradiation campaign, it has been noticed that there might be a temperature dependence from the mean lifetime of the meta-stable states. In particular, the higher the temperature is, the faster the meta-stable state decays. With these two aspects in mind, it is clear that having the control over the temperature of the crystal and the PMT is extremely important.
In order to achieve these two conditions, a two nested boxes system was developed in the workshop of the physics department of Udine University. The inside box, made in aluminium, is large enough to contain all the detectors and the crystal, about 30x30x30 cm^3 internally, and guarantees the isolation from external sources.

The faces are made from 3 mm thick panels, making the system solid and avoiding any deformations, necessary to maintain all the detectors perfectly aligned. The faces are fixed to each other by means of alluminium angle profiles. At the same time, the choice of the material allows a control of the temperature using an external cooling system. Instead, the outer box is made of 5 mm thick polyvinyl chloride (PVC, one of the most common types of plastic) panels, to thermically insulate the apparatus from variations of the ambient temperature. The two boxes are kept separeted by means of 5 mm thick PVC pads. The gap between the boxes is small enough to further increase thermal isolation by suppressing convective air flows. The total dimension of the system is about 32.7x32.7x32.7 cm^3. The choices of the materials were done in order to minimize the formation of radioactive nuclei during the irradiation with protons. For this reason, the materials are all with a low atomic number.

The arrangement of the detectors inside the aluminium box had some aspects to be considered carefully. The base of the PMT has three cables that need to come out of the box. Only two of them are actually useful for this work, more specifically the cable to power the PMT and the one to bring out the anodic current. This is realized by creating a support fixed inside the box on one of the lateral faces. The PMT must fit perfectly inside this support in order to avoid any light entering, since at the other side of the support there is a hole to let the wires exit the box. The same hole is made on both boxes. Actually it is even larger on the outside box, since it is here that the cooling system is applied on the internal box. For this reason the support is made in aluminium. Finally, there is a small hole made perpendicular to the PMT base to fix it using a plastic screw. The details are shown in Figure 3.2.

The SDD is hosted on a printed circuit board (PCB), specifically designed by Nicola Zampa to perform tests on the GAGG:Ce-SDD detection system. Four SDD cells can be connected to dedicated electronics (integrated preamplifiers and discrete signal conditioning and trigger circuitry) for measurements with X and γ sources. These components are placed on the left half of the PCB as shown in the upper panel of Figure 3.3. The anodes of the remaining SDD cells can be wired either to the electric ground of the sensor or to a picoammeter through one of two SMA connectors on the right of the PCB. The SDD array is biased via a filtered resistive voltage divider receiving power from an additional connector placed next to the SMA connectors. The sensor array is fixed on the other side of the PCB by means of double sided adhesive tape with the anodes facing the PCB and centered on specific square holes. The board features 12 such holes, two more than the number of SDD cells, to provide additional degrees of freedom in selecting the sensor cells to use, since the available prototype devices feature large

anodic currents on some of the cells. The leftmost pair of holes can be used to connect two SDD cells to sensor ground when their current is too large making them unusable. The next two pair of holes provide the connection to the electronic channels, while the last three pairs provide access to the SMA connectors for the anodic current measurements. In this project a single GAGG:Ce crystal is analysed to characterise its afterglow induced by a proton beam. The experiment relies on the measurement of the anodic current of the two SDD cells coupled to the crystal, consequently the electronic circuitry is not needed and the other cells are connected to sensor ground. The two cells wired to the SMA connectors are those facing the third pair of holes from the right.

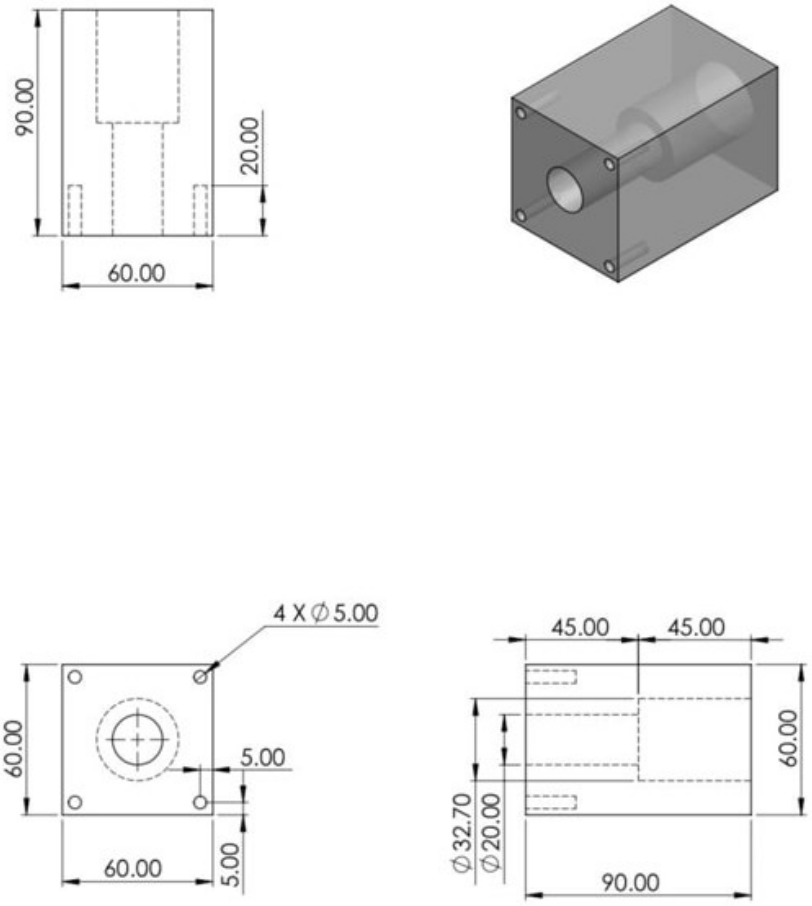

Figure 3.2: Schematics of the PMT support. The particular internal shape is realized from the PMT base, to avoid the detector decoupling from the crystal.

The PCB features also several circular mounting holes. The four at the angles of the PCB are used to fix it to the aluminium box, more precisely to the face

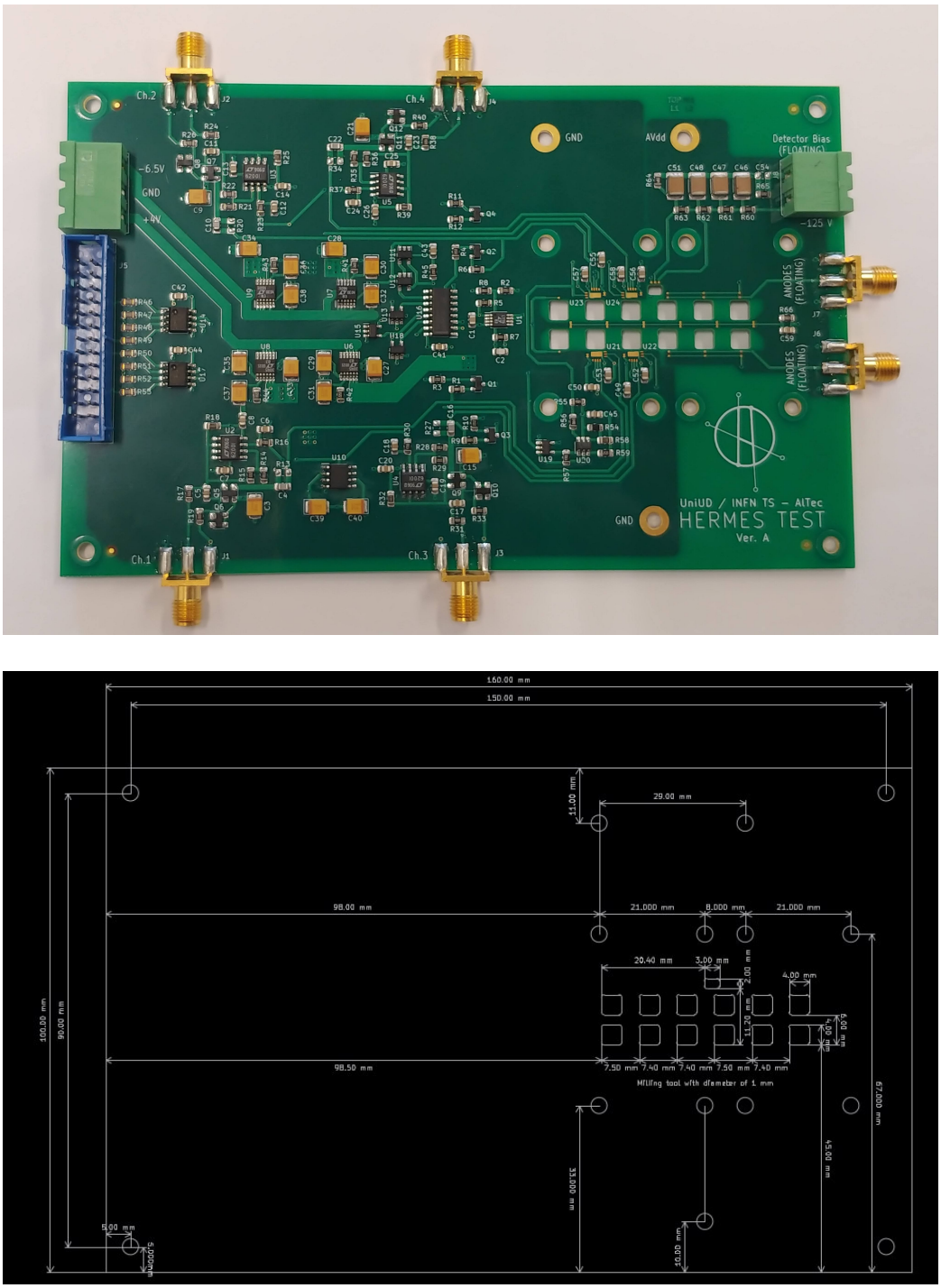

Figure 3.3: On the upper image the PCB used for this experiment, on the lower one the schematics of the same.

opposite to the one holding the PMT support. The PCB is fixed using plexiglass columns and polyethylene screws. In this way it is possible to adapt their length so that the SDD cells are perfectly resting on the silicon mat.
The holes placed around the region dedicated to the SDD array are used to fix the structure that will hold the crystal, since it is too dangerous and unstable to hold it in place only by compressing it between the SDD cells and the PMT. For this purpose, a support was specifically designed and realized using a 3D printer. It was built into three separate pieces to ease its assembly around the crystal. The schematics and the final result are reported in Figure 3.4. As it can be seen, there are several features of this structure that need to be explained.

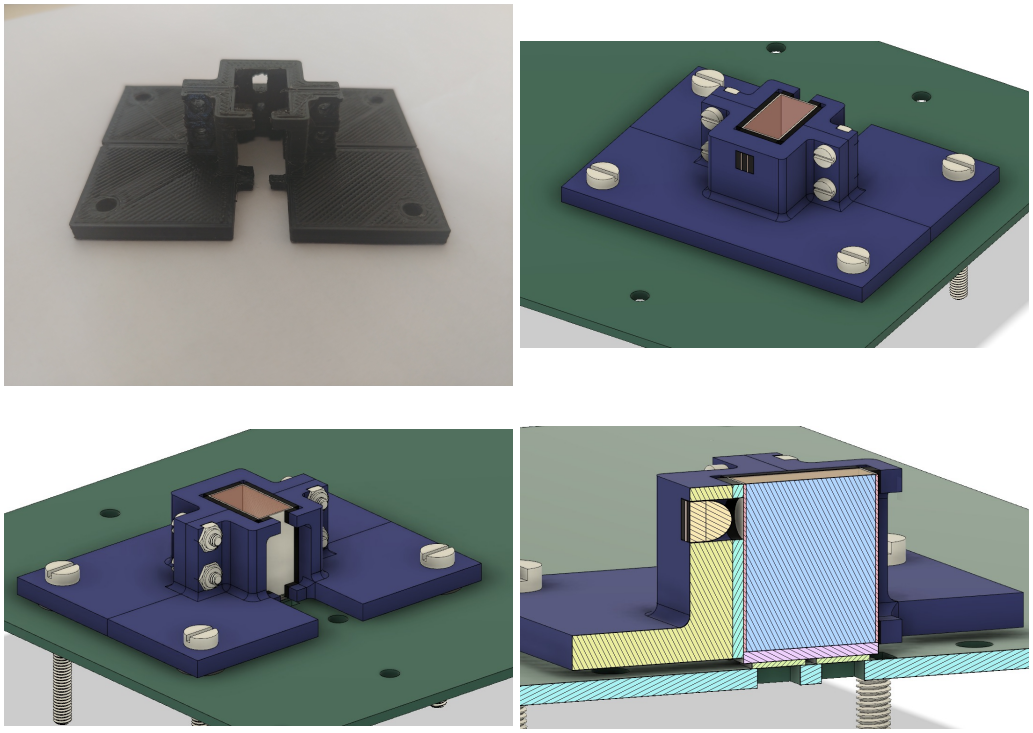

Figure 3.4: On the upper left image the final result for the GAGG support used for this experiment, on the upper right and lower left the computer modelling of the structure, on the lower right the cutaway drawing.

The support structure is going to be irradiated with protons, due to its proximity to the crystal. The same logic used for the boxes must be applied here in the choice of the material. It is necessary that the material of the support structure has a low atomic number to reduce the interactions with the protons and become radioactive. So the choice made is for PLA. To optimize the irradiation with protons, a hole is provided on the side facing the proton source so that the crystal is not covered by

the support structure. The GAGG:Ce is positioned with the longest dimension (15 mm) put between the two detectors and the middle dimension (12.1 mm) in the direction of the incoming beam of protons, which is more than the free mean path of the protons used during the tests (9 mm for the beam characteristics, described later). This is important to contain the protons inside the crystal and avoid that they exit behind the crystal. In correspondence with the hole on the support structure, there are two holes of 5 cm in diameter on the two boxes. Those two holes are then covered with four layers of solar filter produced by Baader each featuring a thickness of 12 µm and a photon stopping power of 99.999% in order to provide a barrier for ambient light while being trasparent for the protons. The multiple layer technique used is both to prevent any damage on one layer of the filter and to increase the stopping power against the photons.
Finally, the last aspect to be discussed is the two holes opposite to the one made for the protons (only one is shown in Figure 3.4 because the second one was added later). The first hole, which has a square shape, is used to fit the UV LED light, necessary for the first part of the tests, while the second, circular and smaller, is made for a thermocouple to measure directly the temperature of the crystal. The spectrum of the LED must be chosen in such a way that the photons it emits are completely absorbed within the crystal, in such a way that the SDD cells see only the secondary emission from the crystal (scintillation light and afterglow). Moreover, the photons should be able to penetrate few mm inside the crystal both to avoid edge effects and to emulate, at least approximately, the ionization pattern of the protons. By inspecting the absorption spectrum of GAGG:Ce plotted in Figure 4.5 one finds that the most appropriate region is around 300 nm. The chosen LED features a peak emission between 305 and 315 nm. The light is focused in an angle of 30° and it reaches the crystal through a small circular hole bored into the wrapping. Even if the hole in the support structure is made with the precise measures of the LED, it could still fall off the support structure because of the wiring to power it. As a precaution, some glue is applied on the border of the hole. Pieces of rubber are fixed internally of the crystal support structure to create more friction and to avoid any displacements of the crystal from its aligned position. Then, once the crystal is placed in position, all the structure is fixed to the PCB. The pressure applied on the silicon mat is such as to compress it by 5% (i.e. 50 µm), which is the nominal situation in the HERMES Pathfinder nanosatellites.

The apparatus exposed to the beam so far described needs additional equipment and proper connections to work adequately. The problem of connecting the PMT without breaking the darkness condition inside the boxes has been discussed already, similar issues arise for the connection of the SDD cells, the LED and the thermocouple. To bring the cables of the latter two devices outside of the boxes small holes (2-3 mm diameter) are bored into their walls, and subsequently

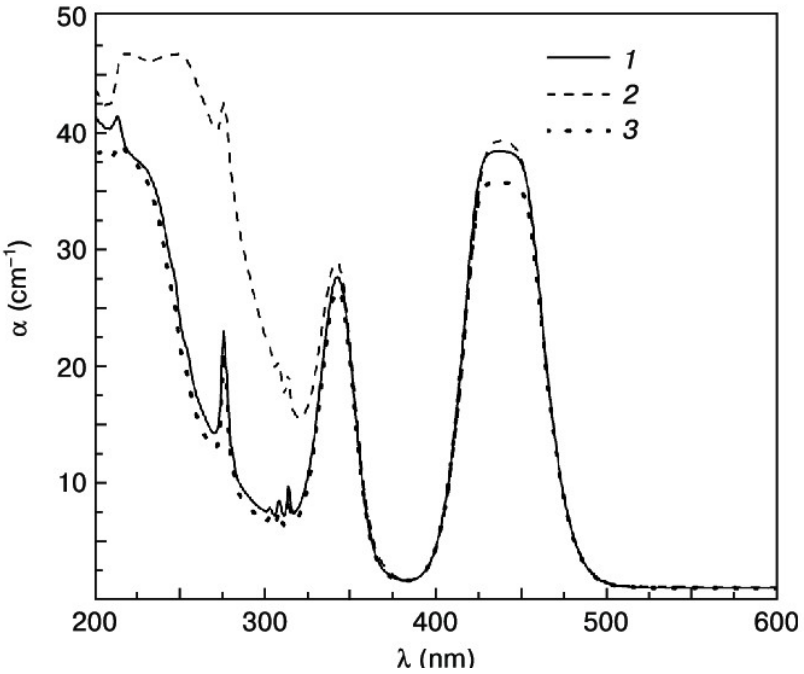

Figure 3.5: Absorption spectrum of the GAGG:Ce (line 1). The other two are the absorption spectra of GAGG:Ce-Ca (line2) and GAGG:Ce-Zr (line 3) crystals.

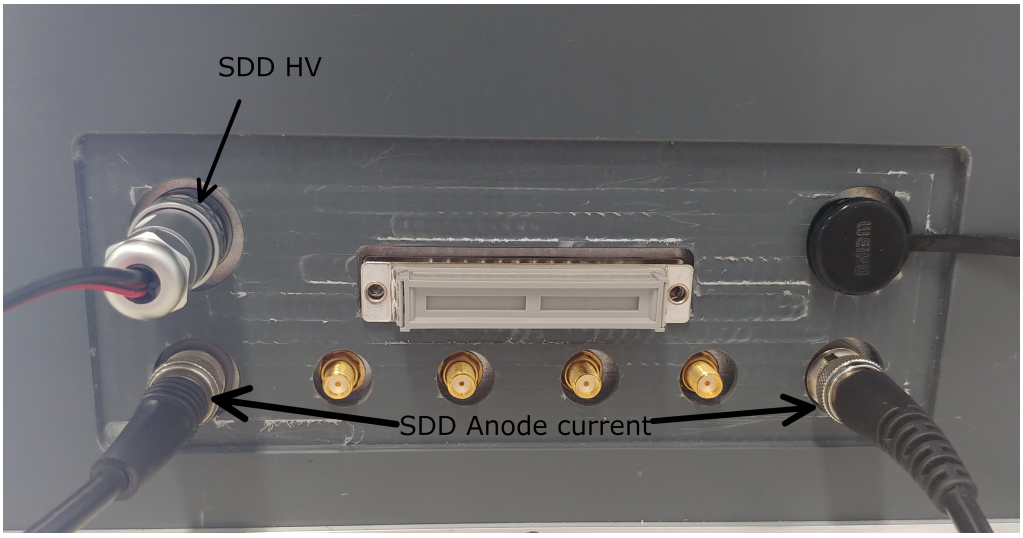

Figure 3.6: The connector panel. Only those used are marked, the others are to be used when using PCB channels equipped with preamplifiers and amplifiers.

covered with black tape once the cables were fed through them. The cables for the other connections would require larger holes which would harden the task to

keep the insides of the inner box dark. The solution to this problem is to use panel connectors directly fixed on the walls of the inner box and holes shaped slightly larger than the connectors on the walls of the outer box as described in Figure 3.6.

To provide the high voltage to the SDDs (125V) a BK PRECISION 9184B DC Power supply is used. The cable going from the generator to the connector panel is covered with a copper mesh to reduce the external noise. Since the SDD requires a negative voltage, the positive and negative wires are inverted inside the box.
To discuss the high voltage supply of the PMT, it is necessary to introduce another instrument that plays a crucial role in this experiment, the picoammeter TetrAMM produced by CAEN ELS (Figure 3.7) [40]. It was specifically chosen for its characteristics that fully meet the requirements of the experiment. More in details, it has four input channels, as the name suggest, that can be set on independently on one of two ranges: up to 120 nA or up to 120 µA. The four channels are sampled independently and simultaneously at a 100 kHz rate with a 24 bit resolution. The output rate can be reduced by changing the configuration of the instrument via software commands. To get the desired output rate the samples are averaged by the instrument, reducing also the measurement noise. The setup developed requires three input channels, one for the PMT anodic current, set to the high range, and two for the SDDs anodic currents, set to the low range. The TetrAMM features also a low noise integrated bias voltage source, that can go up to -2 kV, which is perfect for the PMT that requires a voltage of -1500 V. To conclude about the TetrAMM, it has an ethernet socket to transfer the current data to the computer since the memory space of the TetrAMM is limited.

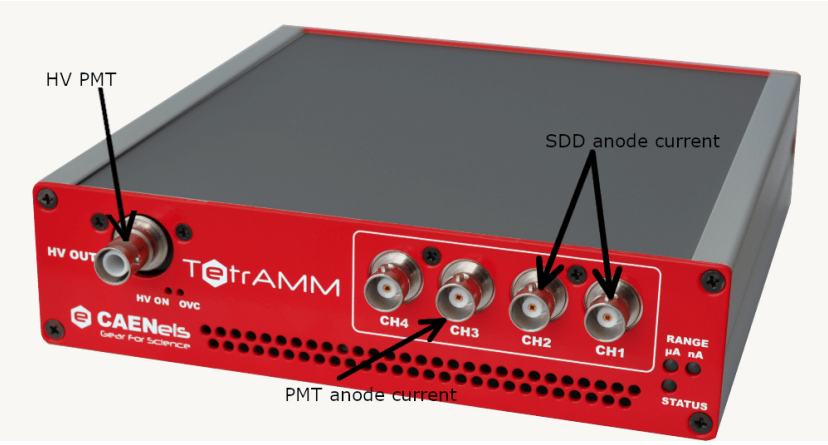

Figure 3.7: TetrAMM picoammeter and description of input and output channels.

Regarding the voltage generator for the LED, another practical solution was found, that solves this aspect and also the question of the central computer that

controls all the systems already presented and also those that will be presented in the following paragraphs. This is the role played by the Raspberry Pi 4 (kindly made available by Nicola Zampa). This model presents 40 pins, and two of them can generate a bias voltage of 5 V, perfect for the LED (5-7 V required). However, to control the LED intensity, that is to say to control the current that powers the LED, a pilot circuit is inserted inside the box, between the Raspberry and the LED. In its role of mini computer the Rasperry is connected via ethernet to the TetrAMM, to download the data acquired by the picoammeter, and to the PC, using one of the two USB sockets and an adapter USB-ethernet (see Figure 3.8 for details).

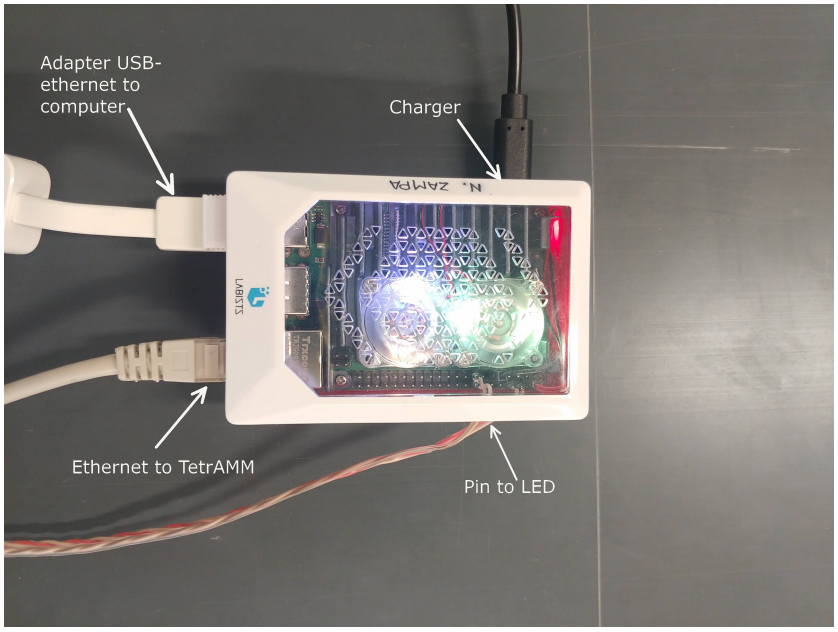

Figure 3.8: Raspberry Pi 4 and description of the connections.

The thermal aspect of the experiments plays a major role for the following data analysis. The knowledge and the control of the temperature is fundamental to better understand the afterglow dynamics. For this reason, in addition to what has already been reported to ensure thermal insulation, there is also a homemade cooling system. It consists in a Peltier cell, a 5L tank more or less half-filled with water, a relais, an aquarium pump, a spiral made of copper and several plastic pipes to connect all the instruments between themselves. The working principle of this cooling system is the following: the pump, inserted into the tank, circulates the water to the Peltier cell, where it is cooled down, to an heat exchanger, and back to the tank.
To reduce the thermal coupling between the ambient and the water circuit the

cooling system uses plastic pipes. The water tank is further insulated by thick plastic foam, while the other components use bubble wrap foils or expanded polyethylene. The heat exchanger is made by a copper spiral fixed externally at the aluminium box through metal hooks, centered with respect to where the PMT support is fixed. To increase the contact area between the spiral and the box, a two-component epoxy glue called "Acciaio liquido", with a good thermal transmission coefficient, is used to fill the spaces between the spires. Then a thermal grease (thermal conductivity 3.6 W/m·K) is applied between the glue and the box. The final result is shown in Figure 3.9.

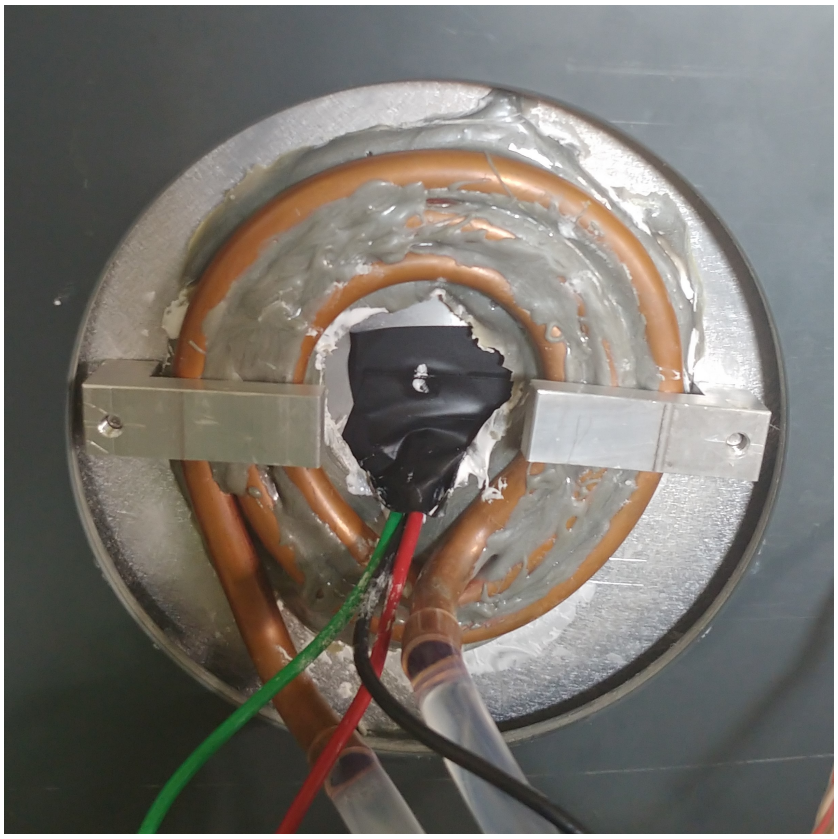

Figure 3.9: Final result of the spiral setup.

The Peltier cooler, produced by Hilitand, includes a ventilation system to cool the warm side of the Peltier cell. A 12V voltage is required to activate the Peltier mechanism, and it is provided using a PeakTech DC dual power supply 6145. To maximize the cooling, the voltage provided is close to 18 V.
The relais is positioned between the generator and the Peltier system. The relais control requires at least a 3V signal, that is provided through another mini computer like the Raspberry, the Phidget. Whether or not switching on the relais

depends on the temperature of the crystal compared to the required temperature, which is provided through a program executed by the Phidget. The Phidget setup developed for the temperature control is composed by the central board (computer) and two hubs connected to it: one is called Digital Output Phidget, and is responsible of switching on and off the relais, the other one Thermocouples Phidget. Four thermocouples are connected to the second hub: one goes inside the box to the hole provided in the cystal holder to make contact with the crystal, the second one is attached to the external box, another one measures the ambient temperature and the last one estimates the temperature of the water from the wall of the tank. The Phidget need to comunicate with the Raspberry in order to know if the PMT is switched on or off, since it generates heat (0.75 Watt). The comunication between the two is made through ethernet, but without a direct connection. A python program executed on the Phidget controls the Peltier cell by means of a clock signal with a fixed one minute period. The duty cycle of this signal is evaluated at the end of each period by the mismatch between the measured and desired crystal temperatures taking into account the temperatures measured by the other thermocouples.

Finally, the last piece of the experimental setup is represented by the collimator. It was only used during the irradiation steps with protons held in Trento. It is meant to be placed in front of the hole covered with solar filters in order to reduce the flux of protons and avoid a saturation of the TetrAMM channels while the SDD is measuring the scintillation light of the GAGG:Ce crystal. Since those two TetrAMM channels are set on the low range, the maximum current that can be measured is 120 nA.
The collimator consists of 3 pieces: two blocks with a square profile and a track on which they can slide (see Figure 3.10). The material is again chosen with a low atomic number in order to prevent the creation of too many radioactive nuclei. In this case the choice fell on polyethylene. The measures of the blocks and the small square hole in the middle were decided based on the characteristics of the proton source. Those are taken from the user guide of the Trento Institute for Fundamental Physics and Applications (TIFPA) or can also be found at [41]. Since the objective is to recreate a similar environment to the one that the detector will experience once in orbit, the energy requested for the protons is 70 MeV (also the lowest energy offered by the facility). Consequently, all the calculations must be made with the parameters of the beam for protons with this energy. In particular, the dimension of the beam profile, assumed to be gaussian and expressed either as the σ or the FWHM, are given at the isocenter (1.25 m from the source) so this is where the first block of the collimator will be placed. In this way, even if the beam will widen in the path from the first block of the collimator to the crystal, and so more proton will be stopped by the second block or will miss the crystal, at least

the SDD current will not saturate. Also, the distance is minimized as much as possible placing the second block in contact with the external box. The two blocks have sides equal to 8 cm in order to stop as much as possible the protons that are scattered very far from the center of the flux. They have a thickness of 5 cm to ensure that the protons that are not focused on the central hole will be stopped, and are put at a distance of 2.5 cm, going from the end of the first block and the start of the second. In this way, if there are any protons deviated inside the first hole, either they will be stopped by the second block or their trajectory does not reach the boxes.

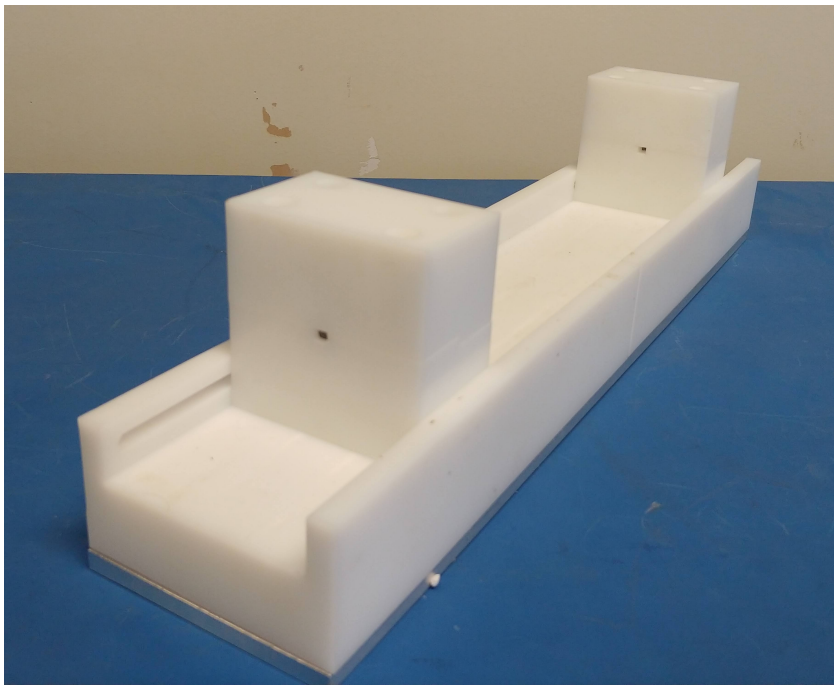

Figure 3.10: Collimator.

About the central hole, the dimensions, 4x5 mm^2, are calculated considering that the maximum current that should be measured by the SDD is 2/3 of the maximum range limit of the TetrAMM, so 80 nA, that each SDD cell is irradiated by only 25% of the scintillation light and that the SDD has an efficiency of 80%, that the light yield of the crystal is 53 photons/keV (this information was given by the producer for the crystals used in the previous campaign, that had different dimensions; from calibration tests reported also in this work, it seems that the actual value for the nominal crystals is lower, making this prediction a worst case scenario), and finally that the protons of the beam have an energy of 70 MeV, a flux of $7 \cdot 10^6$ protons/s and a FWHM of 16.2 mm. From these data it turns out that only 6% of the protons should be reaching the crystal, which is obtained with

a rectangular window with the dimensions written above.

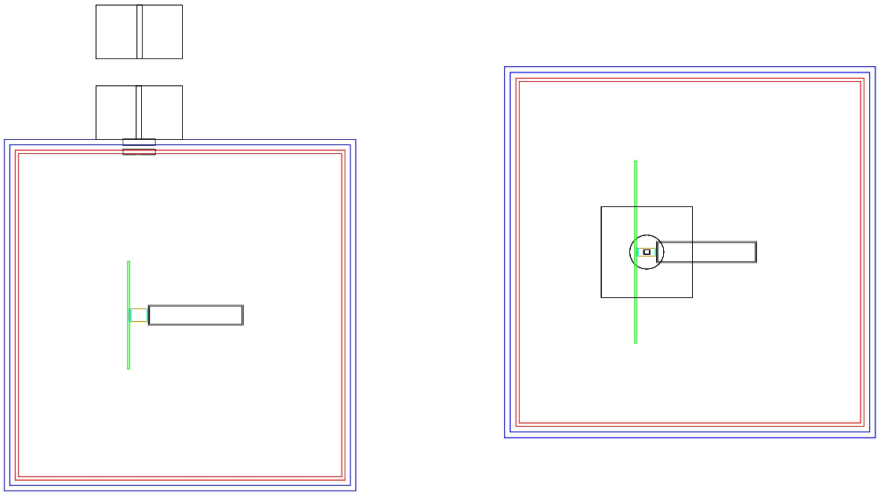

Figure 3.11: View in 2D of the geometry designed with Geant4, without light guide. The two boxes are shown in red (aluminium) and blue (PVC), the PCB in green, the GAGG:Ce crystal in yellow and the PMT in black. Outside there are the two blocks of the collimator, and in front of them the holes in the boxes. There are also the SDDs and the silicon mats but they are too thin to be seen here.

Throughout the development of the experimental apparatus, a simulation work of the same has been carried out to determine the best choice on some issues and verify the correct functioning. One of the first decisions, that required some preliminary tests, was either to optically couple the crystal with the PMT directly (with the silicon mat) or using a light guide. The possible necessity of a light guide was due to the proximity of the PMT to the protons beam. Not only the protons can damage the PMT but also secondary particles. On the other hand, using a light guide means losing part of the light of the afterglow. Since only 50% of the light goes to the PMT, and the PMT has an efficiency of about 6%, it is important to maximize the residual luminescence that reaches the detector. With this in mind, two simulations were carried out to demonstrate if the light guide is necessary or not. The simulations were done using Geant4, a software for the simulation of the passage of particles through matter, developed by several research institutes, first of all the CERN. It allows us to replicate a real scenario in all its details (geometries, materials, ...), also by creating very complex shapes and materials, and to simulate the interactions of the many types of particles. The coding is done in C++, but Geant4 has its own libraries. After recreating the principal actors of

this simulation and the materials they are made of, the simulated setup is ready and is shown in Figure 3.11. The PMT was represented in a simplified way, that is a cylinder of borosilicate glass and a thin layer of cesium for the photocathode. Also, for the simulation the shields protecting the PMT were removed, to consider a worst scenario situation. Also the crystal support structure was not reproduced, but this should not falsify the simulation since the beam collimation is made so that the support structure is not affected by the proton beam.
The important information to obtain are the kind of particles interacting with the PMT (and the SDD) and their amount, the energy distribution of these particles, but also the number of protons reaching the crystal, to verify that the collimator works correctly. The beam was reproduced using the information in [41].

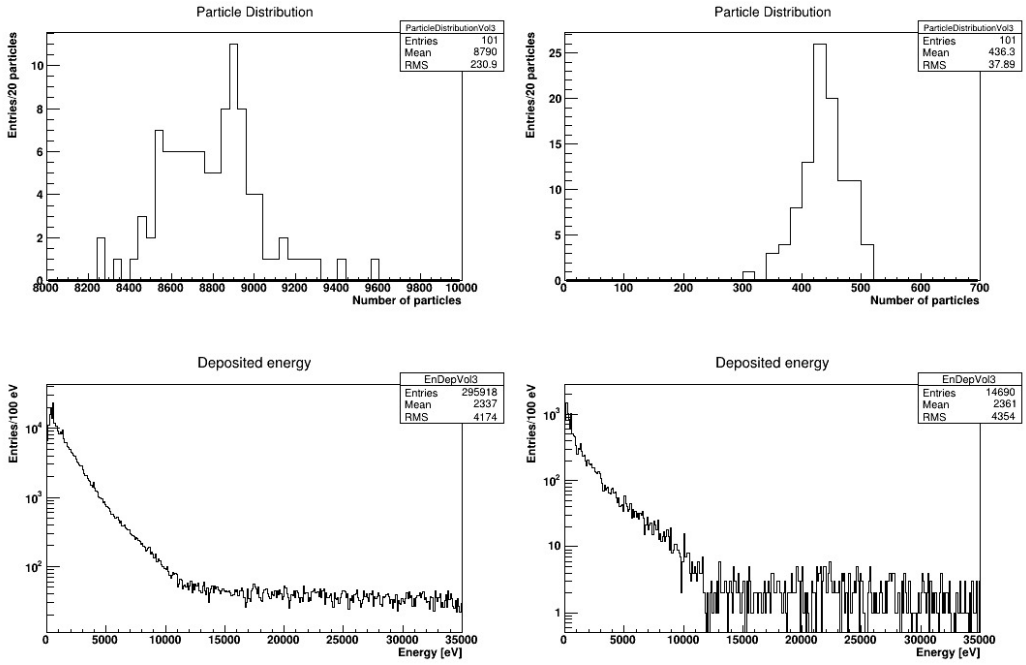

Figure 3.12: Set of plots showing the multiplicity of particles interacting with the PMT in the two cases, without light guide (left column) and with light guide (right column). In the first row, the number particles vs the number of runs with that amount of particles, in the second row the energy deposited by the particles in the PMT, considering putting together all the 10^8 particles. The energy range is limited up to 35 keV in the plots, but there are particles with energies reaching 60-70 keV

The first simulation done consisted in 100 runs of 10^6 protons. Both cases,

with and without light guide, were tested and the results are shown in Figure 3.12. These plots show a clear difference between the two cases. The number of particles reaching the PMT in the case with light guide is about 5% the number of particles without (436 ± 38 against 8790 ± 231 particles). This was pretty predictable since the PMT without light guide is much closer to the crystal, where the majority of the secondaries are created by the interaction of the primary protons with the crystal. The presence of the lightguide also represents a further obstacle for the secondary particles that try to reach the PMT. Those with lower kinetic energy are stopped within the lightguide. So, in the worst case scenario, with a flux equal to $3 \cdot 10^6$ protons per second, the PMT interacts with nearly 9000 secondary particles per second. However, what really matters is the kind of particles and the energy that these particles deposit on the PMT. A first idea of the energy of the particles reaching the PMT is already shown in Figure 3.12. The peak of energy in both cases is slightly less than 1 keV while the mean value for both case is 2.3 keV more or less. What really changes is the number of particles, which is generally a factor 20 higher in the case without lightguide (which corresponds to what was said in the previous paragraph). The two energy distribution are by consequence very similar. But these first two plots only show an energy range from 0 to 35 keV. Especially for the case without light guide, the energy range is wider.

Figure 3.13 shows both the number of particles and their energy distribution for each type of secondaries. From the results of the simulation, the majority of the secondary particles detected on the PMT are γ and neutrons for both cases. There is also a high number of electronic neutrinos, but they have a negligible probability to actually interact with the PMT, so they can be ignored. The simulation is made with 10^8 protons even if the amount of protons irradiated at the Trento facility is two orders of magnitude higher. However the time required to simulate 10^{10} protons is too high. The important information, like the mean energy of the particles, can be extrapolated even with a reduced number of simulated protons.
Looking now at the energy distribution, as it was already seen in Figure 3.12, the majority of the particles have energies lower than a few keV. Only a small amount of particles have energies as high as 70 keV. With these information it is finally possible to understand if there is any risk for the PMT, by comparing these results with what is shown in Figure 3.14.
It is clear that the secondary particles, although more important in number without the light guide, carry an energy that is too low to damage the PMT. The main damages that the PMT can suffer are on the borosilicate glass window, but they are caused by neutron or gamma-rays at higher energies than what was found (about tens of keV, compared to tens of MeV required to damage the PMT window). There is then no necessity for a light guide to be put between the PMT and the GAGG.
Another interesting data that can be obtained from this study, is how relevant is

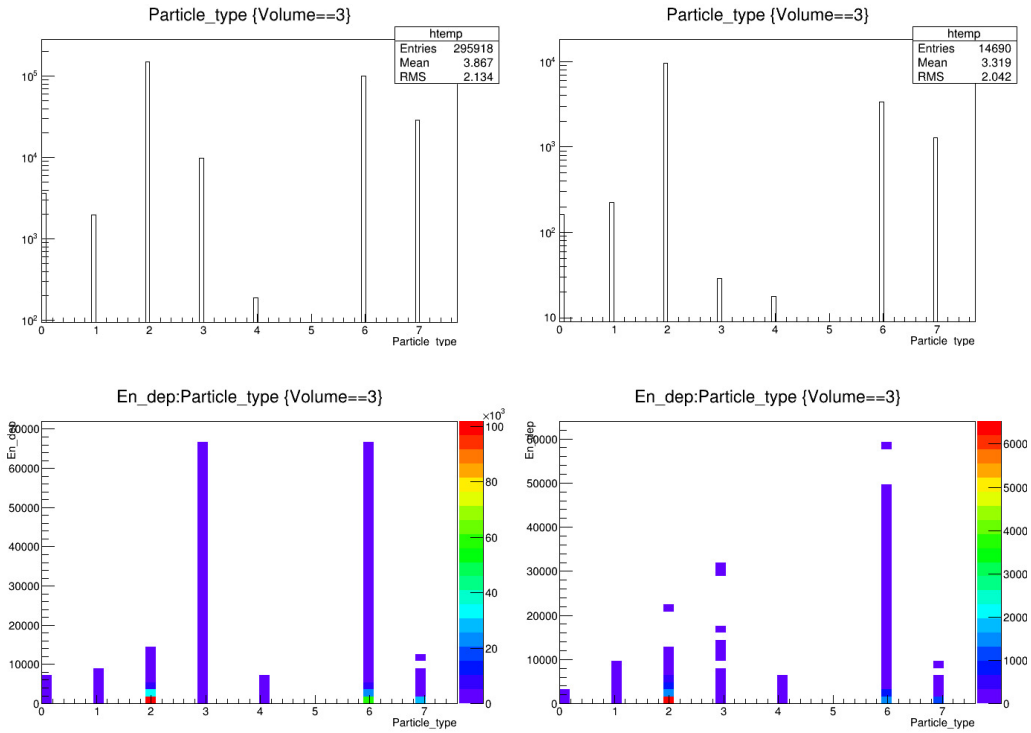

Figure 3.13: Set of plots showing the multiplicity of particles as a function of their type at first (first row), and then also of the deposited energy (second row), for the two cases, without light guide (left column) and with light guide (right column). The energy shown in the y-axis are in eV. Legend for the particles types: 0 = $\mu^{+,-}$, 1 = e^-, 2 = γ, 3 = p^+, 4 = e^+, 5 = $\pi^{+,-,0}$, 6 = n, 7 = ν_e.

the current generated by the secondaries that will be seen from the SDD during the proton irradiation. Only the study without light guide is reported here in Figure 3.15, since there are no major differences in the other case, which is pretty expectable since the situation of the SDD cells does not change. Considering the worst case scenario, which is all the secondaries interact with the SDD and all on a single cell, the energy deposited would be $3.37 \cdot 10^8$ eV. The energy required to generate an electron-hole pair is 3.6 eV, that is we would have about 93 milion pairs created. On the other side, the scintillation light of the 100 milion 70 MeV protons should generate $4.2 \cdot 10^{12}$ electron-hole pairs more or less (remember that only 6% of the protons reach the GAGG). This means that the secondary contribution is about 1/40000 with respect to the primary one, so it is negligible.

The last aspect that was explored with this simulation is the correct functioning

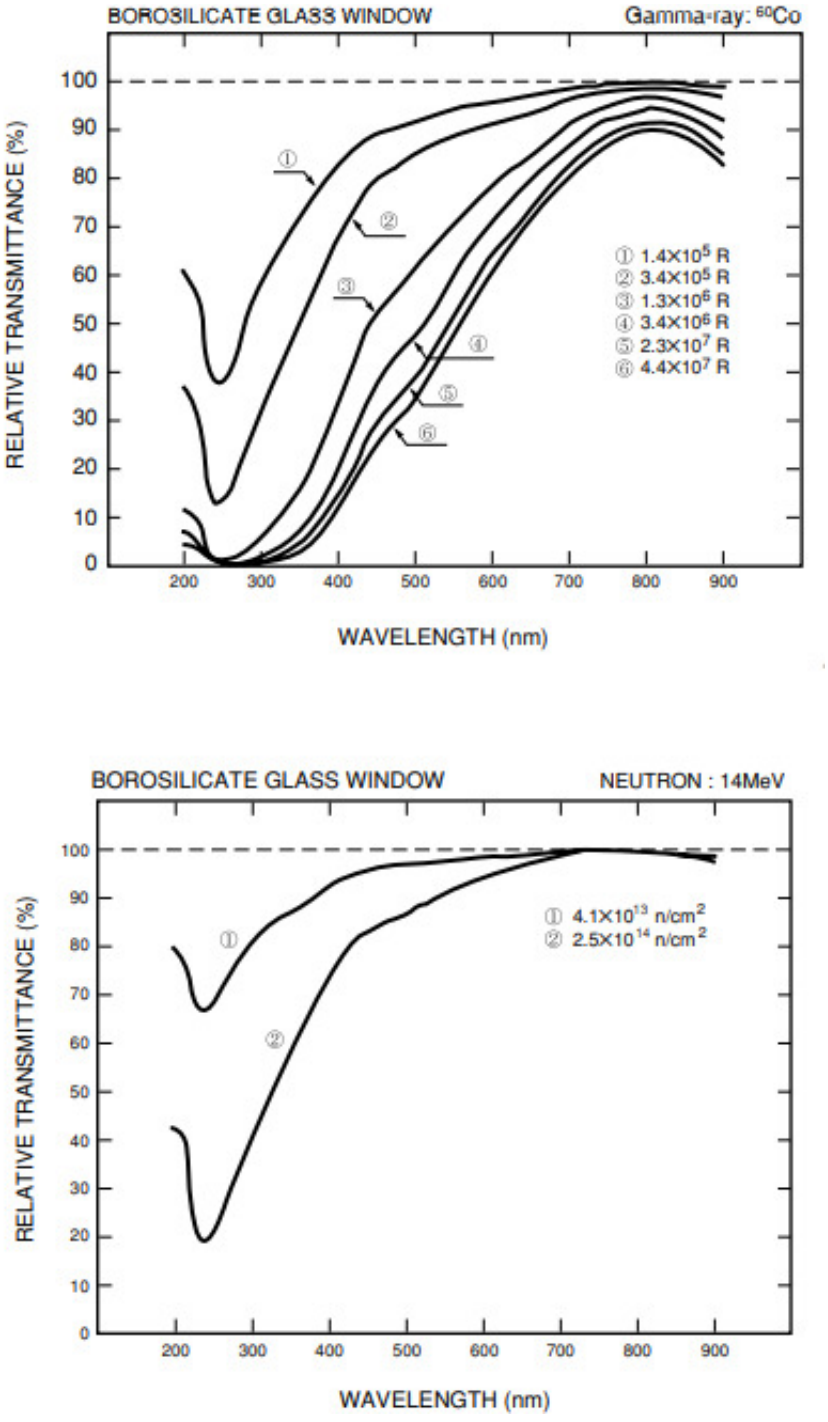

Figure 3.14: Radiation damage on the borosilicate glass of the PMT Hamamatsu r4125 [39].

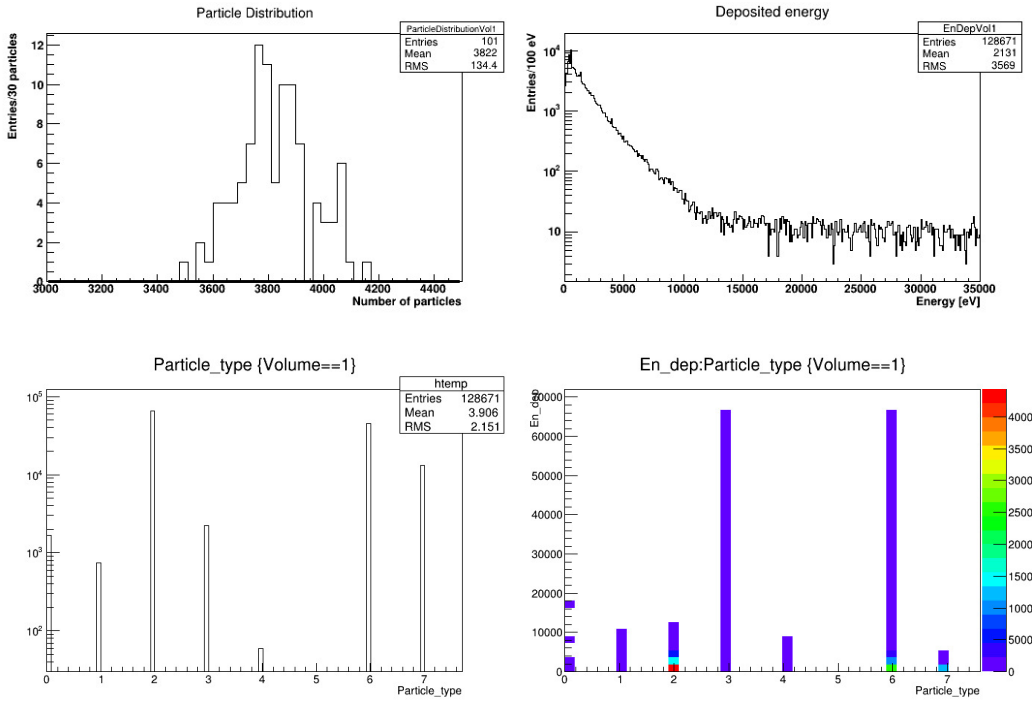

Figure 3.15: Set of plots showing the multiplicity of particles as a function of their type at first (first row), and then also of the deposited energy (second row), for the two cases, without light guide (left column) and with light guide (right column). Legend for the particles types: 0 = $\mu^{+,-}$, 1 = e^-, 2 = γ, 3 = p^+, 4 = e^+, 5 = $\pi^{+,-,0}$, 6 = n, 7 = ν_e.

of the collimator. As explained before not more than 6% of the protons emitted by the source at the Trento facility should reach the crystal, otherwise the SDD current may saturate the instrument. However, imperfections on the collimator could reduce the window that was calculated initially, so it is important to check that even with the imperfections the flux of protons does not reduce too much (it should be higher than 5%). Two setups were used for this test, both without light guide: the nominal case, with both holes aligned, 4x5 mm^2, and the imperfect case, where the holes are not perfectly aligned, and slightly smaller, 3.94x4.95 mm^2. These values were measured with an electronic caliper, as well as the maximum misalignment. In the nominal situation about 5.89% of the total protons irradiate the crystal, while in the case of the worst geometry it is about 5.32%. Both results are good. The first one is slightly under 6% because during that preliminary calculation the beam widening was not considered.

3.1.2 Empirical model

To explain the residual luminescence generated by the crystal after being irradiated, an upgraded version of the model described in [38] was used.
The long lasting luminscence, that characterize the GAGG:Ce scintillator, is due to the creation of metastable states in the crystal, due to intrinsic or impurity defects in the crystal lactice. Some of the charge carriers (electrons or holes) liberated by the ionizing radiation (photons or protons in this work) can be trapped in these sites, creating the metastable states that will decay over time, freeing the charge carriers. This can happen by different processes (e.g. to the conduction band by thermal energy absorption [42] or to nearby recombination centers by direct or thermally assisted tunneling [43]).
Ultimately all of the charge carriers recombine, mainly through radiative paths, giving rise to luminescence. From past experiments, and the tests performed for this study, it has been observed that the GAGG:Ce has an afterglow emission that may last up to several days, even a few weeks.

Since the crystal luminescence is measured starting several seconds after the end of each irradiation step, it is assumed that the trap species that contribute to it form a discrete set, not a continuum. Each metastable state is characterized by a mean lifetime (at least few seconds), a capture rate, and a fixed number of traps. The objective of the data analysis is to determine the number of species required to fit the data, and the value of the parameters that characterize each species of metastable states.
Another assumption made is that the distribution of all the traps is homogeneous inside the crystal volume, or varies very slowly in such a way that their density could be represented by an average value.

In [38] it was already shown that the best way to fit the afterglow current measured by the PMT, is to assume that the decay of the traps is exponential. This means that the equation that controls the number of occupied traps is:

$$\frac{dN(t)}{dt} = -\frac{N(t)}{\tau(t)} \tag{3.1}$$

where N is the number of traps that are occupied and τ is the mean lifetime of these traps. The decay of the excited metastable states may be mediated by absorption of thermal energy from the lattice vibrations (phonons). In such a case the mean lifetime depends on temperature through an Arrhenius like expression. Given the limited temperature interval experienced by the crystal during the experiment the lifetime temperature dependence can be expressed by the relation:

$$\tau_i(T) = \tau_{i,20} e^{-\frac{T-20}{k_{i,\tau}}}$$

where τ_{20} is the lifetime at a reference temperature, arbitrarily chosen at 20°, T is the temperature and k_τ is a coefficient that regulates the temperature dependence of the lifetime.

The main difference with the previous model in the article concerns the capture phase. When an ionizing particle interacts with the crystal, a large number of electon-hole pairs are generated. The capture of the electrons can happen either from a recombination center or by a trap with a lifetime large enough to be measurable in this experiment, or even by a trap that has a too short mean lifetime to be identified from the collected data. Assigning to each trap species and recombination center a propability of capture π, the probability that an electron is captured from the i-th species can be shown to be given by:

$$p_{\infty,i} = \frac{\pi_i d_i}{\sum_r \pi_r d_r + \sum_i \pi_i d_i}$$

where d represent the density of each possible capture center, the subscript i represent the traps species studied here and the subscript r includes both the recombination centers and the traps with too short mean lifetime. This equation is true only with the assumption, made by Dilillo et al., that the total number of traps that can be occupied by an electron is much larger than the number of charges actually captured. However, trying to fit the afterglow data obtained after irradiating the crystal with the LED light, it becomes clear that this assumption is not correct. So, the capture probability of the i-th species is redefined as follows:

$$p_i \approx \frac{\pi_i (N_{i,tot} - N_i)}{\sum_r \pi_r N_{r,tot} + \sum_i \pi_i (N_{i,tot} - N_i)}$$

where the subscript tot indicate the total number of capture centers for each species, i. e. the maximum number of traps that can be occupied.

Considering the GAGG:Ce a good scintillator, the majority of the charges recombine radiatively, so $p_i << 1$. For this reason, it is fair to make another assumption: the probability of recapture of a charge emitted by a decayed metastable state is negligible. Also, it allows to consider each species independently from the others.
Then, focusing on the i-th species, during an irradiation the number of occupied traps is given by the balance between the capture of the electrons and the decay of the metastable states already occupied.

$$\frac{dN_i(t)}{dt} = n_i \left[1 - \frac{N_i(t)}{N_{i,tot}}\right] \phi - \frac{N_i(t)}{\tau_i(t)} \tag{3.2}$$

where n_i is the capture rate of the i-th species and ϕ is the flux of the ionizing particles, considered constant in time.

It is possible to redefine the variable τ to simplify the equation. Defining τ' as:

$$\tau_i'(t) = \frac{\tau_i(t) N_{i,tot}}{N_{i,tot} + n_i \tau_i(t) \phi}$$

then the equation 3.2 becomes :

$$\frac{dN_i(t)}{dt} = n_i \phi - \frac{N_i(t)}{\tau_i'(t)} \tag{3.3}$$

which is similar to the one in [38], except for the τ' variable. Notice that the higher is the value of $N_{i,tot}$ and the closer the two value τ and τ' are. Instead the smaller $N_{i,tot}$ get compared to the other term at the denominator, the smaller τ' becomes compared to τ.

The solution of this differential equation is quite complex. Using Wolfram Alpha, this is the output:

$$N_i(t) = e^{\int_0^t -\frac{1}{\tau_i'(\xi)} d\xi} \left[\int_0^t e^{-\int_0^\zeta -\frac{1}{\tau_i'(\xi)} d\xi} \phi n_i d\zeta + N_{i,0} \right] \tag{3.4}$$

where $N_{i,0}$ is the number of occupied traps of the i-th species at the start of the irradiation.

Inserting this equation in the program that is going to fit the afterglow current is actually complicated to code and would take an enourmous amount of time to solve, because of the double integral. There is an assumption that can be made, to simplify equation 3.3, that is that the temperature is costant over small periods of time, like 1s. So instead of having one long irradiation, it can be divided in multiple small irradiation steps. In this way the temporal dependence of τ' in equation 3.3 can be removed, and the solution of the equation becomes a lot easier to process by the program.

$$N_i(t) = e^{-\frac{t}{\tau_i'}} \left[\tau_i' \phi n_i (e^{\frac{t}{\tau_i'}} - 1) + N_{i,0} \right] \tag{3.5}$$

In the solution 3.5, τ_i' has to be recalculated for every step of the irradiation, considering the mean temperature in that time interval, while $N_{i,0}$ will take the

value of $N_i(t)$ at the end of the previous one second irradiation.

This process is not required to solve equation 3.1. So, during period of only decay (i.e. no irradiation), the number of occupied metastable states is:

$$N_i(t) = N_{i,0} e^{\int_0^t -\frac{1}{\tau_i(\xi)} d\xi} \tag{3.6}$$

where $N_{i,0}$ is the number of occupied traps of the i-th species at the end of the irradiation.

With equations 3.5 and 3.6 it is possible to reproduce the behaviour of the metastable states during all the period of test for the i-th species. But the curve that must be reproduced by the fit is the afterglow current measured by the PMT. The current is generated by the radiative recombination of the electrons freed by the decayed traps, so it is proportional to the derivative of the equation 3.6.

$$I_i(t) = \frac{I_{i,0} e^{\int_0^t -\frac{1}{\tau_i(\xi)} d\xi}}{\tau_i(t)} \tag{3.7}$$

where $I_i(t)$ is the current measured by the PMT at time t due to the i-th species.

3.1.3 LED illumination

Once all the setup is ready and operational, the irradiation phase can begin. As anticipated, the first step to study the afterglow exploits an UV LED light, that is placed nearly in contact with the crystal. This test is planned in order to study the GAGG:Ce crystal behaviour in a situation where there is no radiation damage that could change its internal structure. The goal is to identify the set of traps that fits the data in the best way possible. This means finding the number of species, and then for each one of them the lifetime at a given temperature and how it varies with the temperature, the capture rate and the total number of traps available.

To do this, the LED irradiation phase is divided in two parts, both with the same amount exposition time to the UV light, but with two different temperatures. This is done in order to study the themperature dependence of the metastable states lifetime. Since this data acquisition is done in a clean room in Udine, that allows to maintain the temperature stable enough, and thanks to the cooling system described in section 4.1.1, that can maintain a fixed temperature within 7 °C from the room temperature, the range temperature that can be chosen for the LED test is quite large. However knowing that, the room at the proton therapy center in Trento, where the next phase of the experiment took place, has a temperature of 20 °C (more or less), it is better to stay close to that value. The final decision is to

set the internal temperature of the box at 18 °C in Trento, and consequently to set, for the test in Udine, initially a lower temperature (17 °C) and then an higher one (19 °C).
Multiple irradiation steps of different duration are scheduled for both temperatures. More in details, in both cases there are six irradiation steps the first day, and only one the second. Those on the first day have durations equal to 2, 5, 10, 20, 50 and 100 seconds, while the one on the second day lasts 500 seconds. Between the illuminations of the first day, one hour is waited in order to let the current measured by the PMT go back to only dark current or close to it, since there are metastable states with very long lifetimes, even as long as a few weeks, as it will be seen. Then after the single irradiation of the second day, ten days are left to pass before changing the temperature and doing everything again from the start. By the end, there are more or less 21 days of data collected. Having multiple irradiation steps of different duration is important for the fit to better estimate the parameters of the traps. From a mathematical point of view, it is complicated to fit multiple exponential decay, especially with the presence of noise. Changing the exposition time of the crystal to ionizing particles fills the metastable states differently, changing the contribute of each species in the total afterglow current and making it easier to identify them. Having multiple post-irradiation curves to fit provides also more data for the traps with a short and medium lifetime to improve their fit.

The data acquistion logic requires taking into account a number of factors to improve as much as possible the final result. As it was already pointed out, the SDD is always powered and acquiring data. This means that during the irradiation time it measures the scintillation current of the GAGG:Ce crystal. However, once the beam of ionizing particles ends, and the residual luminescence appears, the latter is too low to be measured by the SDD. This is why the PMT is necessary, but only to observe the afterglow. During the irradiation it must be powered off, otherwise it can be seriously damaged. It is clear that this two detectors must be synchronized, in particular to switch on and off the PMT at the right time. This is done by the Raspberry Pi 4, exploiting a program written in Python. Through the ethernet connection between the two instruments, there is an exchange of information going both sides. The TetrAMM sends the collected data to the Raspberry, while the Raspberry controls the configuration of the TetrAMM. So, from the data collected and immediately read, the Raspberry sees from the current measured by the SDDs if the crystal is being irradiated. The threshold is fixed at 1 nA. Before starting to irradiate the crystal, the PMT high voltage is switched off manually. The first time that the current measured by the SDD goes above the threshold, the high voltage is armed. Then, the moment the SDD anode current goes below the threshold, the TetrAMM high voltage is switched on at -1500 V. In this way, the

loss of information about the residual luminescence is reduced at the minimum (also compared to the previous study [38], where they waited one minute after each irradiation to switch on the high voltage of the PMT).

An aspect that has only been marginally mentioned is the dark current of the PMT. It has been said about its exponential dependece from the temperature, but the parameters of the equation are not known at the beginning. Another factor must also be considered in the equation. The TetrAMM picoammeter has been calibrated before shipment, but a measurement offset may still be present due non ideal insulation in the setup (cables, connectors, and so on). Since the currents that are to be measured are very small a change in offset could be expected every time the setup is modified. This offset must then be considered in every fit done as a parameter to be recalculated. So the equation to fit the dark current is given by :

$$I(T) = I_{20} e^{-k(20-T)} + O \tag{3.8}$$

where I_{20} is the current at 20 °C, k is the coefficient that describes the temperature dependence of the dark current, and O is the offset. Also, this expression has been simplified on consideration of the limited temperature interval experienced by the PMT.

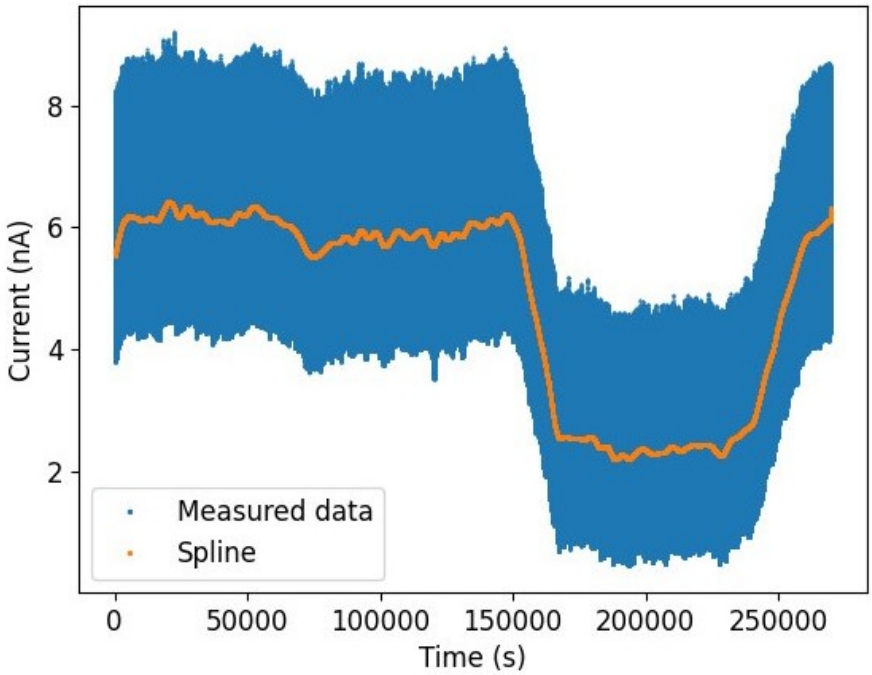

Figure 3.16: Dark current of the PMT. In blue the data collected by the TetrAMM at a frequence of 200 Hz, in orange the spline of the data, to simplify the fit.

Since the residual luminescence of the crystal lasts even for a few weeks, to study the dark current of the PMT the crystal must have been obscured for a period of time even longer. In this case, since for the first data used it seemed like there could still be some afterglow, a new set of measures of the PMT dark current at were taken several months after the last irradiation, using a larger temperature escursion. In Figure 3.16, the data showed has already undergone an initial screening. This is done selecting one minute of data at a time, calcultating the mean value and the sigma for each interval of time, and keeping only the data that is contained within $\pm 3\sigma$. Since the TetrAMM samples the current measured by the PMT with a frequency of 200 Hz, the amount of point to be fitted is still too high after the first screening and with too much fluctuation. Instead, a spline is made from the screened data set and then one point every 15 seconds is saved for the fit. To each point is associated a temperature calculated as the mean value for the 15 seconds interval straggling the time of the chosen point.

Using equation 3.8 to fit the spline in Figure 3.16, the best parameters found for the fit are the following (with the curve plotted on Figure 3.17):

$$I_{20} = 7.61nA \quad k = 0.098K^{-1} \quad O = -3.51nA$$

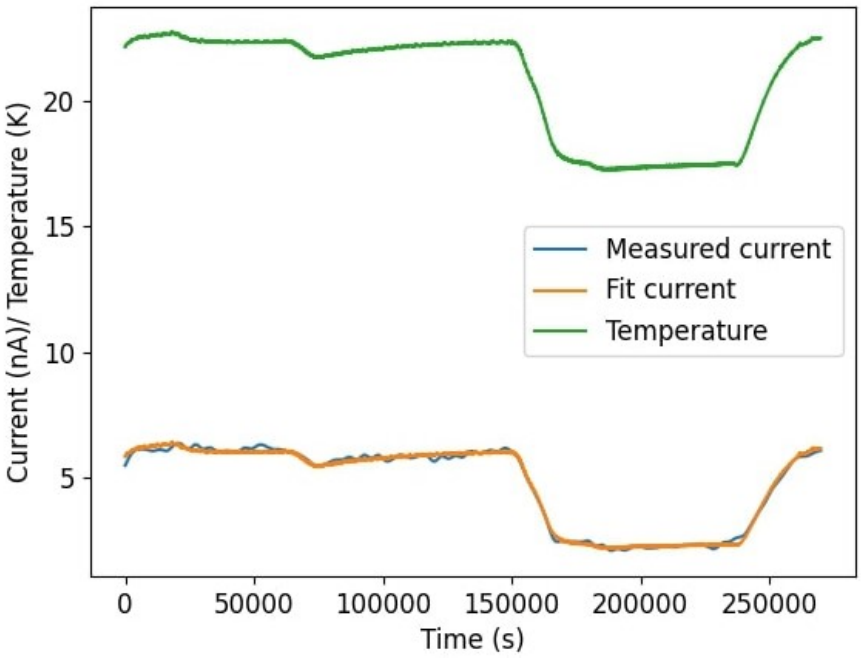

Figure 3.17: Plot showing the fit superimposed on the measured data. The temperature is also plotted, going from 17 °C to 22 °C, more or less.

The first two values are inserted in the fit of the afterglow, while the offset has to be recalculated. What was noticed during this analysis and also the one done on the irradiation tests is that the temperature of the crystal changes later than that of the PMT. The delay was estimated to be around 15 minutes. This is probably due to the heat exchanger being fixed on the same face of the aluminium box on which the PMT support is mounted. Consequently, for all the data analysis conducted from now on, two different temperature will be used: one for the PMT dark current, and one for the metastable states lifetime. It is the same set of data taken by the thermocouple fixed on the crystal, but it is shifted 15 minutes ahead to calculate the PMT dark current.

After the characterization of the dark current, the analysis on the data collected using the UV LED light can be started. An example of residual luminescence is shown in Figure 3.18.

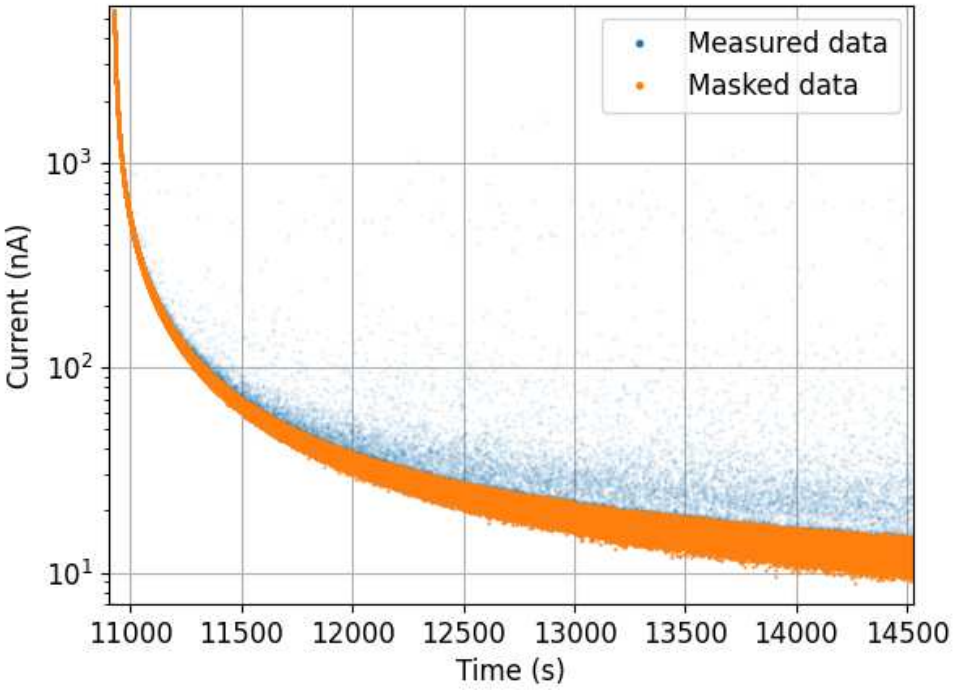

Figure 3.18: Example of the current measured by the picoammeter (in blue), after an irradiation of 20 seconds at 17 °C. In orange, the data contained within $\pm 3\sigma$. The few points that are very far from the 3σ limit are probably due to cosmic rays interacting with the GAGG:Ce crystal.

The preparation of the data that are then fitted using the model described in section 4.1.2 is the same as the one done for the dark current, except that instead

of taking from the spline one value of the PMT anode current every 15 seconds over 21 days (that would mean more than 10^5 points, making the fit process very long), this is done only for the first hour after the irradiation.Successively, the time gap between two values becomes one minute. This is possible because the afterglow current varies rapidly only in the initial minutes, where consequently it is necessary to accumulate more data. After one hour the variation is very slow, so it is justified to take one value of the current every minute. The fit remains quite long to process anyway.
One last thing to be pointed out about the data used is that even if the high voltage powering the PMT is switched on within one or two seconds from the end of the irradiation, it takes a few second for the high voltage to ramp up, and also after the peak of current measured the situation is still not fully stable. So in general it is better to use data that are taken about 15 seconds (but it depends from case to case) after the high voltage switch on.

Figure 3.19 shows the full afterglow current obtained during the LED irradiation phase. In the upper image it is possible to see an initial set of data taken two days before the beginning of the LED irradiation. This can help the fitting program to establish the number of traps of the species with the longest lifetime that could be already occupied before starting the study. Another information that can be given already now even if it is not visible in these plots, but it will be in the fit, is the presence of two gaps towards the end of the measurements. The first gap is due to a sudden error whose cause is not known. Instead, the second gap is due to memory of the Raspberry, being fully filled.

The current measured plays the main role in the fit, but it requires the help of other elements to obtain the correct interpretation of the phenomenom. For the fit program to work, you need to provide it with other information, like the temperature. For the part of the irradiation, the program needs to know the duration and the flux of photons reaching the crystal. Actually, the information required to run the python code is the number of protons, so it is necessary to convert the amount of photons that irradiate the crystal in their proton-equivalent amount. What was done was to compare the anode current of the SDD during one of the protons irradiation (where the flux of particles is known as it will be explained later) to the anode current generated during these irradiation steps done with the LED light. Finally, the information of the end time of the irradiation, which is provided by the SDD measurements as explained previously. It is important to be accurate since it affects strongly how well the short traps are fitted.

After several tries, in which the fit was progressively helped by fixing some parameters to find the correct values for other parameters, the best result was obtai-

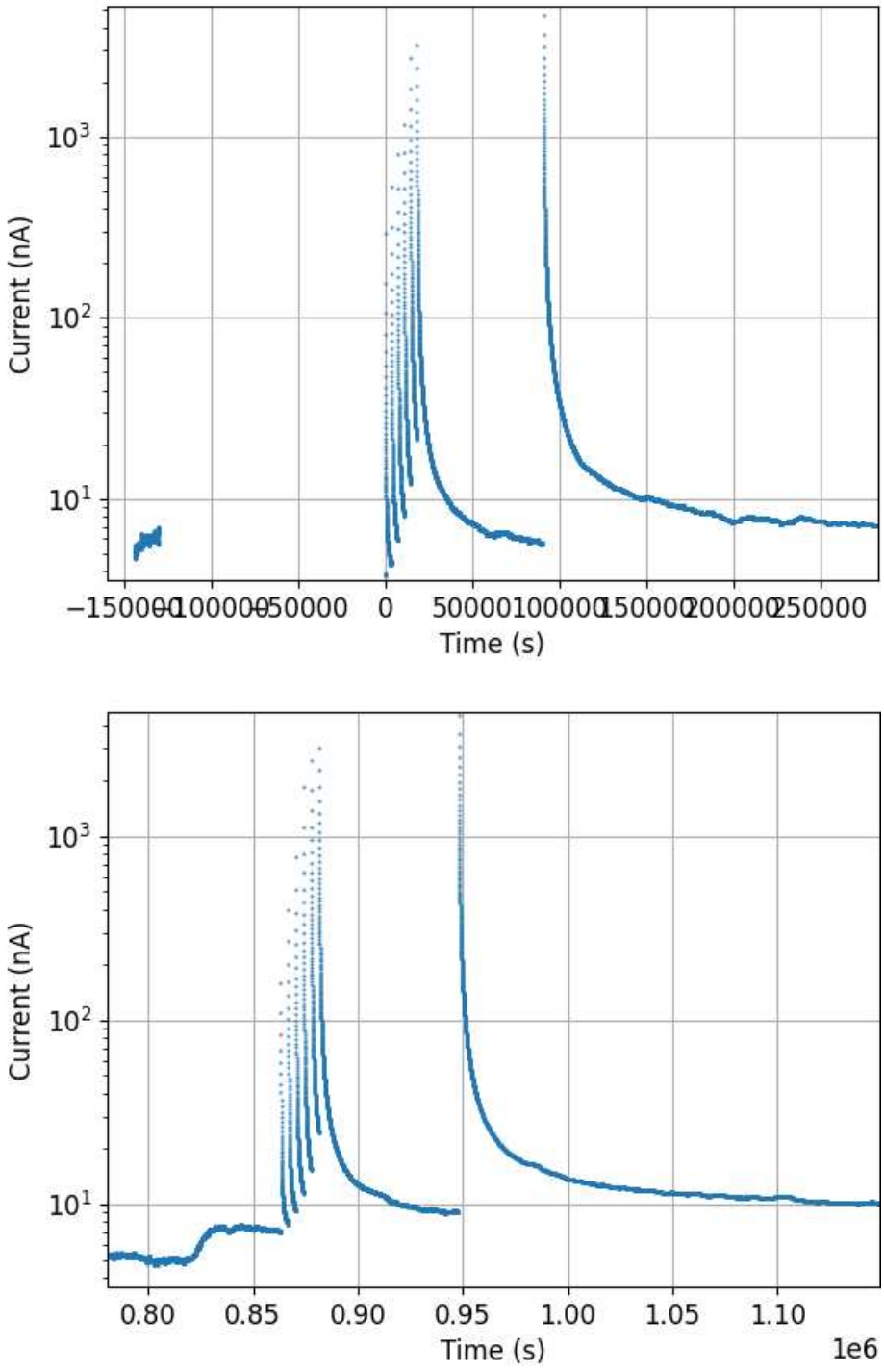

Figure 3.19: The afterglow generated by the crystal after every exposure to the UV LED light. On the upper image, the afterglow current generated at 17 °C, on the lower image at 19 °C. This is not the full data set, it was cut.

ned with a set of 8 traps which is described in Figure 3.20. In some cases a fit could seem better with more traps, but there was one or more pair of traps that were basically identical in lifetime, but with different capture rates (and in general one of the two was very low). In Figure 3.21 several plots are presented to show the fit result, followed by the residual plots.

	τ	σ_τ	T_τ	σ_{T_τ}	n	σ_n	N_{tot}	$\sigma_{N_{tot}}$
1st	17.86	0.1766	4.008	0.05875	1871.0	8.852	7.698000e+13	1.395000e+05
2nd	89.26	0.7802	8.266	0.16630	1821.0	9.605	6.752000e+10	5.732000e+08
3rd	296.00	1.7240	9.680	0.16670	1479.0	11.090	1.132000e+11	5.900000e+08
4th	1024.00	6.3970	6.460	0.09627	1136.0	6.358	1.276000e+11	6.654000e+08
5th	4684.00	34.4700	10.960	0.26950	799.4	5.290	1.492000e+11	1.310000e+09
6th	24330.00	270.4000	7.386	0.18540	683.1	6.051	1.245000e+11	1.672000e+09
7th	467800.00	10090.0000	27.100	3.22800	1758.0	50.960	5.875000e+14	5.132000e+04
8th	2723000.00	374600.0000	1.947	0.09965	9760.0	1377.000	2.022000e+12	1.917000e+11

Figure 3.20: Table listing all the traps parameters for the fit of the afterglow current generated during the LED irradiation campaign in Udine.

The fit gives generally a satisfying result but with a few things that should be pointed out. There is some difficulty in fitting the first data measured of the current generated by the afterglow after the end of the irradiation. This is due to an instrumental limit that does not allow to measure the current for previous times than those shown in the plots and therefore to have knowledge of the traps with lower lifetime than those found. This means that in the first currents measured by the TetrAMM there might still be a contribution from traps with very short decay time, but it is not possible to estimate this contribution with the acquired data. This aspect is well represented in Figure 3.22.
Another aspect is the temperature dependence of the lifetimes of the metastable states. Comparing the two situations, at 17 °C the fit is less precise than at 19 °C, especially for the metastable states with low mean lifetimes (again visible in Figure 3.22). This effect could be due to the fact that traps not accounted for in the model can give an appreciable contribution at 17 °C while being invisible at 19 °C due to the shortening of their mean lifetime. However it is interesting to notice that the transition between 17 °C and 19 °C is reproduced very well by the fit giving good hopes that the exponential parametrisation can achieve the goals of this study.
For information, the offset calculated by the fit is equal to -2.14 ± $2.13 \cdot 10^{-2}$ nA, while the initial number of occupied traps for the 8th trap is $2.58 \cdot 10^{11} \pm 3.85 \cdot 10^{10}$.

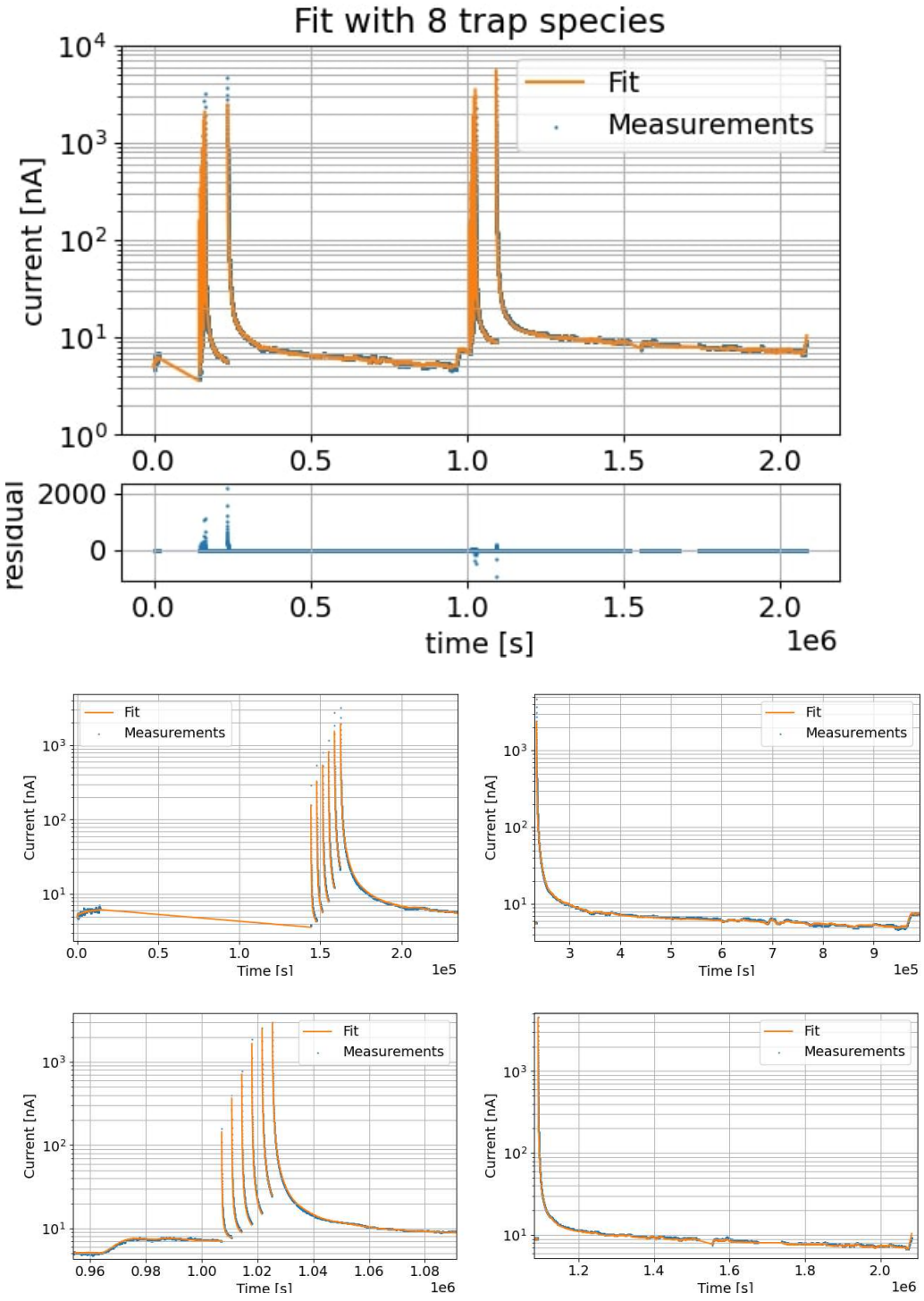

Figure 3.21: Several plots showing the fit of the full 22 days of measurements (top image), and the more detailed aspects of the fit in correspondence of the days with multiple irradiation steps (left column) when the low lifetime traps are more important, but also the single long irradiation (right column) when the longer lifetime traps play a major role.

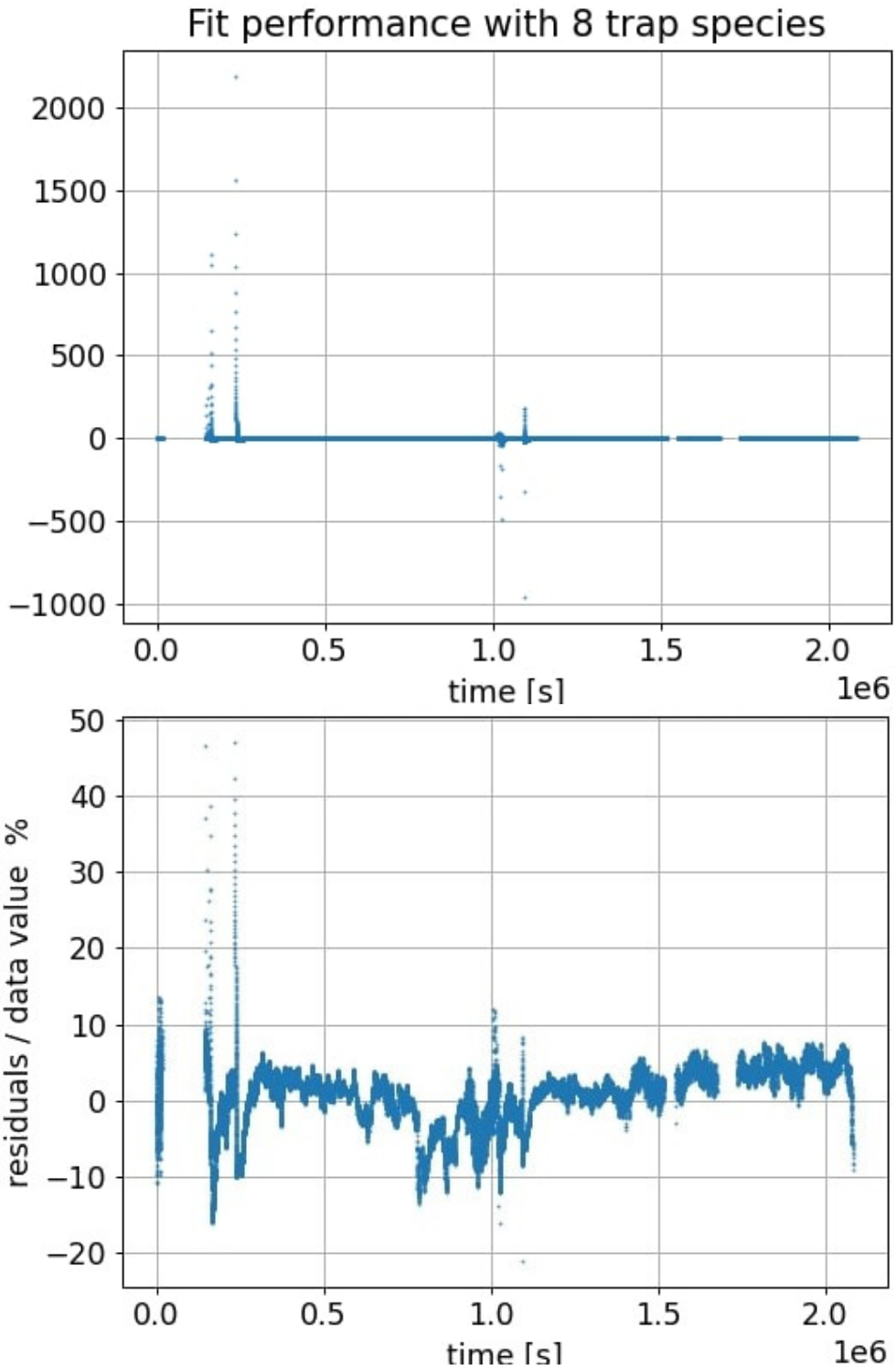

Figure 3.22: The residuals obtained from the fit of the LED irradiation campaign (top) and the percentage of the residuals compared to the actual data value.

With these promising results, it is possible to proceed with the analysis of the proton irradiation steps.

3.1.4 Proton irradiation

During the week long time spent at the Trento facility, a very precise schedule of irradiation was executed, that is reported in Figure 3.23. Between the proton irraditions of a single day, there was a wait of at least half an hour, but it could be longer. This because, being primarily a health facility, if there are some preparations to be done for the next day these obviously have the priority over the scientific work.

Day	Step	Step Beam time (s)	Cumulative Beam time per day (s)	Cumulative beam time (s)
Monday-1	Step 1	2	2	
	Step 2	7	9	
	Step 3	18	27	
	Step 4	30	57	
	Step 5	470	527	527
Tuesday-2	Step 1	30	30	
	Step 2	48	78	
	Step 3	67	145	
	Step 4	82	227	
	Step 5	800	1027	1554
Wednesday-3	Step 1	30	30	
	Step 2	130	160	
	Step 3	220	380	
	Step 4	1500	1880	3434
Thursday-4	Step 1	30	30	
	Step 2	2500	2530	5964
Friday-5	Step 1	30	30	
	Step 2	5600	5630	11594
Saturday-6	Step 1	30	30	
	Step 2	9600	9630	21224 ~ 5.9hours

Figure 3.23: Schedule of the irradiation steps done at the Trento Proton Therapy Center between February 28th and March 7th 2022.

The two longest irradiation steps (Step 2 of Friday and Saturday) had to be divided in several steps of shorter duration. This is because otherwise the neutron detector alarm would go off and shut down the source of protons for several minutes. It is necessary to make a small break ($\sim$ 5 minutes) after more or less 40 minutes of irradiation. After the last irradiation on Saturday, the apparatus was left to acquire data until Monday, so there is approximately one week of measurements taken.
Another aspect to take into account is that, even though the original plan was to make all the measuremntes at a temperature of 18 °C, the first day the irradiation steps were done at 19 °C, due to some delay in the preparation of the setup, and

consequently not having enough time to reach the pre-set temperature.
Finally, between the second and the third day, there was a malfunction of the system, so there are a few hours of data missing.

The analysis conducted on the data acquired during the proton irradiation steps, performed at the Trento Proton Therapy Centre, is very similar to the one used for the LED but with two main differences. The first one concerns the activation of the crystal: the interactions of the protons with the atoms of the crystal lattice generate new radioactive elements. The nuclear decays of these newly formed elements generates photons that are captured by the PMT together with the photons released by the metastable states. It is therefore important to separate these two events. However this is not always possible, in particular after irradiating the crystal for a long time (several minutes or more). This means that after long irradiation steps, the first tens of seconds, or even minutes, following the switch on of the PMT high voltage are unfortunately unusable. The effect of the activation can be seen in Figure 3.24, and compared to the situation after the LED irradiation represented in Figure 3.18, since the irradiation durations are similar. Keep in mind that this is only for ~20 seconds of irradiation, but the longest irradiation goes up to more than two and a half hours.

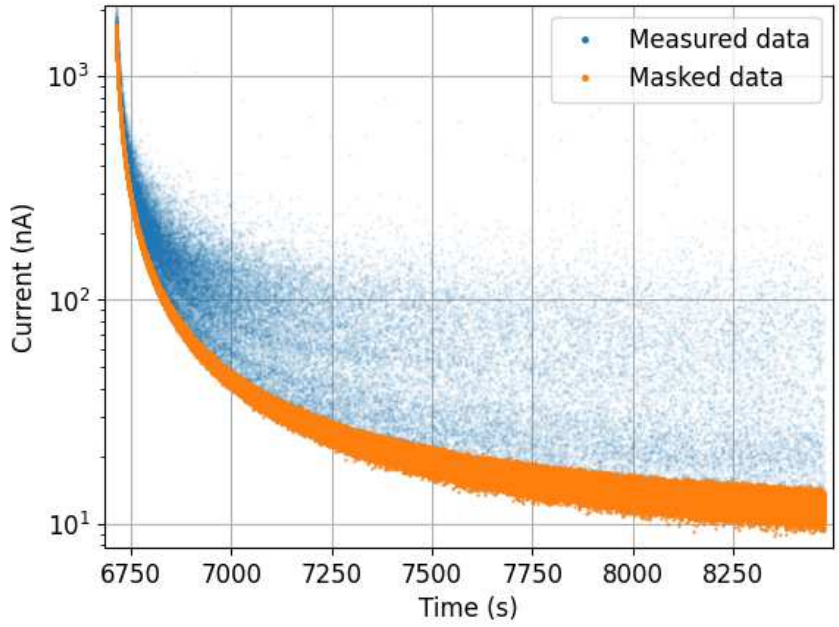

Figure 3.24: Example of the current measured by the picoammeter (in blue), after an irradiation of 18 seconds with protons. In orange, the data contained within $\pm 3\sigma$. The amount of values outside this interval is consistently higher than in Figure 3.18 because of the decay of activated nuclei.

The method used to separate the two components that compose the current measured by the PMT exploits the gaussian distribution that is expected for the values of the current generated by the afterglow. This means that in an ideal situation (i.e. without radioactive decay) the residuals of the current are centered on zero nanoampere. The residuals are obtained by subtracting a spline, made from the masked current showed in Figure 3.24, to the measured data. However, because of the activation of the elements inside the GAGG:Ce, the distribution of the measured current is no longer gaussian and the residuals tend to be negative due to an overestimate of the spline value in the regions where the contribution of the activation to the total current measured is important.

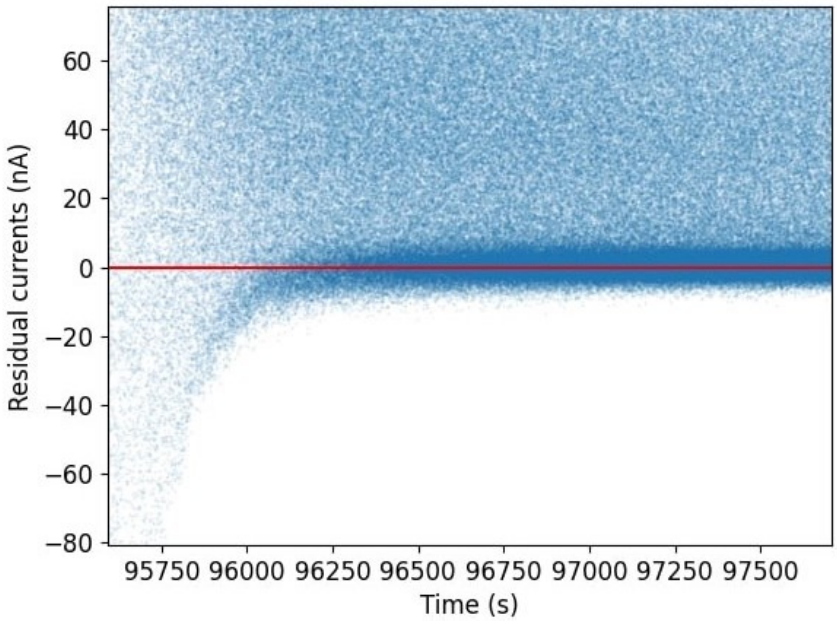

Figure 3.25: Residuals obtained from the current measured after the last irradiation on the second day at Trento.

An example is given in Figure 3.25. The most densely populated area corresponds to the afterglow current only, the other points have a radioactive contribution too. When the radioactive decay inside the crystal is low (after 96250 seconds in the plot) the residual currents of the afterglow is centered on zero. But before that time, the activation inside the crystal is large and the residuals of the afterglow current are not centered on zero anymore. Even further, going closer to the end of the irradiation, i.e. the start of the measurements, it becomes harder to identify what is the real value of the afterglow current. So, as anticipated before, these data must be left out. What needs to be done is to understand where it is possible to separate the contribution of the afterglow from the one of the activation, and from

there on to return the center of the residuals to zero.

The first operation to do is to divide the time of observation of the afterglow in several intervals that last one minute. The choice of the width of the time interval is determined by two conditions: the first one is that, especially for the first part of the analized data, the current is changing quickly, therefore taking more than one minute sized interval would put together data that are too different between each other in their composition of afterglow and activation current; on the other side, taking an interval that is too restricted would mean having little statistics. One minute seems a reasonable choice. However, because of the fast initial variation, the analysis is done moving the minute interval of fifteen seconds every time for the first hour after the end of the irradiation. After that, the interval is moved from one minute to the next one.
Now that the data are divided, it is possible to try to separate the current values that are affected by the activation from those that are not. As anticipated, the afterglow current is expected to have a Gaussian distribution. It was also found out during the analysis that the current due to the decay of newly formed elements in the crystal (added to the afterglow current) is well fitted using a convolution of a gaussian distribution with a gamma generalized distribution.

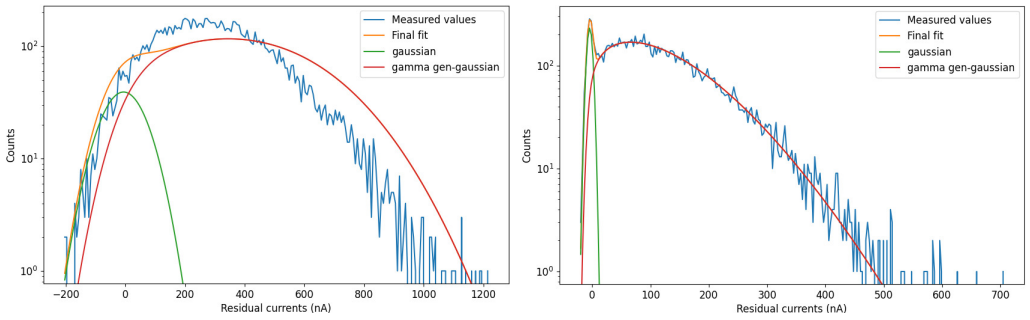

Figure 3.26: Examples of fit of the afterglow current values distribution. On the left side a failed fit attempt immediately after the end of the 800 seconds irradiation, while on the right side a successfull fit of the current distribution after $\sim$ 7 minutes.

Looking at the histogram of the values of the current measured by the TetrAMM two scenarios may arise (showed in Figure 3.26) while trying to fit it with the Gaussian distribution and the convolution described above: the gaussian fit works and it is possible to distinguish the afterglow current (right), or the fit fails because the activation is dominant (left).

The criterion chosen to determine whether the Gaussian fit works or not is the error on the Gaussian normalization parameter. If it is lower than 25% of the estimated value then the fit is considered good. In the end, the data of the current are kept from the first good fit after the last failed one.
A parameter that is used from this fit is the mean value of the Gaussian distribution, since it provide the information of how much the spline obtained is shifted to higher values because of the crystal activation. This will be added (since it is a negative number) to the initial spline. Actually, to be more sure about the correction to the residuals, the correction procedure is applied twice, the second time on the data already corrected from the first analysis. The final result, for the same case shown in Figure 3.25, is reported in Figure 3.27.
The last two information that are taken from this analysis are the statistical error and the systematic error in each point that will be used for the fit. The first one is obtained by the error returned by the program on the mean value of the fitted gaussian. The second one instead is equal to the second correction applied to the spline. This is because there is no guarantee that the deviation of the spline from the zero is equal for all the points in the minute interval taken into account, so the error made with the second correction could be equal to the correction itself. The two error, statistical and systematic, are then summed in quadrature.

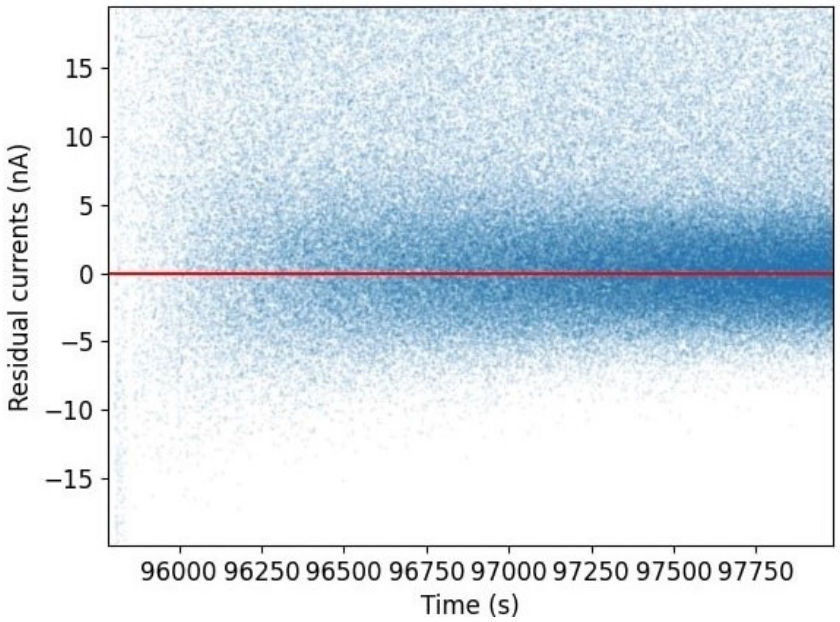

Figure 3.27: Residuals obtained after the two step correction for the current measured after the last irradiation on the second day at Trento. The different start time of the residual currents compared to Figure 3.25 is due to the discard of the first ~ 250 seconds because of the radioactive decay.

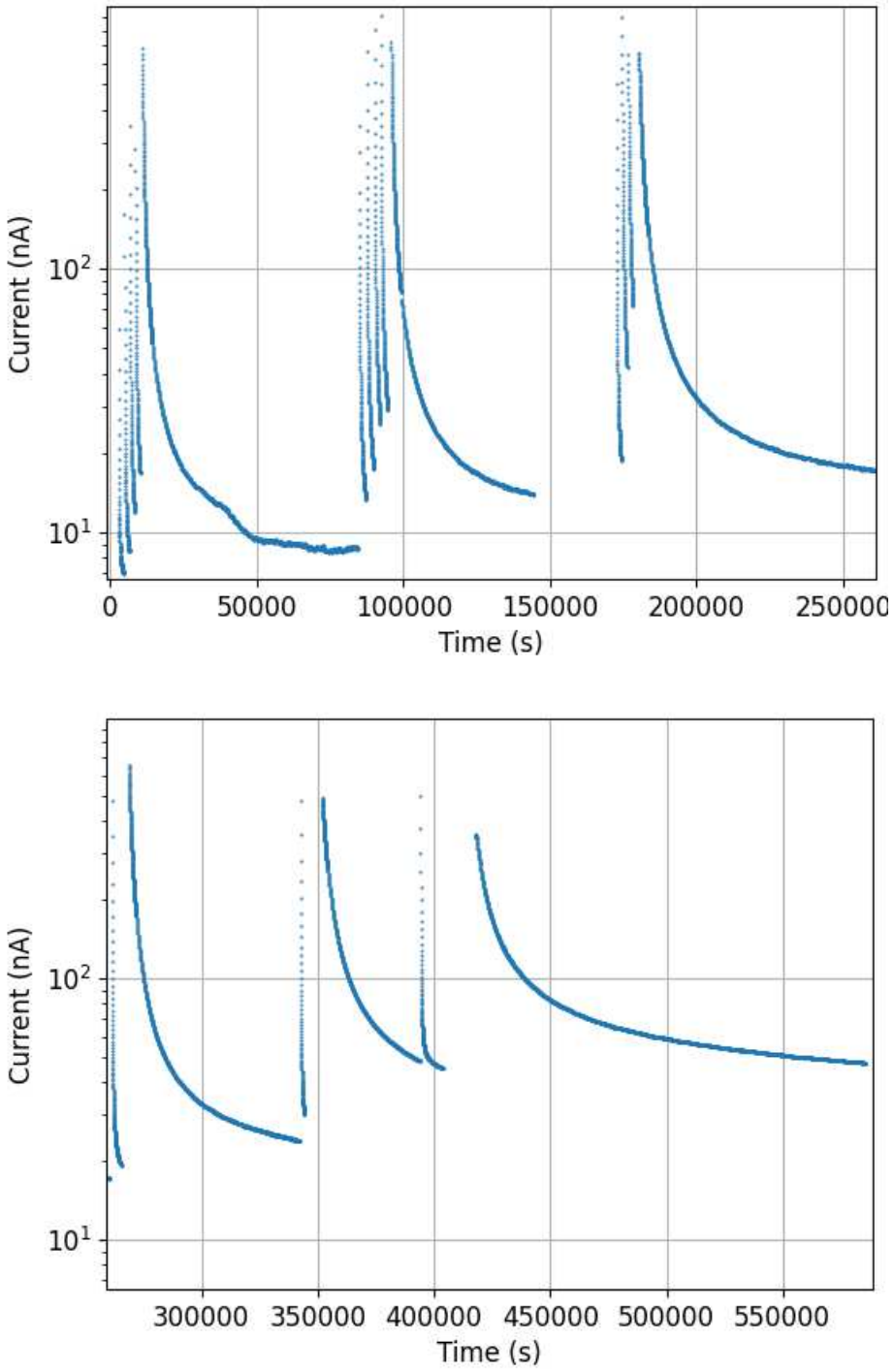

Figure 3.28: The current due to the afterglow generated by the crystal after every exposure to the protons beam. On the upper image, the afterglow current generated during the first three days, on the lower image the one generate on the following four days.

This data cleaning operation is done throughout all the week of measurements. In this way the correct current generated by the afterglow is obtained and can be fitted (Figure 3.28).

The second difference, compared to the fit done for the LED irradiation, is the introduction of a new parameter in the fit, the absorption coefficient. This parameter represents the formation of colour centres, crystallographic defects where an ion is missing from its regular lattice position, due to the energy transferred to it from the interaction with high energy particles (in this case the 70 MeV protons). In general, this causes the displacement of the ion in an interstitial position and creates a vacancy. This two new features are responsible of the absorption of part of the afterglow emission, that will not reach the PMT. So the measured current is actually lower than residual luminescence that is actually emitted from the crystal. The fit must take it into account, and tries to estimate the value of this parameter. However, the value of the absorption is not expected to be very high. This is because the absorption spectrum of the colour centres is predominantly centered on the UV light, while the light emitted by the crystal has higher wavelengths. So only a very small part of this light is expected to be absorbed [44].

In this case, for the proton flux there is a file, given by the facility, that registers the proton fluence, measured before the collimator, emitted by the source in the direction of the crystal every 0.2 seconds. This value has to be corrected because of the presence of the collimator. Actually, the value provided in the file is not the actual number of protons, but there is a multiplicative factor that has to be applied. Studying the behavior of the source of protons, it seems correct to assume the flux as constant during each irradiation, since the flux standard deviation is less than 1% of its mean value. This approximation could generate some fit difficulties on the mestastable states with low lifetimes if the final flux value is very different from the mean value used.

The species of traps are expected to be same as those calculated in the previous fit with the LED. So the mean lifetime and the temperature coefficient should remain the same for both cases. What is going to change is the capture rate since different processes occur when the crystal is irradiated with protons or with photons. Also, since the duration of the measurements was significantly shorter compared to the LED tests, it would be more difficult to find the parameters of the longer traps. The other parameter that is left to vary is the total number of metastable states available. Even if the illumination flux measured by the SDD is higher than the irradiation flux used at the proton therapy center, the duration of the former is significantly lower. This means that during the LED phase the amount of traps involved, especially for the species with lifetime higher than the

photon irradiation duration, might have been significantly lower than their total number, making it difficult for the fit program to find the actual value for N_{tot}. This parameter can be improved by this second analysis, having an irradiation lasting as long as two hours and forty minutes. The final parameters and shape of the fit are presented respectively in Figure 3.32 and Figure 3.30.

	τ	σ_τ	T_τ	σ_{T_τ}	n	σ_n	N_{tot}	$\sigma_{N_{tot}}$
1st	17.86	0.1766	4.008	0.05875	1711.0	6.093	5.716000e+10	4.443000e+09
2nd	89.26	0.7802	8.266	0.16630	1151.0	2.182	6.310000e+10	1.589000e+09
3rd	296.00	1.7240	9.680	0.16670	870.3	1.008	9.845000e+16	3.005000e+01
4th	1024.00	6.3970	6.460	0.09627	811.4	0.944	3.156000e+11	2.232000e+09
5th	4684.00	34.4700	10.960	0.26950	586.8	0.707	2.220000e+12	5.974000e+10
6th	24330.00	270.4000	7.386	0.18540	523.2	1.021	6.162000e+11	2.796000e+09
7th	467800.00	10090.0000	27.100	3.22800	1667.0	8.570	9.274000e+16	1.073000e+04
8th	2723000.00	374600.0000	1.947	0.09965	7770.0	108.300	9.254000e+12	2.611000e+11

Figure 3.29: Table listing all the traps parameters for the fit of the afterglow current generated during the proton irradiation campaign at TIFPA.

The fit represents very well the curve of the current measured by the TetrAMM. As for the LED case, the major difficulty arises while fitting the initial rapidly decaying part after each irradiation. However this happens only for the shorter irradiation steps. For the longer ones the first minutes are removed as explained before, so this problem has no impact on their fits. However, because of the difficulties in fitting the early moments after the short irradiation steps, also the traps with a medium mean lifetime ($\sim 10^3$) are affected, and try to compensate. Since the lower lifetime metastable states tend to underestimate the afterglow current, the medium one are fitted trying to increase the current. This is why after the long irradiation steps (the last one of each day) the residuals (Figure 3.31) are negative at the start.
Regarding the other parameters fitted by the program, the offset in this case is -0.804 ± 1.53 · 10^{-2} nA (it changed from the LED fit since all the setup was disassembled and reassembled in the meantime) and finally 7.796 · 10^{11} ± 1.603 · 10^{10} traps of the longest lifetime species are occupied at the start of the acquisition of data. The absorption coefficient returned by the fit is basically zero ($\sim 10^{-26}$). It is not clear if it is due to the reason given before to jusitfy a priori the expected low value, or if there is no absorption at all. Since the PMT is sensitive only in the low wavelength region of the GAGG:Ce emission spectrum, where most of the absorption takes place, while the SDD cells cover the whole spectrum, an even smaller effect is anticipated for the nanosatellites during their mission.

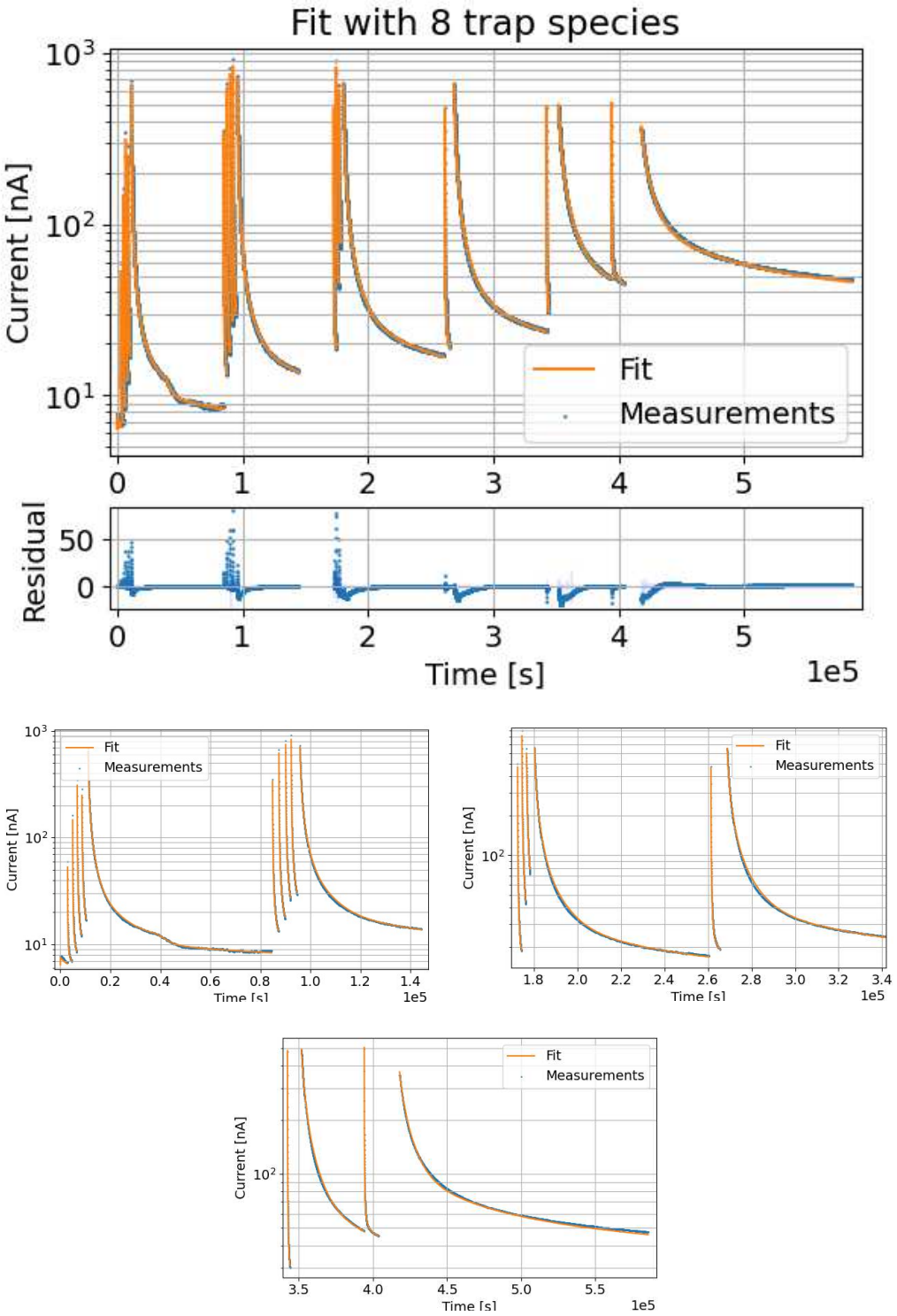

Figure 3.30: Several plots showing the fit of the full 7 days of measurements (top image) with the residual, and the more detailed aspects of the fit by taking two irradiation days at a time.

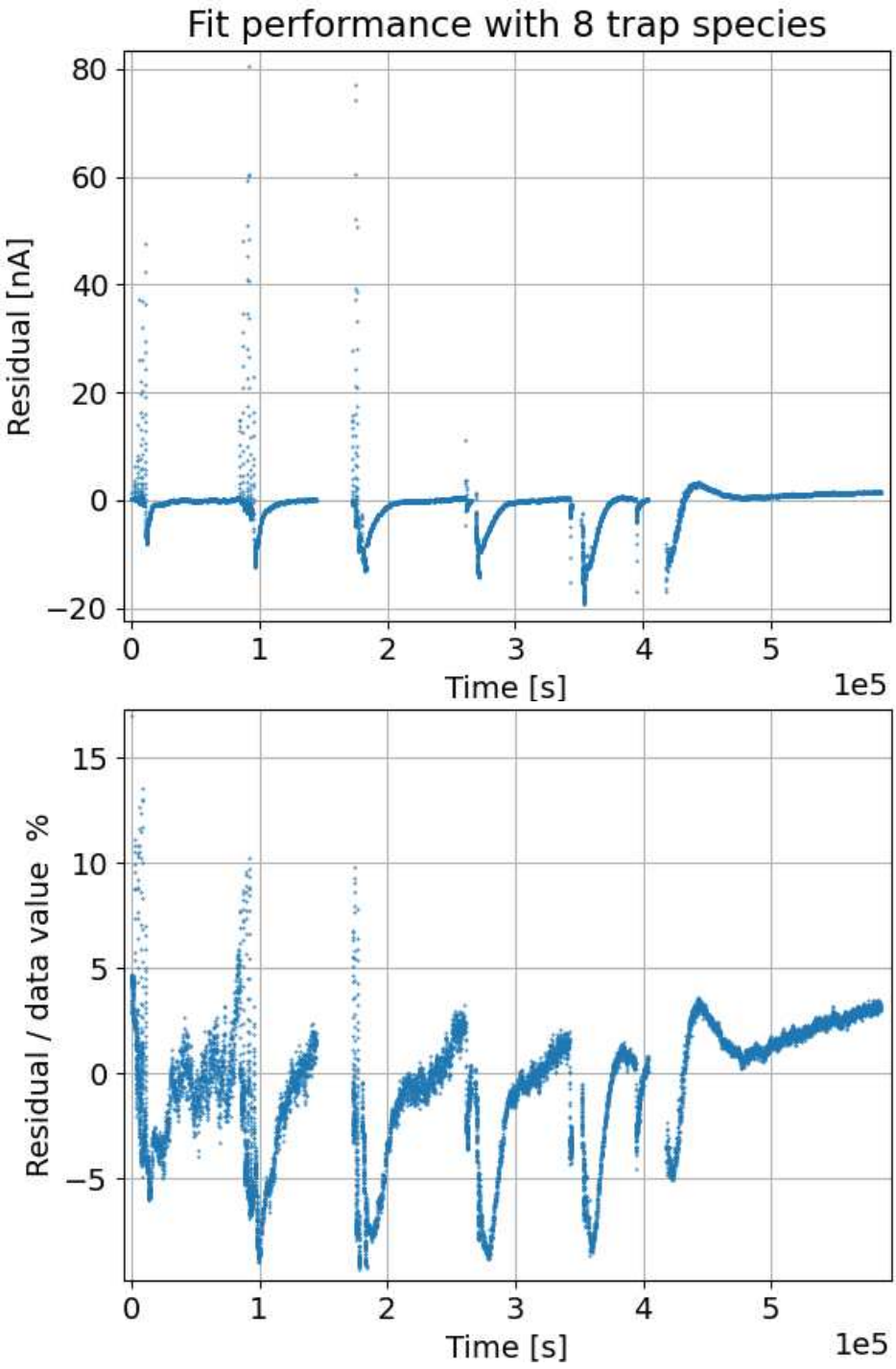

Figure 3.31: The residuals obtained from the fit of the proton irradiation campaign (top) and the percentage of the residuals compared to the actual data value. The blue shadowed region represent the ± 3 σ region obtained from the statistical and systematic errors of each data.

From the residual plots it is possible to see that, even if the residuals are not always contained within the 3σ region, they are reasonably small (<10%) compared to the measured value. The fact that the residuals are lower than in the case of the LED should not be too much a surprise, since the worst part of the fit in the LED case concerns the first seconds after the illuminations. In the case of the protons, the first measured after each irradiation used for the fit is generally taken at least several second later than in the LED case.
It is also important to keep in mind that this fit was done using an empirical model, that carries with it some approximations. And this is added to the instrumental limitations already described in previous discussions. So it is understandable that the fit still presents some errors. Keeping all of this in mind, it is satisfying to see how good the results are. One last fit is presented (shown in Figure 3.33) to demonstrate that, using the more accurate N_{tot} value obtained from the proton irradiation study to fit the afterglow measured during the LED tests, the fit still provides good results, with the limitations described earlier, while finding new values for the capture rates. In conclusion, the model describes satisfactorily the residual luminescence generated by the GAGG:Ce crystal, and can be used to make some predictions about the behaviour of the crystal once in orbit.

	τ	σ_τ	T_τ	σ_{T_τ}	n	σ_n	N_{tot}	$\sigma_{N_{tot}}$
1st	17.86	0.1766	4.008	0.05875	1888.0	2.986	5.716000e+10	4.443000e+09
2nd	89.26	0.7802	8.266	0.16630	2170.0	5.432	6.310000e+10	1.589000e+09
3rd	296.00	1.7240	9.680	0.16670	1057.0	1.900	9.845000e+16	3.005000e+01
4th	1024.00	6.3970	6.460	0.09627	1420.0	3.136	3.156000e+11	2.232000e+09
5th	4684.00	34.4700	10.960	0.26950	447.7	1.372	2.220000e+12	5.974000e+10
6th	24330.00	270.4000	7.386	0.18540	557.7	2.122	6.162000e+11	2.796000e+09
7th	467800.00	10090.0000	27.100	3.22800	1511.0	7.665	9.274000e+16	1.073000e+04
8th	2723000.00	374600.0000	1.947	0.09965	4218.0	26.570	9.254000e+12	2.611000e+11

Figure 3.32: Table listing all the traps parameters for the fit of the afterglow current generated during the LED illumination campaign in Udine, using the N_{tot} values obtained for the proton irradiation fit.

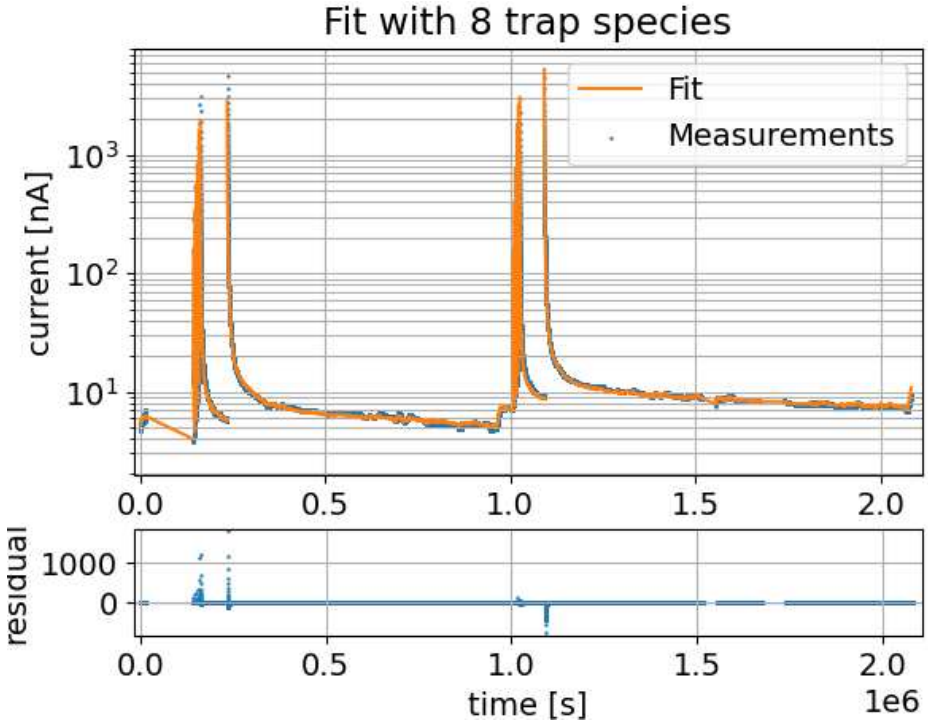

Figure 3.33: Fit of the full LED irradiation campaign after fixing N_{tot} to the values obtained from the proton irradiation fit.

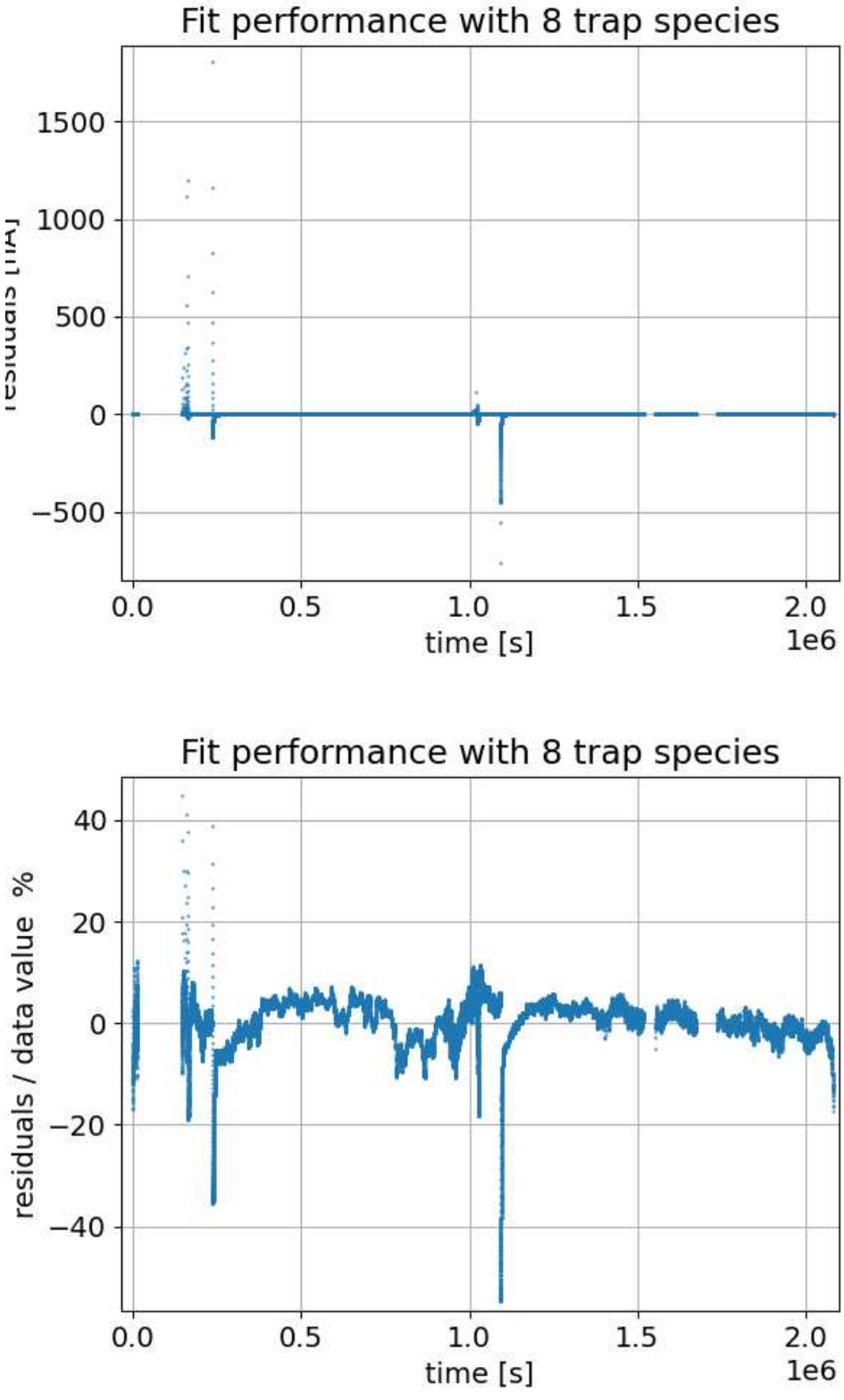

Figure 3.34: The residuals obtained from the fit of the LED irradiation campaign (top) and the percentage of the residuals compared to the actual data value after fixing N_{tot} to the values obtained from the proton fit.

3.1.5 Effects on the HERMES Pathfinder nanosatellite

The first small fleet of HERMES Pathfinder nanosatellites, that hopefully will be launched within a year or so, will fly around the Earth at an altitude of 550 km on an equatorial orbit. Once in the space, the nanosatellites, and hence the crystals, will be affected by the energetic charged particles (protons and electrons mainly) trapped in the Van Allen belts [45]. Flying on a Low Earth Orbit (LEO), the major concerns for the detectors are caused by the South Atlantic Anomaly (SAA), a region located over the south portion of the Atlantic Ocean (as the name suggest), where the inner Van Allen belt is closer to the Earth surface due to an anomalously weak magnetic field (Figure 3.35).

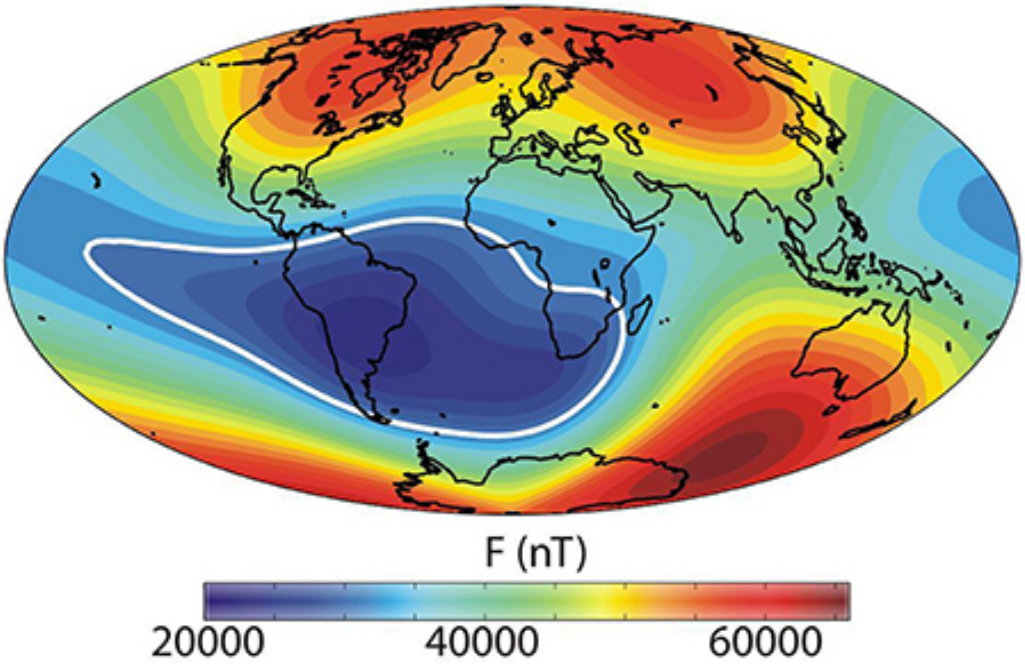

Figure 3.35: Earth map showing the intensity of the geomagnetic field [46].

There have been several empirical models developed after the discovery of the Van Allen belts, a little over 60 years ago, in order to try to estimate the flux of charged particles around the Earth as a function of various parameters, such as solar activity for example. The models that are used in general by the scientific comunity to simulate the orbital charged particles scenario are called AP8/AE8, respectively for protons and electrons. They have been developed by NASA, using data acquired by several satellites between the sixties and the seventies. They are available on ESA's SPace ENVironment Information System (SPENVIS). The problem with these models is that they start to be very old and they tend to underestimate the actual flux of charged particles. The former problem is quite relevant

since these models are simple averages of the data taken in the two situations of maximum and minimum solar activity, that does not take into account changes in the last 40 years [47][48].
To face all the limitations of the AP8/AE8 models, several models have been created, but usually they are limited to a specific situation, contrary to the NASA models that covers the entire inner magnetosphere and a very wide energy range. In an effort to try and follow up on the models created by NASA, the IRENE (International Radiation Environment Near Earth) AE9/AP9 models were proposed by the National Reconnaissance Office (NRO) and the Air Force Research Laboratory (AFRL) [47]. It is based on the data acquired by 33 satellites from 1976 to 2011, so compared to the AP8/AE8 models the data used are definitely more recent. Moreover, since the fluxes are calculated using Monte Carlo simulations, it provides errorbars due to the uncertainties on the data and space weather changes, contrary to the AP8/AE8 models. However, this model too is not perfect, and usually overestimates the flux of charged particles [48].

The objective of this last study about the GAGG:Ce crystal afterglow, is to establish whether or not it might be a problem for the electronics installed on board. In particular, the preamplifiers, described in chapter 3, that are used to amplify the signal measured by the SDDs, have been designed to operate with a leakage current that can go up to $\sim$ 500 pA. To be safer, it is better to fix a maximum limit at 100 pA. As it was explained at the start, the afterglow current generated by the decay of the metastable states is very low, so it is not expected to trigger the detection system onboard the nanosatellites. From the point of view of the front-end electronics the current generated in the SDD by the crystal afterglow is equivalent to an additional component of leakage current, so it is important to verify that it does not reach the above mentioned limit.

Even if the initial fleet of nanosatellites will fly on an equatorial orbit, which is a more favorable orbit since it nearly avoids the SAA, the objective of this analysis is to present a worst case scenario, that could be useful also for the following nanosatellites. This means that instead of an equatorial orbit, an inclination of 10° is chosen for the orbit. The altitude is 550 km, which is the actual altitude for the HERMES Pathfinder nanosatellites. Another parameter intentionally set for a worst case scenario is the SDD efficiency: in general it is around 80%, here it is considered as perfect, i.e. 100%. Same for the transport of the light to the SDD, the worst case scenario supposes that all the residual light generated inside one crystal reaches the two SDD cells optically coupled to it.
Finally, since the AP9/AE9 models tend to overestimate the flux of protons and electrons that can be encountered, the choice of the program to use to recreate the space environment falls on them. In Figure 3.36 it is possible to see the estimate

of the proton and electrons fluxes for the chosen orbit over an entire day, while Figure 3.37 illustrates the integral flux maps from which the data of the former image are calculated. The fluxes in Figure 3.36 are normalized at 70 MeV because this is more or less the maximum kinetic energy that a charged particle can have and still be stopped inside a GAGG:Ce crystal with the nominal dimensions for the HERMES Pathfinder nanosatellites. Consequently, what is done for fluxes of particles at energy E less than 70 MeV, is to divide the flux by 70/E, while for fluxes of particles with energy higher then 70 MeV they are considered as if they released an energy equal to 70 MeV inside the crystal. The latter approximation is not actually totally correct: these charged particles are expected to leave less than 70 MeV, since the Bragg peak, where the majority of the energy is lost, is not contained inside the crystal. To simplify the calculations and remaining in a worst case scenario, these particles are still accounted to release 70 MeV inside the scintillator.

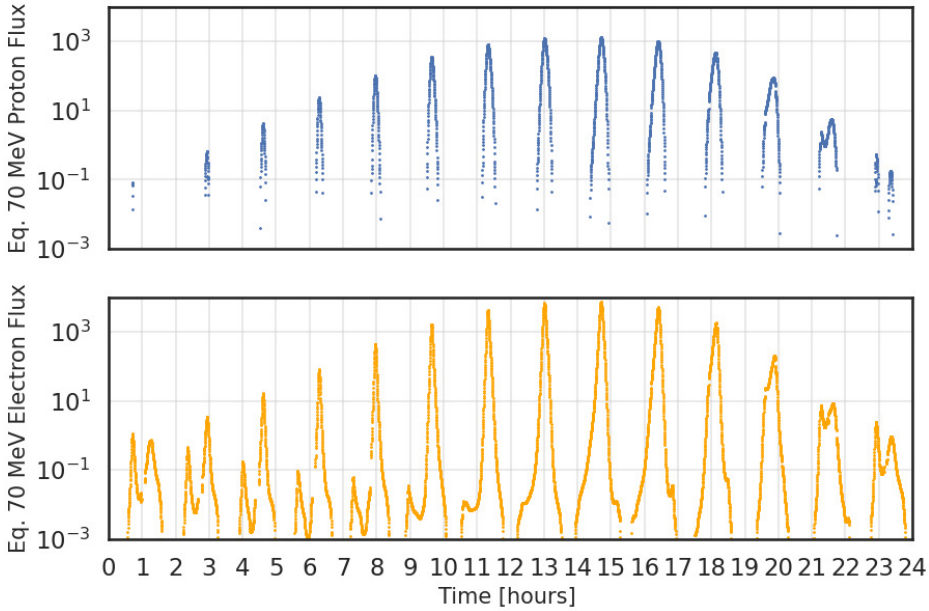

Figure 3.36: Two plots showing 70 MeV equivalent protons and electrons flux over a day, which contains fourteen orbital revolutions around the Earth. Since one orbital revolution lasts a little more than 1.5 hours, after one day the situation goes back to the starting point. Then, these two plots cover all the scenarios.

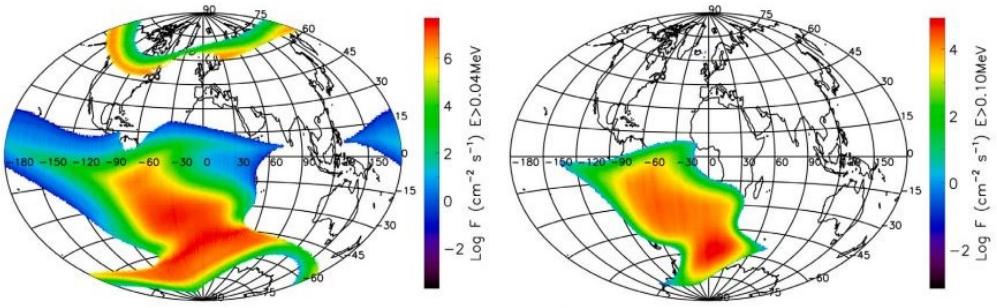

(a) Trapped electrons with kinetic energy exceeding 0.04 MeV. (b) Trapped protons with kinetic energy exceeding 0.1 MeV.

Figure 3.37: Two world maps showing the integral flux. As expected from Figure 3.35, almost all particle flux is concentrated on the SAA [38].

All the calculation are done at a temperature of 20 °C, in order to compare with the work done in [38]. However, due to the longer lifetime of the traps, it is important to explore the effects of the afterglow on a timescale longer than seven days. The best choice is one month which corresponds to the longest metastable state lifetime found here.
Figure 3.38 shows the leakage current accumulated over one month of orbital revolution around the Earth. Since the nanosatellites will be switched off during the crossing of the SAA, the corresponding data are not reported here, as well as for the minute folowing the exit from the SAA, that correspond to the switch on of the nanosatellite, and is also the afterglow part that is described with the largest uncertainty by the fit done in the previous sections.
What can be seen is that the results are at least one order of magnitude larger than what was found previously. This is mainly because the metastable states with longer lifetimes could not be taken into account in the previous study, since it was impossible to find them with the short time of observation of the afterglow available at that time. Since these metastable states last so long before decaying, they accumulate over several orbits. Following the initial growth in the leakage current, due to the detector entering the space environment, the current tends to stabilize after some time, peaking above 1 pA. However it can be seen that the minimum value keeps growing over the month long simulation, initially being less than 0.1 picoampere, and then reaching a few tenths of a picoampere. This minimum correspond to the current of the longest traps, and it is growing for the reason written above, that is the longer traps are occupied faster than they decay. The final result is that the minimum leakage current is more than one order of magnitude higher than in the work shown in [38]. Instead the maximum seems to remain constant. Even with this increase in the leakage current, the situation is still good for the HERMES Pathfinder nanosatellites, especially considering that this is a worst case scenario.

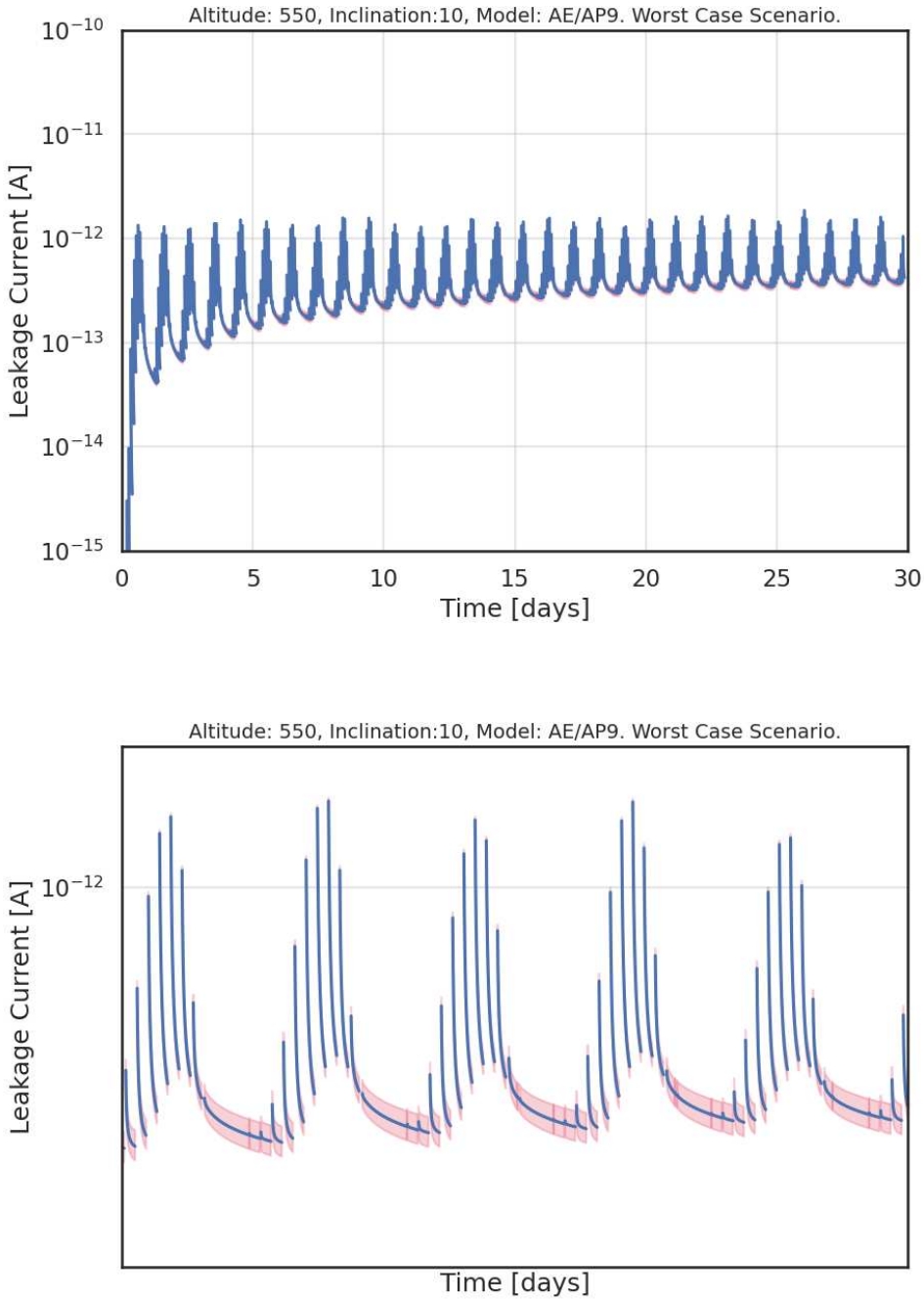

Figure 3.38: Plots of the leakage current generate by the afterglow. On the top image, the entire month is shown, while on the bottom image only a part of it is presented, to show the effect of the single transition over the SAA. The region filled in red represent a ± 1 σ variation on the parameters used.

The only parameter that is not set to the actual scenario that the payload will experience is the temperature. The HERMES Pathfinder detector is expected to operate at a temperature of 5 °C. It has already been pointed out that the traps lifetime dependence on the temperature is not described perfectly by the exponential relation used in this study, and is expected to work only for small differences of temperature from the reference one. To establish with more precision this temperature dependence, more specific measurements should be done. So the estimate reported below is not expected to provide necessarily the real situation (since there is a difference of 15 °C), but just an idea of what the scenario could be at that temperature.
As it can be seen in Figure 3.39, the current generated by the afterglow has higher maximum values but also lower minimum value because the lifetime of the metastable states increased with lower temperatures, so the majority of those traps still have to decay. However, the minimum current is not expected to grow much higher than the level already reached at the end of the month. On the other hand, the maximum is still contained within a few picoamperes, providing no risks for the nanosatellite electronics. However, again, this estimate should be taken with due caution.

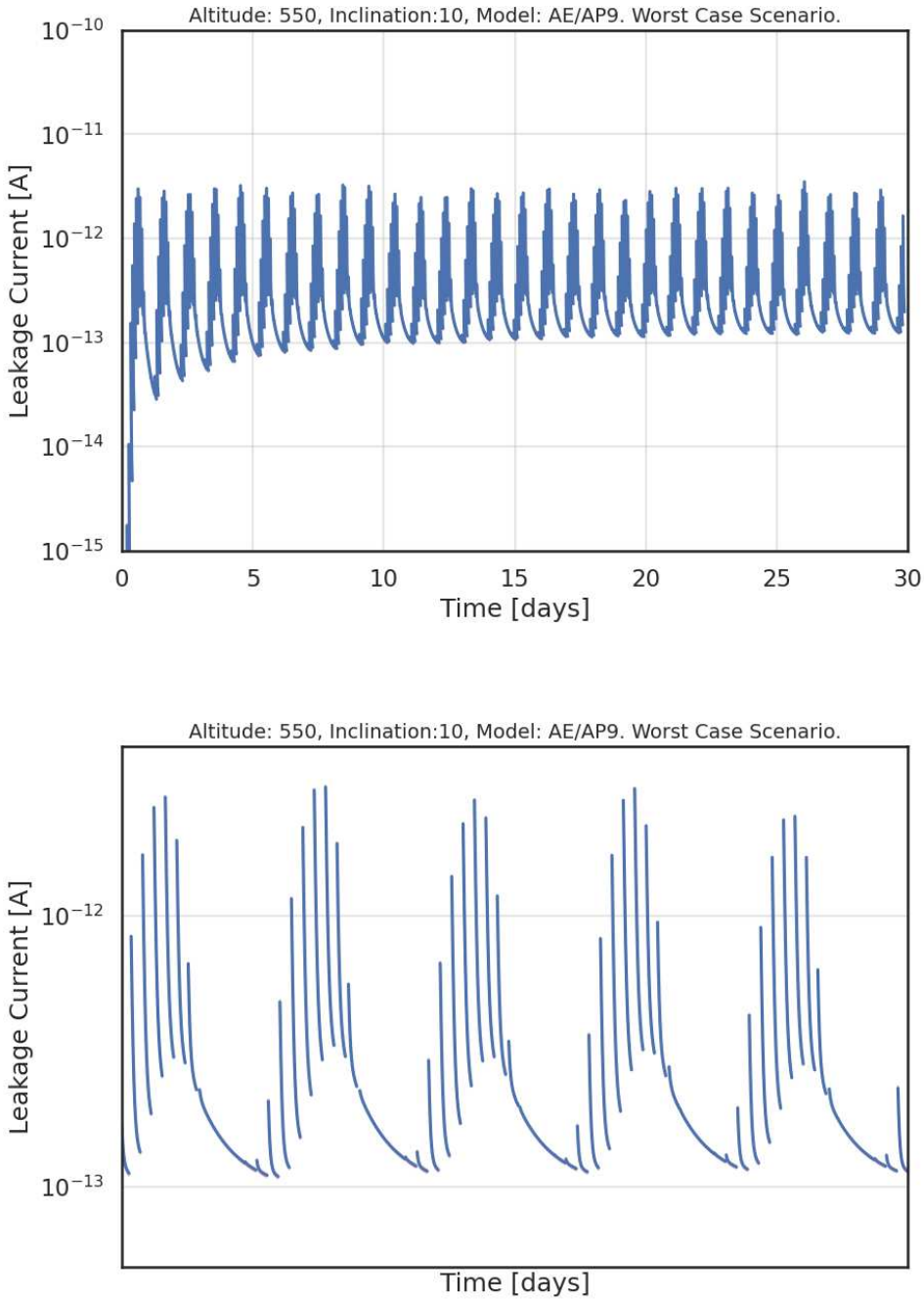

Figure 3.39: Plots of the leakage current generate by the afterglow at 5 °C. On the top image, the entire month is shown, while on the bottom image only a part of it is presented, to show the effect of the single transition in the SAA.

3.2 Qualification and calibration of the HERMES TP/SP nanosatellites

The author contribution provided through this work concerned the Proto-Flight Model (PFM), the Flight Model 1 (FM1) and the Flight Model 3 (FM3). While the FM1 was delivered to the Australian team SpIRIT [30], to be integrated in their 6U CubeSat, the other two, together with FM2, FM4, FM5 and FM6 (the last two are still being integrated as of January 2023), compose the first fleet of HERMES Pathfinder nanosatellites.

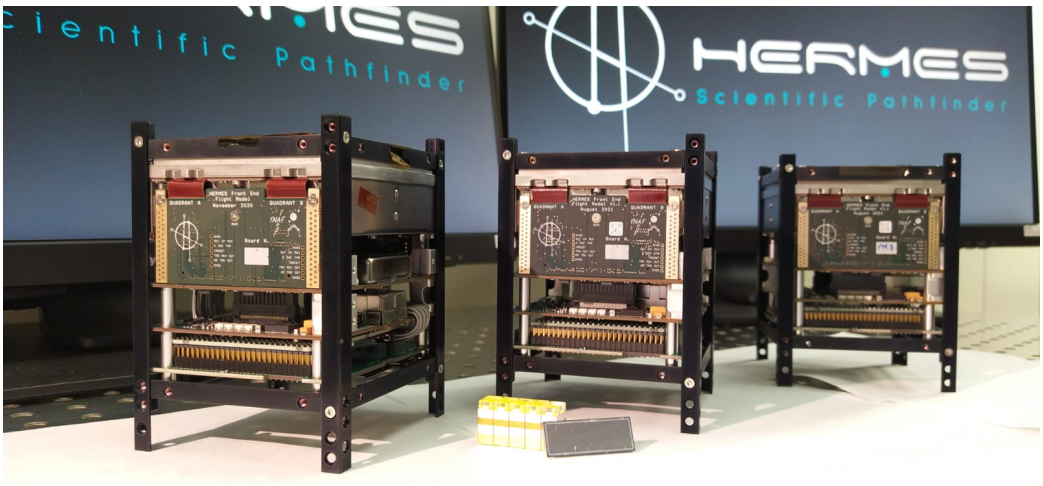

Figure 3.40: The PFM, FM2 and FM3 detector payloads, each one having dimensions 10×10×10 cm^3.

Through all the steps of the detector assembling it is important to verify that all the components are working properly, as long as it is still possible to make adjustments. For example, if one of the LYRA-FE chips is not working properly during the early stages of testing, it is possible to switch to the second circuit (described in section 2.2.1.3) on the same silicon die, or even to replace the ASIC chip. Once the integration of all the components is concluded, a new set of test must be done to qualify the performance of the detectors. This step is crucial to compare the performance before and after the environmental tests, but also to have a priori knowledge of the behaviour of each detector for when they will be in orbit.

The first set of tests, checking the functionality of the front-end electronics and the detectors, have been held in Trento, at the Fondazione Bruno Kessler (FBK) facility, where the assembling of the detector is done. The performance test instead are carried out in Rome, at the INAF/IAPS research center.

3.2.1 Functionality test

The operations described in this section were done by the author for the PFM, the FM1 and FM3. They took place in a period of time going from August 2021 to October 2022.

Since the PSU was not yet integrated for these functionality checks, it was necessary to make use of external power supplies. In particular, three bias voltages were required: one at 2.0 V for the LYRA-FE and two lines at 3.3 V to power the LYRA-BE, respectively for the analogic (3.3A) and the digital (3.3D) part. It is important to verify that, after switching on each generator, the absorption current stays within the range of nominal values that are 1-3 mA for the 2.0 V and 7-9 mA for the 3.3A and <1 mA for the 3.3D.
The test equipment was composed also of a pulser, a digitizer and an oscilloscope (shown in Figure 3.41). The same test equipment was used for the following functional tests, after integrating the SDDs and GAGG:Ce crystals, while for the other campaigns on FM1 and FM3 a new oscilloscope (RIGOL MSO5104), which includes also the functions of pulser and digitizer, was employed.

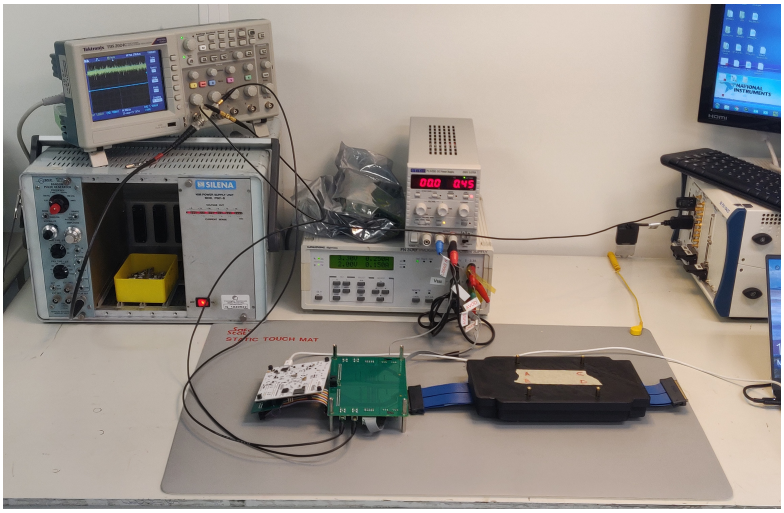

Figure 3.41: Test equipment used for the calibrations performed on the PFM during the first campaign in August 2021.

The initial stage of the functionality tests consists in verifying all the 120 LYRA-FE ASICs, that are placed on the FEE board, and the 4 LYRA-BE ASICs, without any SDD bonded.

After checking that the absorption values were within the limits, the electronics of one quadrant at a time was tested by means of the pulser signal. The input signal

generated by the pulser is directly sent to the LYRA-FE where it is processed as shown in Figure 2.8. The modified (output) signal is then sent from the LYRA-BE to the digitizer. The evaluation of the front-end electronics was done exploiting two different modalities: shaper and stretcher. The first one is used to check the full shape of the signal detected by every channel individually, the second one instead shows the peak value of the signal observed by all the requested channels simultaneously. The stretcher mode employs a peak-and-hold system: at a given discriminator threshold, when an input signal exceeds this limit the peak-and-hold is activated, and once the input signal reaches its maximum and starts to decrease, the output signal instead maintain (or "stretches") the peak value, until it receives a reset command.

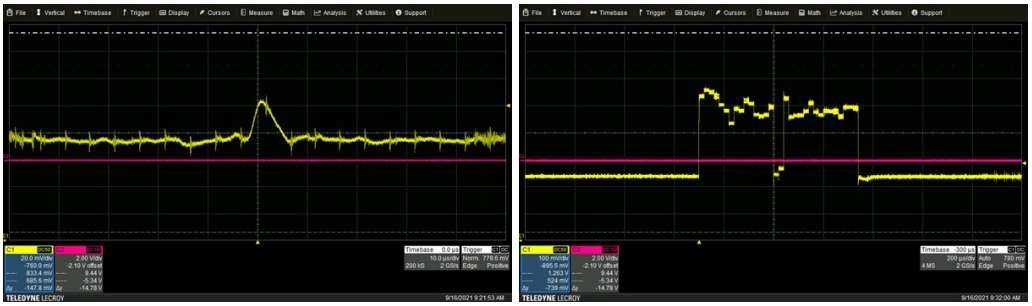

Figure 3.42: Examples of signals observed in shaper mode, on a single channel (left), and in stretcher mode, cycling on all 32 channels (right, yellow line in both cases).

Setting the system in stretcher mode (which is the mode used for acquisition in orbit) an initial inspection was made on all channels from their response to a signal generated from the pulser, so providing an immediate view of the noisy channels. Then, turning to the shaper mode, every channel was analyzed individually, finding the best working configuration for each channel. Then a data acquisition was launched until 2000 events have been registered in order to have enough statistics for the subsequent analysis. This operation was repeated three more times, attenuating the input signal by a factor 2, 5 and 10. In this way there are four different signals measured to estimate the gain and offset parameters of the channels. Turning back to the stretcher mode, the same data acquisition was done on all channels simultaneously, by cycling the multiplexer, collecting 4000 events each time. However, with an attenuation factor of 10 no channel was able to reach the trigger threshold. Consequently the analysis of the strecther was done with only three signals of different amplitude. Thanks to these early controls it was possible to individuate that one channel was not working and even causing problems to the rest of the quadrant, leading to its substitution with a new FE chip.

To obtain the gain and offset values for every channel and identify any anomalies, a calibration was done from the data acquired for both operative modes. The calibration was carried out by a python code. The program locates the peak positions in the distribution of the amplitude ot the output signals measured by the channel, and then proceeds to compare the original amplitude of each type of input signal generated with the position of the corresponding peak in the distribution. The linear fits, obtained for the shaper and the stretcher points of each channel, provide the offset (intersection with the x-axis) and the gain (1/slope of the fit) of the associated ASIC (see Figure 3.43 for more details). In formula:

$$y[ADC] = x[ADC] \times \text{Gain}[ADC/ADC] + \text{Offset}[ADC] \tag{3.9}$$

where y is the amplitude of the output signal and x is the amplitude of the input signal.

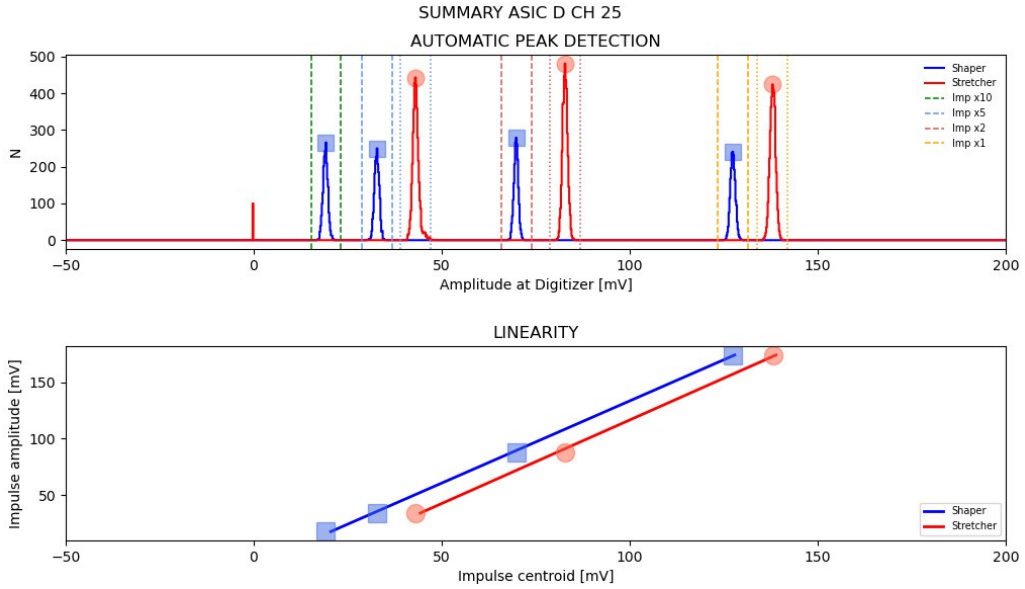

Figure 3.43: Example of the calibration process done on the FEE before the SDD bonding. The top image shows the distribution of the signals acquired by the channel (8000 events in shaper mode and 12000 in stretcher mode) and the detection of the peaks. The lower image presents the linear fit between the amplitude of the input signal and the one of the output signal.

Since these were mainly functionality tests, a careful study of the detector performance was not performed at this point, especially considering that the noise aspect will improve once the detector payload is fully assembled. The important

information acquired were that, after the substitution of the critical chip, all the ASICs were operative, and eventually some noisy channels were identified.[1]

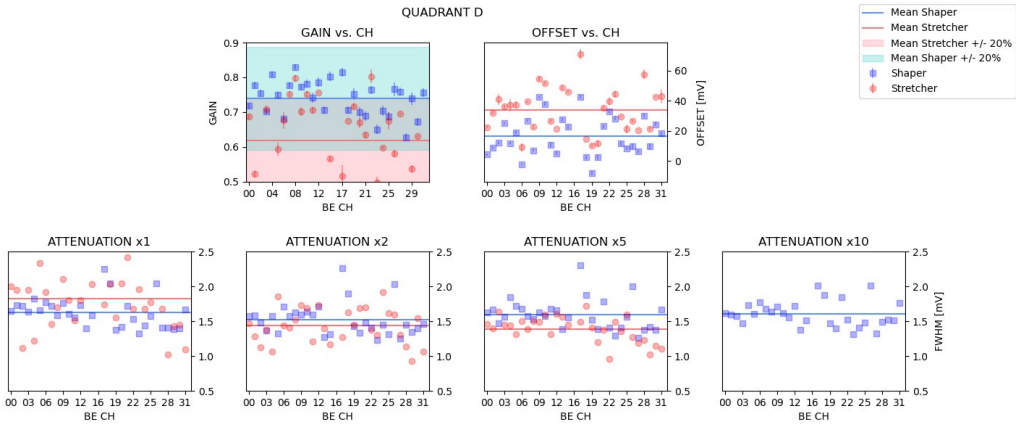

Figure 3.44: Results obtained after the calibration of the quadrant D of the PFM. The upper images show the gain (left) and the offset (right) for all the ASICs of the quadrant. The gain of all the channels is expected to be contained within ± 20% of the mean value. The lower images show the FWHM (in ADC units) for each of the peaks. The x-axis refers to the identification number of each channel.

The next step consists in verifying again the LYRA-FE ASICs after placing the 12 SDD arrays (Figure 2.6) on the FEE board and bonding all the circuits to the pads on the n-side of the cells. The functional verification is done by means of a pulser signal initially and then using radioactive sources, emitting in the X energy band, in order to test also the SDDs.

Once the SDDs are integrated to the detector, they require a dedicated bias to allow reaching the nominal full bulk depletion voltage (−123 V, the nominal absorption is 14 µA) allowing the proper collection of the signal charge.

Starting with the signal pulser, it was not necessary to reproduce all the data acquisition done in the previous step, unless there were channels that were behaving strangely, to understand the causes. At this stage it is still possible to intervene and improve the malfunctioning channels, or at least try to. Subsequently the data

[1] For the sake of completeness, since it was not directly involved in this doctoral work, there was another aspect that needed to be investigated: in some cases the two fits had different slopes, meaning the two modes had different gain for the same channel (as it can be seen in Figure 3.44). It was later discovered that this is related to the ASIC itself: for some channels the gain is dependent on the threshold used. This was fixed applying an hardware patch for the ASICs already in use and developing a new version of the LYRA ASIC, which is being tested on the FM4.

acquisition was performed using the radioactive sources, again in stretcher mode and switching off the channels that were too noisy, due either to a high leakage current or because they are too sensitive to environmental electromagnetic interferences. The choice of the sources depended on the availability at different times when the tests were run at FBK. The first time for the PFM the X-sources were Cadmium-109 (^{109}Cd) and Barium-133 (^{133}Ba), while for the following campaigns ^{109}Cd was used again, with Iron-55 (^{55}Fe) instead of ^{133}Ba. It is necessary to use multiple sources in order to have enough emission lines for the calibration. For example, considering the second case of available sources, the detectors should observe three emission lines: one from the ^{55}Fe at 5.9 keV, and two from the ^{109}Cd at 22.1 keV and 24.9 keV. It was then discovered that there was a fourth line at 8.05 keV, due to the fluorescence of the copper used to isolate the system, that could be also exploited for the calibration. During the data acquisition, the sources were placed on the protections used to shield the detectors from the ambient light, and were moved around the quadrant to ensure that all the channels were equaly irradiated.

For this real calibration procedure made using radioactive sources the procedure had to be sligthly modified. After finding the position (expressed in units of the analog-to-digital converter, ADC) of the peaks corresponding to the output signals, the equation to describe the processing of the input signal is similar to equation 3.9, but in this case the input signal is represented by the electrons released inside the SDD silicon bulk, following the absorption of a X-ray (one electron-hole pair created every 3.65 eV of deposited energy [50]). Consequently, the units of the quantities are different:

$$y[ADC] = x[e^-] \times \text{Gain}[ADC/e^-] + \text{Offset}[ADC] \tag{3.10}$$

It is then possible to reconstruct the spectrum expressing the output signal amplitudes in keV. From the gain and offset values obtained, the amplitude measured is converted from ADC to electrons, as follows:

$$A[e^-] = \frac{A[ADC] - \text{Offset}[ADC]}{\text{Gain}[ADC/e^-]} \tag{3.11}$$

Using the relation $1e^- = 3.65\text{eV} = 3.65 \cdot 10^{-3}\text{keV}$, the amplitude can be converted once more, this time in keV:

$$A[\text{keV}] = 3.65 \cdot 10^{-3}[\text{keV}/e^-]A[e^-] \tag{3.12}$$

This is called the X-mode calibration, since it correspond to the X-mode observation of the nanosatellite (described in Section 2.2).

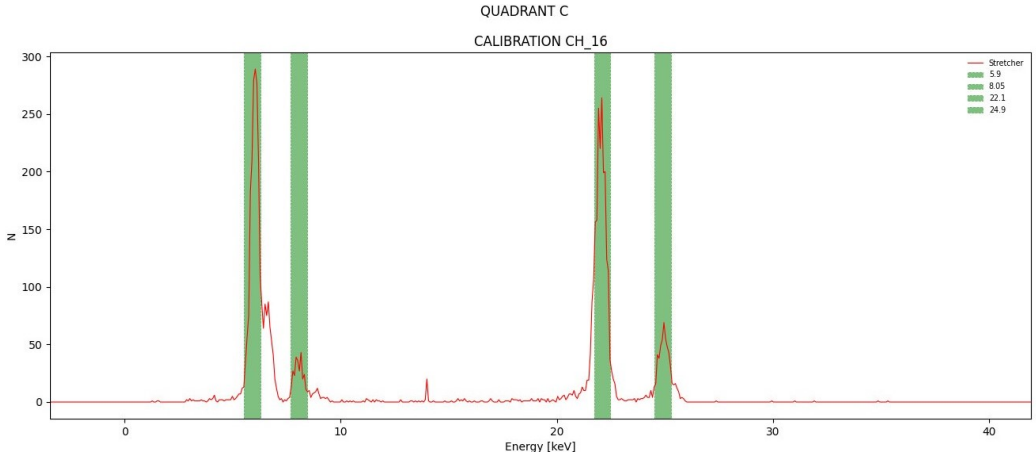

Figure 3.45: Example of calibrated X-spectrum for a channel on the FM1. The green area are centered on the energies of the emission lines used for the calibration which are 5.9 keV, 8.05 keV, 22.1 keV and 24.9 keV.

For all the flight models studied there were a few channels that during this procedure resulted too noisy, mainly because of the too high room temperature (23 °C), and had to be turned off. The in orbit operational temperature is foresen to be 5 °C. This corresponds to a lower noise, making those channels operational again. In some cases the reason could be related to difficulties during the bonding between SDD and FEE making it more complicated to recover those channels.

The last step of the detector assembling that takes place in Trento is the integration of the crystal box. The 60 GAGG:Ce crystals, neatly arranged in their box after being cleaned of all possible contaminations, are placed in optical contact with the SDDs, separated by the silicon pads, that are delicately compressed (described in chapter 2). the whole assembly is done by a dedicated specialist.

Once the crystals box integration was achieved, a quick check was executed using the pulser to verify that the process did not result in a damage to any channel. The final data acquisition was then directly performed to proceed with the S-mode calibration. In order for the radiation to cross the SDD cells and reach the crystal, the source used for this test was the Cesium-137 (^{137}Cs), which has an emission line at 661.7 keV. The S-mode calibration has as its primary goal to verify the effective light output for each channel, which is defined as the number of electrons generated inside the SDD per unit of energy absorbed in the crystal. It is different from the intrinsic light yield of the crystal (expressed in photons per keV) since there are other factors that need to be considered, like the SDD quantum efficiency (the fraction of scintillation photons able to produce one electron of charge in the

active silicon bulk; on average, one optical photon that reaches the active bulk produces an electron), the optical contact efficiency (the fraction of scintillation photons able to reach the SDD surface window, which may change from one channel to another). The effective light output is known to be a non-proportional quantity, i.e., its value depends also on the energy (consequently, the effective light output obtained here is referenced to the 661.7 keV line) [51]. Finally, it also depends on the temperature, with an expected ∼20% increase by going from room temperature to −20 °C [37].

From the spectrum expressed in units of the ADC, it is straightforward to obtain the spectrum in units of e^- using the gain and offset values obtained with the X radioactive sources. Knowing that the peak observed must be the ^{137}Cs emission line at 661.7 keV, to obtain the effective light output, $LY[e^-/\text{keV}]$, for every channel the peak is fitted and then the central amplitude is divided by the energy of the emission line.

$$LY[e^-/\text{keV}] = \frac{A[e^-]}{A[\text{keV}]} \tag{3.13}$$

where $A[\text{keV}]$ is equal to 661.7 keV. Once the light output has been derived for both channels optically coupled to the same crystal, it is possible to reconstruct the event amplitude, in keV, that led to the signal, in e^-, read out by the channels with the following equation:

$$A_{\text{tot}}[\text{keV}] = \frac{A_a[e^-] + A_b[e^-]}{LY_a[e^-/\text{keV}] + LY_b[e^-/\text{keV}]} \tag{3.14}$$

In the spectra obtained with this calibration (like in Figure 3.51) there is a continuum signal at lower energies. This signal is the Compton continuum, it is the consequence of the photons that escaped the crystal after scattering several times, and consequently have a lower energy than expected.

During the first tests done on the PFM, it was noticed that the effective light output was lower than expected (the estimated value is 14-15 e^-/keV). The mean value found during these tests was about 11.4 e^-/keV. Keeping in mind that lowering the temperature this value increases, it was however considered that this could be caused by a non-optimal optical coupling. Consequently the silicon pads have been more compressed in the following integrations. That actually led to an increase in light output. The PFM mean effective light output improved to 12.6 e^-/keV, while for the FM1 the mean value is 12.1 e^-/keV and for the FM3 it is 13.1 e^-/keV. At the operating temperature (∼ 5 °C for HERMES Pathfinder and ∼ −15 °C for SpIRIT) these values should reach the expected value.

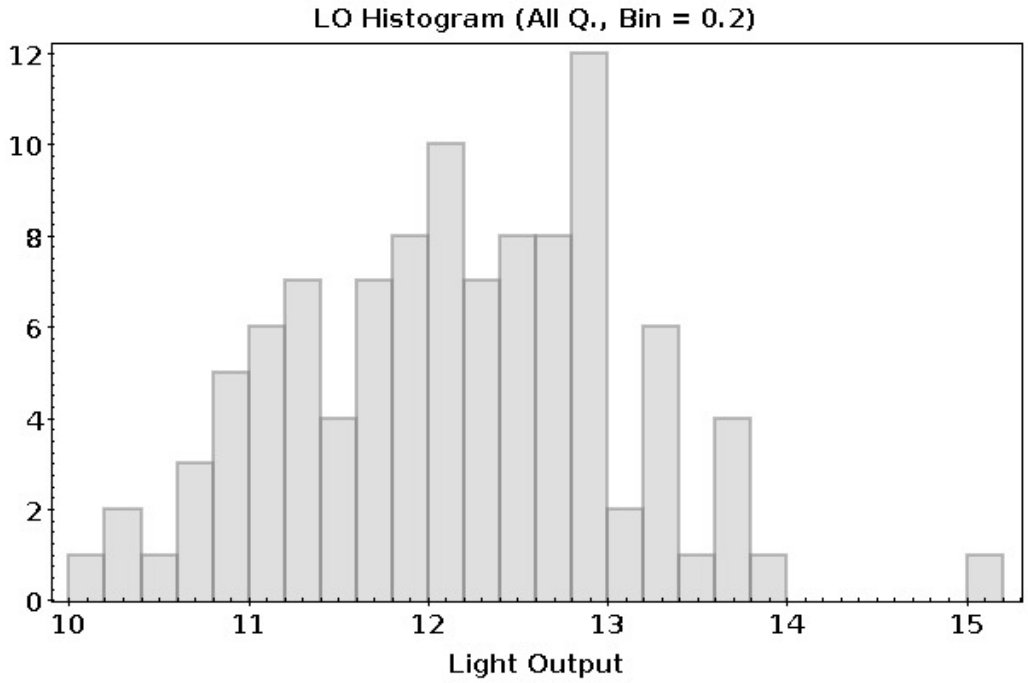

Figure 3.46: Effective light output distribution for all the active channels in FM3.

Concerning the active channels situation, usually there were not many differences between before the crystal box integration and after. Taking the FM3 case as an example, before assembling the crystal box to the detector, 109 of the 120 (90.8%) channels were working properly, 4 (3.4%) channels were working marginally due to noise and 7 (5.8%) channels had to be switched off, either due to too much noise/retrigger (4 of them) or to a lack of responsiveness (3). With the box integrated, still 109 (90.8%) channels were working properly, 5 (4.2%) channels were affected by acceptable noise and 6 (5%) channels were switched off, either due to retrigger (2) or to a lack of responsiveness (4). This means that on one side one channel was recovered in part, but on the other side one other channel was not working anymore. Similar behaviours were manifested by the other flight models. This last step concluded the functional tests.

3.2.2 Performance calibration

After finishing with the step by step functionality tests, the detector payload is packed, with all the possible precautions, and prepared for the journey to Rome. At the INAF/IAPS laboratories all the activities on the detector payload are performed in a class 10000 clean room. The detector assembly is integrated with the BEE board, the PDHU and the PSU. It is then placed in a climatic chamber, which has

been equipped with a 3D printed source holder, where are placed the radioactive sources, and a cover to prevent them from moving. The source holder is mounted on a movable arm inside the climatic chamber. In this way the sources are usually placed at 18–20 cm from the detector top side, allowing for an almost uniform coverage of the detector plane (maximum off-axis angle is ∼15°–20°). The PDHU, inside the box, is connected to an external PC using a custom-made interface. All the test equipment used for these calibrations is represented in Figure 3.47.

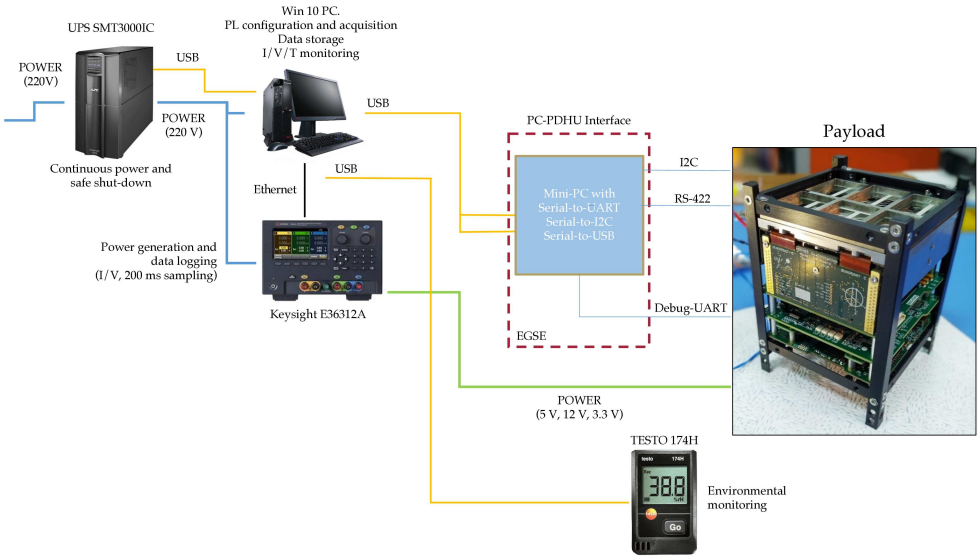

Figure 3.47: Schematic representing the various instruments used for the calibrations in Rome.

The objective of this calibration was again to obtain the gain, offset and effective light output for every channel, with the HERMES Pathfinder payload fully integrated. This means that there was no more space for modifications on the hardware. The only modification possible was on the acquisition configuration of the channels, to find the better one. Similarly to the functional test, the detectors were exposed to radioactive sources to perform the X-mode (^{55}Fe and ^{109}Cd) and S-mode calibration (^{137}Cs), this time using all the sources at the same time. Exploiting the climatic chamber, the calibrations were done at several temperatures, starting from +20 °C and reaching −20 °C, by steps of 10 °C. For each temperature, three different data acquisition were executed, changing the discriminator threshold. Three values were used: 105, 95, 85 (in units of the digital to analog converter, DAC, that generates the reference voltage to power the discriminator). The higher threshold corresponds to about 2 keV in energy units, which is compliant with the requirements of the HERMES Pathfinder nanosatellites, to observe photons down

to 3 keV. However, lowering the threshold, the noise read out increases. With these tests it is possible to individuate the best threshold.[2]

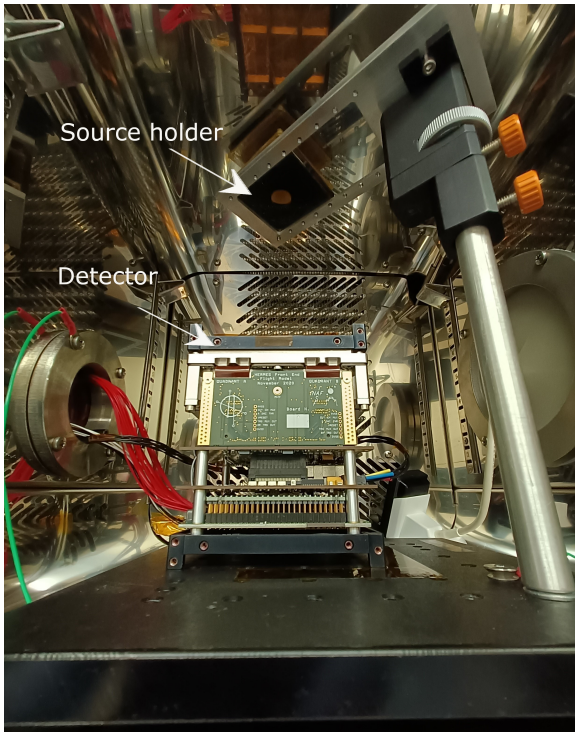

Figure 3.48: HERMES Pathfinder FM1 detector unit placed in the climatic chamber, with the source holder visible above the detectors.

The data acquisition was done directly from the PDHU. Refering to Figure 2.12, while moving from one operational mode to the other, it is always important to verify the absorption values. The nominal ones are (for the three lines of the PSU at 3.3 V, 5.0 V, 12.0 V): 296 mA, 69 mA and 0.066 mA in STANDBY mode, 298 mA, 85 mA and 26 mA in IDLE when the SDDs are powered. Using the housekeepings it is possible to verify if all the currents and voltages inside the payload are correct, and they provide also the temperature measured in different parts of the unit. When everything is set, the OBSERVATION mode is launched for 900 seconds, the time necessary to accumulate at least 10^5 events per radioactive source per channel. Returning to STANDBY mode the data are downloaded to the computer.

[2] Another reason for studying different thresholds is to verify if the gain is finally independent from it after the hardware patch (see footnote 1).

The analysis was conducted using an advanced version of the python script previously described. This new software, called `mescal`, is an automatized pipeline of Python scripts. It requires a list of the sources employed for the calibration and the data file in a format called FITS "Level 0.5". The algorithm mechanism is described in Appendix A.

The analysis reported here concerns the FM1. Unfortunately, during the calibrations a fault occured in quadrant A, generating a short-circuit on the 12 V power line. Because of time limitations and risks related to disassemble the detector, the calibration were carried on with the A quadrant switched off. On the other three quadrants some channels had to be turned off (22 in total).

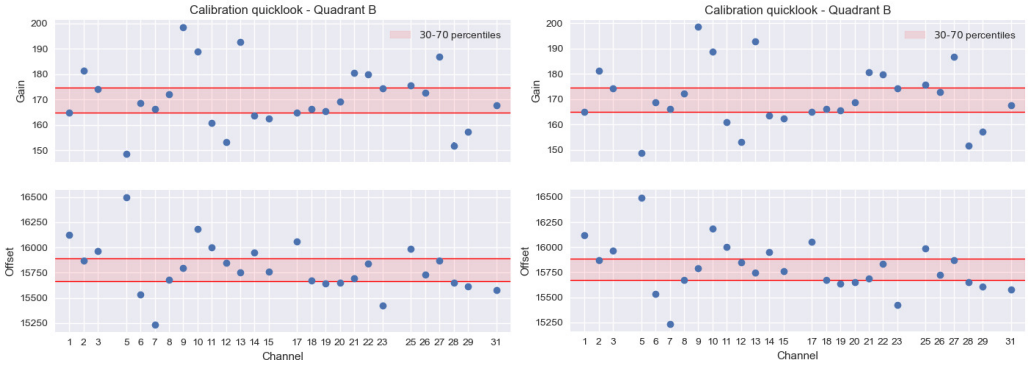

Figure 3.49: Plots showing the gain and offset values obtained for the channels of the quadrant B, at 0 °C, for a threshold of 105 (left) and 95 (right).

One of the first aspect that were verified is the dependence of the gain and offset from the threshold chosen. In Figure 3.49 are reproduced the values of gain and offset obtained for the same quadrant, at the same temperature but with different threshold. The two cases show identical values, confirming that the problem has been fixed. It might happen in other flight models that one or two channels are still slightly dependent on the threshold, but in general the problem was solved.

For the FM1, the baseline calibrations presented here were obtained with the 105 threshold (although the 95 threshold provided good results too). In Figure 3.50 and Figure 3.51 are displayed, respectively, the X-mode calibration and S-mode calibration results, with all the emission lines well defined. In the latter one the emission line at 88 keV of the ^{109}Cd appears, and is correctly placed, meaning the calibration works properly. In the middle there is the Compton continuum described before.

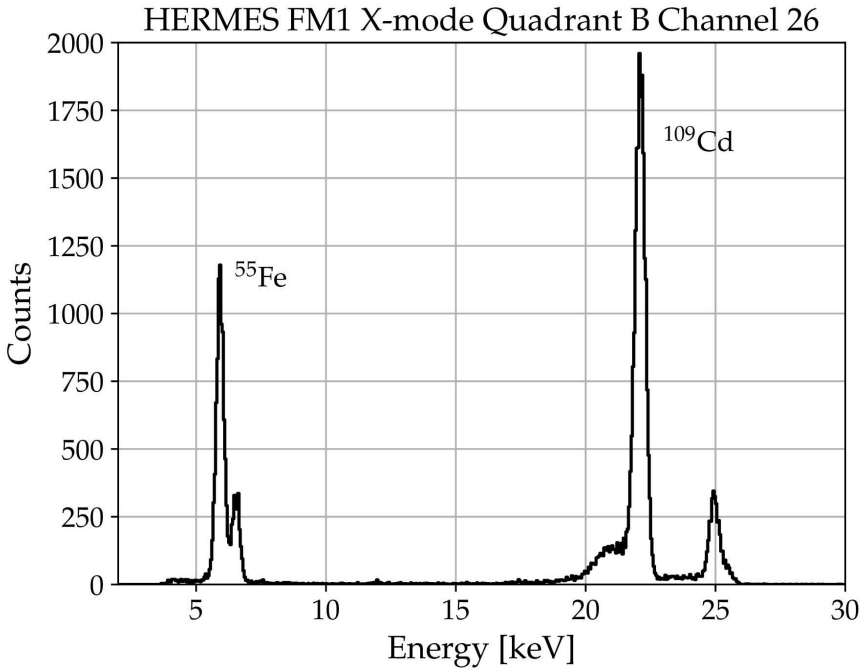

Figure 3.50: X-mode calibrated spectrum of one channel on the FM1 HERMES Pathfinder detector, at a temperature of −20 °C and a threshold of 105.

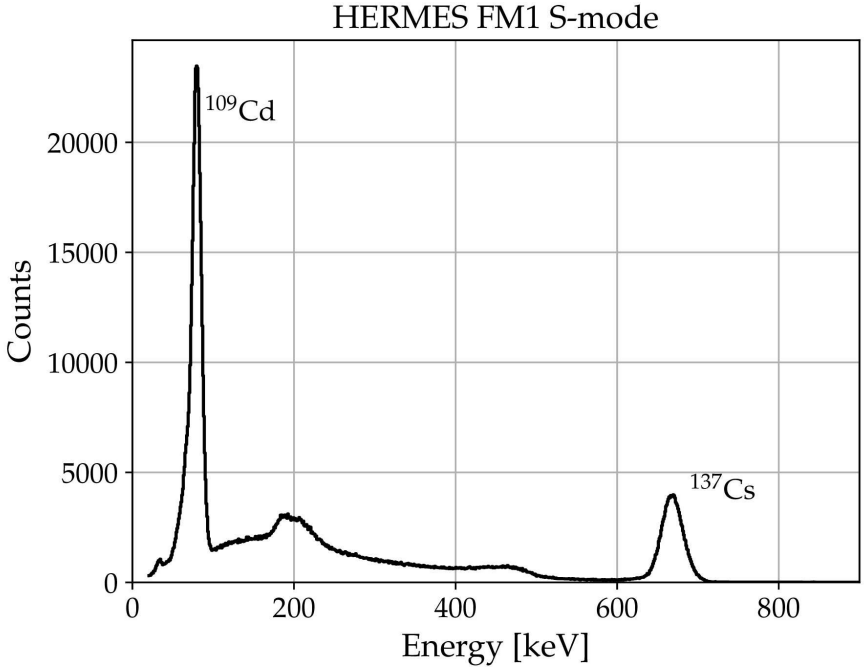

Figure 3.51: Summed S-mode calibrated spectrum of the whole FM1 HERMES Pathfinder detector, at a temperature of −20 °C and a threshold of 105.

The last aspect to be verified is if the effective light output obtained during the S-mode calibration reached the expected value. At -20 °C (which is close to the operative temperature of SpIRIT) the mean effetive light output value is 14.25 e^{-}/keV, which is satisfying for the purpose of the mission.

3.3 Minimum variability of gamma-ray bursts

The principal scientific objective of the HERMES Pathfinder project is the study of gamma-ray bursts. Over the last 60 years many discoveries have been reported and many theories have been developed to understand the GRBs nature, but there are still many unanswered questions.

The objective of this part of the PhD work is to explore the GRBs sources using a tool called microvariability, defined as the shortest variability timescale displayed in the GRB lightcurve. This tool allows to have some insights about the GRB central engine and see if it is possible to identify any relations between the minimum variability of a GRB and the energy bands considered, but also with other characteristic values of the GRBs, in particular related to the energy aspects of the burst, like the peak energy or the isotropic energy. Fast timing, of the order of fractions of μs, is one of the main objectives of HERMES Pathfinder Pathfinder. The study of the fast variability of GRBs should provide important answers on the model describing the central engine of GRBs, on the composition of the jet, but also for fundamental physic studies, like granular structure of spacetime. Consequently, huge efforts were put in improving the payload timing capabilities reaching a time resolution of 300 ns, which is 5-7 times better than any previous in-orbit telescope. [12]. This will allow to identify values of microvariability of the order of microseconds, if present.

3.3.1 What is the Microvariability

The idea of the microvariability first appeared in a paper of Walker et al. (2000) [52]. The minimum variability of a GRB depends on the central engine processes. Looking at the results obtained up to today, the microvariability value is generally expected to be found in the range going from milliseconds to seconds. However, this value could be even shorter, having as only limitation the time resolution of the instrument. Using the Time Triggered Event (TTE) data of GBM, for example, microvariabilities lower than 2μs are not observable.
While a variability of the order of a second can be easily seen with the naked eye from the spectrum of the GRB, it is a much more difficult undertaking to find peaks of the order of milliseconds. Even more, it must be considered possible to find even lower values for the microvariability.
From the litterature, which unfortunately is very limited, the technique that is generally used to extract the microvariability of a GRB is the wavelet analysis, in particular using the Haar discrete wavelet transform [53]. Using a wavelet transform allows to obtain information on the signal variation in both time and frequency contrary to a Fourier transform that is limited by the uncertainty prin-

ciple. There are two types of wavelet transform: continuous and discrete. For the purpose of this work, the discrete wavelet transform is the obvious choice, working with a discrete set of data. A discrete wavelet is a set functions that forms an orthonormal basis, and can be used to explore the time-structure of the GRB spectrum. From the coefficients generated by the transform it is very simple to separate the noise (low value) from the signal (high value) by setting a threshold and preserving only the signal coefficients [54]. The simplest discrete wavelet existing is the Haar wavelet, which consists in an antisymmetric function, setting one bin positive, the following one negative and all the others equal to zero. An example is given supposing to have a scale of $\frac{1}{2}$:

$$\psi(t) = \begin{cases} +1 \text{ if } 0 \leqslant t < \frac{1}{2} \\ -1 \text{ if } \frac{1}{2} \leqslant t < 1 \\ 0 \text{ everywhere else} \end{cases}$$

The discrete wavelet transform works for a set of data $\{X_1, X_2, ..., X_N\}$ of dimension N that must be a power of 2, i.e. $N = 2^q$ ($q > 0$). The Haar transformation returns the same amount N of coefficients, comprising $N - 1$ detail coefficients, obtained from the difference between adjacent bins, for an increasing scale $k = 2^i$, with i in $\{0, 1, 2, ..., q - 1\}$ (shown in equation 3.15), while the last coefficient is the mean value of the set of data.

$$d_{j,k} = \frac{1}{\sqrt{2k}} \left[\sum_{n=0}^{k-1} X_{2jk-n} - \sum_{n=0}^{k-1} X_{2jk-k-n} \right] \tag{3.15}$$

where j is an index that can take the following values $\{1, 2, 3, ..., N/2k\}$.

Except for the common starting point, the methods employed in the articles studied are different between them. This required a deep study of these techniques to understand which one was more accurate. There are three main articles that were found and studied about this topic. The first one has already been cited (hereinafter referred to as paper 1), the second one was written by MacLachlan et al. (2013, paper 2) [55] and the last one is a work of Golkhou and Butler (2014, paper 3) [56]. To this first work of Golkhou and Butler followed a second article in 2015 [57] (paper 4).

In paper 1, starting from the Haar wavelet a new quantity is defined, the activity. It is obtained from the mean value of the square differences of counts between adjacent bins, in formula:

$$A(\tau) =< [C(t) - C(t+\tau)]^2 > \tag{3.16}$$

where A is the activity, C are the counts in each bin and τ is the binning time. A normalized activity is then defined, and consists in dividing the activity of the GRB by the noise activity, with the noise assumed to be Poissonian. Calculating the normalized activity for increasing time binnings, what is observed is that for the lower ones the normalized activity is equal to one, i.e. the noise and the burst have the same activity, while for higher binning times the normalized activity starts to grow. The point where this value exceeds the activity of the noise by more than 3σ represents the microvariability. The analysis is done using 20 bright GRBs observed by BATSE, and in general the microvariability found is very low, of the order of the millisecond for both long and short GRBs, sometimes even below.

In paper 2, the process executed to obtain the microvariability considers the variance of the details coefficients for every scale (which is essentially the same thing as the activity). In order to remove the background contribution, the variance at each scale is also calculated for an interval of time previous to the trigger time of the burst. After the background subtraction, there are two contribution remaining in the original variance, one is the noise and the other one is the burst. Looking at them in a log-scale diagram, where the y-axis shows the base 2 logarithm of the variances and the x-axis the scale, the first one is generally flat, while the second one is growing linearly. The microvariability is given by the intersection between the two components. Working on Fermi GBM bursts, the article found a microvariability ranging between a few milliseconds (for short GRBs) to hundreds of millisecond (for long ones).

In paper 3, the technique follow the same initial idea. The equivalent of the activity, here called structure function, is used to explore the temporal features in the spectrum of the GRBs. Expanding the structure function by the means of a first order Taylor expansion it is found that there is a proportional relation between the square root of the structure function and the timescale τ:

$$\sqrt{SF(\tau)} \propto \tau$$

This is true for the timescales at which the signal varies smoothly, otherwise the Taylor expansion would not be valid anymore. Consequently, when the signal starts to have non-smooth variations the square root of the structure function (from now on called $\sigma_{X,\Delta t}$) no longer grows linearly with the timescale. The last point before exiting the linear regime represents the microvariability of the GRB. There are then three phases that can be identified in the structure function scaleogram: an initial flat phase due to the predominance of the noise, a final flat phase when the

signal variance reaches its maximum and a linear phase in the middle (as shown in Figure 3.52). To make the structure function analysis more robust, the Haar wavelet transform is not applied only once but N times, each time on the same set of data (of dimension N) circularly shifted by one position. The final value of $\sigma_{X,\Delta t}$ is obtained by averaging the N transforms results, shifted back in their original position. This is called a non-decimated Haar wavelet tranform, which is translation invariant and solves some artifacts that are usually connected to this type of wavelet transform.

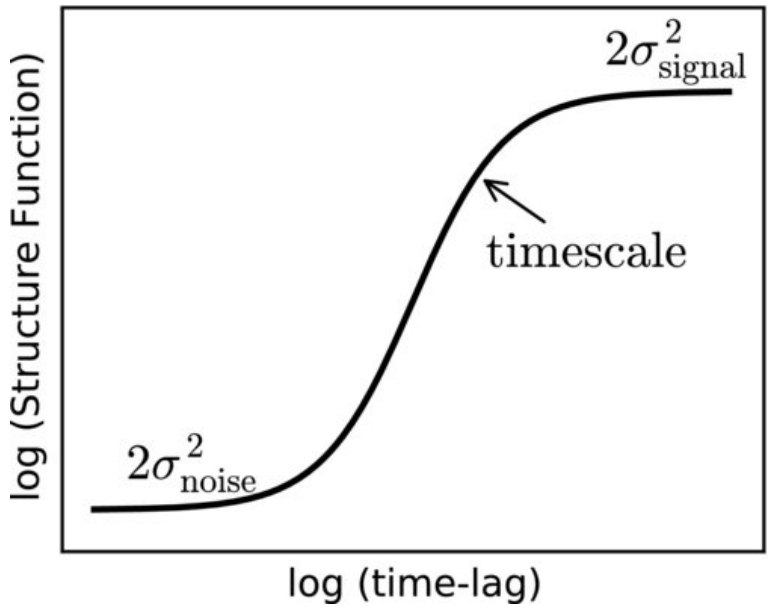

Figure 3.52: Representation of an ideal structure function scaleogram. [56]

The study conducted in paper 3 uses the GRBs detected by Swift, while the second work of the same authors is focused on Fermi GBM observations. In general it is found that long GRBs have a median timescale for the microvariability lower than a second (but in some cases reaches even tens of seconds), while for short GRB it is of the order of tens of milliseconds.

The results obtained in the three articles are quite different between them. In particular, paper 1 finds the lowest microvariability, while paper 3 has the highest values. However this is a consequence of the criterion selected to identify the microvariability: looking at Figure 3.52, the paper 1 and 2 methods locate the microvariability timescale at the start of the linear phase, while in paper 3 the microvariability is found at the end of the same phase. The choice made in paper 3 seems more justified in the light of what has been said in the previous paragraphs. Moreover, as shown in paper 3, the value found for the microvariability corresponds

to the fluctuations observed in the GRB spectrum, which is not demonstrated for the other two techniques.

In order to choose which method is more efficient to find the microvariability there is one requirement that the selected method must comply with: its independence from the noise measured by the instrument. Since the noise changes from one satellite to the other, depending on the collecting area, a method that is dependent on the noise would give results that are influenced by the satellite itself. From this point of view, the first two article do not satisfy the requisite, since their criterion of selection is based on the noise level. The only criterion that depends only from the burst characteristics is the one of paper 3. In conclusion the technique developed for this work was first proposed in paper 3.

There are also other techniques that do not involve wavelets to obtain the microvariability, in some cases this is also due to a different definition of microvariability. An interesting approach can be found in Camisasca et al. (2023) [58]. In this case, the microvariability is defined as the shortest full width half maximum between all the statistically relevant peaks displayed in the GRB lightcurve. The results observed are slightly higher than those observed in paper 3 considering the same sample of GRBs. This is due to the different techniques to identify the significant peaks in the lightcurve. Also, the GRBs are not classified based on their duration but following the criteria presented in [28].

3.3.2 Two different approaches

One of the largest catalog of GRBs available is the Fermi GBM one. Since its launch in 2008, GBM was able to observe more than 3000 bursts. To achieve a good statistic and extract some information from the microvariability it is crucial to apply the technique developed on a very large set of GRBs. This is even more important in order to analyze as many GRBs with measured redshift as possible.

The first step consists in recovering the Time Triggered Event (TTE) data files of the bursts. The TTE data contains the temporally unbinned data, i.e. it provides the time at which every photon is detected. In this way it is possible to have an insight on the spectrum variations at the smallest timescales. The GBM data tools proved to be very helpful for this task. Through a python library called "gbm.finder" it is possible to obtain the full burst catalog, with all the information usually required, like the T_{90}, the corresponding start time, the fluence, ... Using the same library it is also possible to directly connect to the archive where the TTE files are stocked and download them. For each event there is one file for each detector on board of Fermi GBM (this means 12 files for the NaI detectors and 2

for the BGO ones, as described in section 1.4). From the catalog it is possible to obtain a list of the triggered detectors for each GRB. To proceed with the analysis, only the files of the triggered detectors are kept, and merged in a unique file. Also, for this work there is no interest in the BGO detectors, which means that the two related files are always discarded.

Once the merged TTE file is ready, it is necessary to proceed with a background removal. For this operation there is another library called "gbm.background" that can provide good results. It first requires to bin the TTE data. Then, given two time intervals, one going from 20 to 5 seconds before the burst and one from 75 to 150 seconds after the burst, it returns the best fit of the background. For the analysis conducted here, a linear fit suits perfectly the requirement. This fit is then subtracted to the burst itself, selected between the starting time (obtained from the catalog) and the final time (adding the T_{90} to the starting time) and binned at 0.2 ms. To avoid losing part of the burst, the initial and final time are respectively subtracted and added the T_{90} error. An example is shown in Figure 3.53.

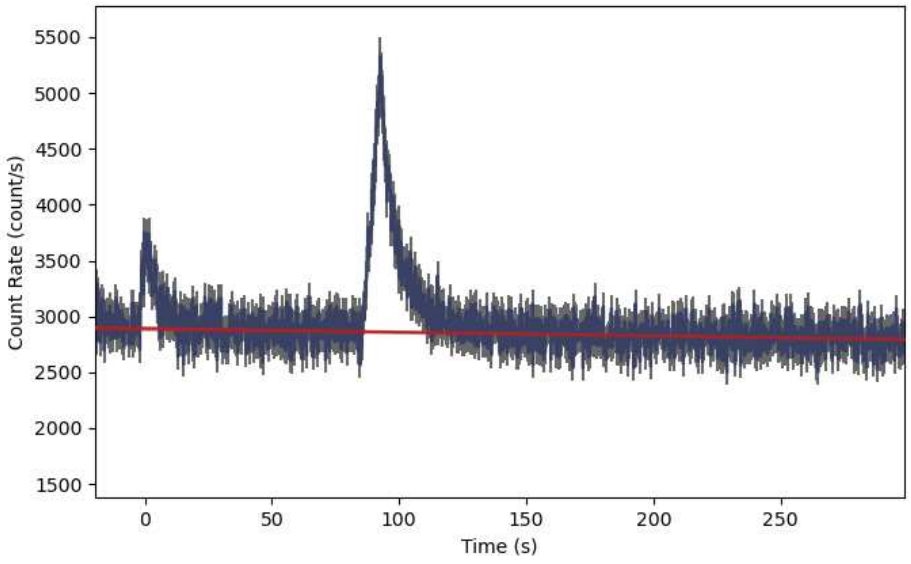

Figure 3.53: Example of the procedure of background subtraction. The red line represents the linear fit of the background, that is then subtracted to the lightcurve.

The reworked file is the one used to study the microvariability. Since there might be bins of the lightcurve showing no signal, especially for lower timescales, a weighting factor, provided by the denoised curve, is applied to the data. In this way the identification of the variations in the spectrum is optimized. The denoised curve is obtained following a technique described in [59]. It consists in using again

the non-decimated Haar wavelet transform on the lightcurve, and then apply an adapting threshold to the coefficients obtained for every scale. The article presents two ways to apply the threshold: hard threshold simply set at zero all the coefficients with absolute value below the threshold limit; the soft threshold applies the same rule, and in addition it reduces the other coefficients by the threshold value. The choice of a hard threshold seems more appropriate for the weight calculation since the separation between the time intervals with signal and those without is more sharply defined. From the newly calculated coefficients, the lightcurve is reconstructed, without the Poisson noise.

The structure function is then calculated, as described in the previous section, for several timescales, starting from 0.2 ms. As shown in Figure 3.52, there is an initial phase where the burst and the noise are not distinguishable. For this reason a threshold is fixed at 3σ above the Poisson fluctuations level. In this way the deviation from linearity in the structure function can be determined. Two possible methods are considered in this work. The first one is taken from paper 4, and

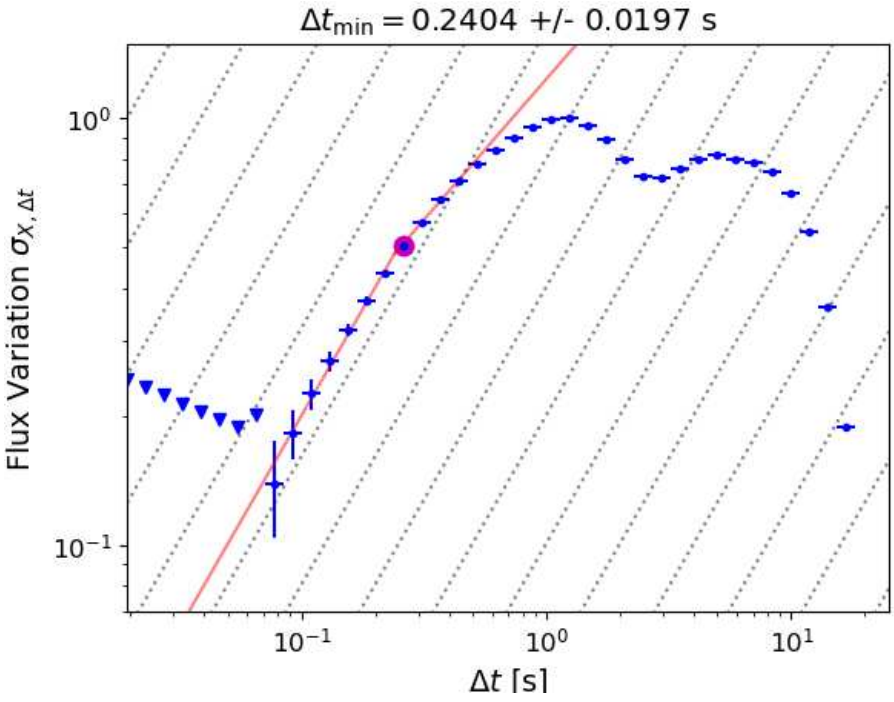

Figure 3.54: Microvariability calculation for GRB080730B, using the Butler method. The red line shows the initial linear phase, followed by a flatter phase, with the intersection highlighted by the red dot. The triangles represent the 3σ Poisson noise threshold for the timescales where $\sigma_{X,\Delta t}$ is lower than this limit.

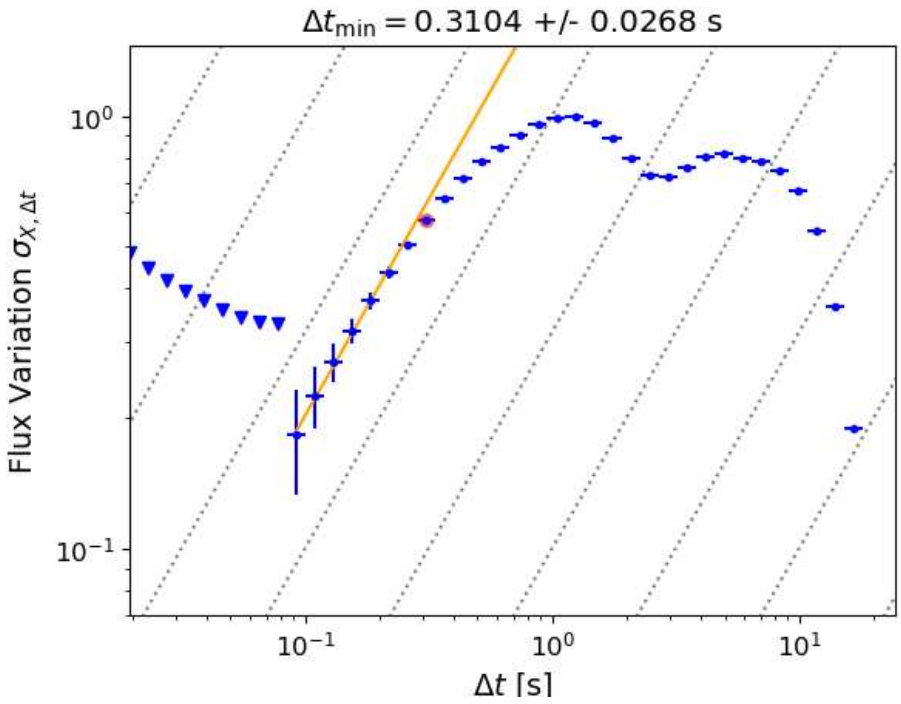

Figure 3.55: Microvariability calculation for GRB080730B, using the new method. The orange line shows the best fit of the linear phase. The red dot shows the timescale corresponding to the end of the linear phase. The triangles represent the 3σ Poisson noise threshold for the timescales where $\sigma_{X,\Delta t}$ is lower than this limit.

was provided directly by one of the authors N. R. Butler (called Butler method from here on). Looking at the scaleogram, the microvariability is given by the intersection between two straight lines, one fitting the linear phase of $\sigma_{X,\Delta t}$, the other one the subsequent flatter region. The second method (called new method henceforth), developed during the course of this work, consists instead in finding the best linear fit for an increasing number of $\sigma_{X,\Delta t}$ values, and for each fit verify with a chi-square test (α = 0.05) up to which timescales the linear fit works. By progressively considering more values, the fits are initially expected to improve (while in the linear growth phase) until the curve starts to flatten and the chi-square deteriorates. Both techniques are shown in Figure 3.54 and Figure 3.55, applied on the same GRB. In general, it is observed that the microvariability obtained with the first method corresponds to lower times than the ones obtained with the second one, as for the case shown here. This will become more evident in the next section.

As pointed out in paper 4, it is interesting to notice how the scaleogram also provides more information looking at the behaviour at higher timescales. In the example given above, at around 1 s the $\sigma_{X,\Delta t}$ starts to decrease. This timescale

should correspond to the overall envelope emission.

To demonstrate that the microvariability values, obtained with the new method, correspond to the shortest variations of the GRBs, they are identified in the lightcurve. In Figure 3.56 the lightcurve of GRB080730B is reproduced, with a denoised version of it overlaid. A zoomed image of the region presenting the shortest variability, localized by eye, is also provided. Here it is confirmed that the value found correspond to what is seen in the lightcurve. This does not mean that the other method is wrong, there are other cases in which the shortest variability is closer to what is found with the Butler method, or even in between the two values.

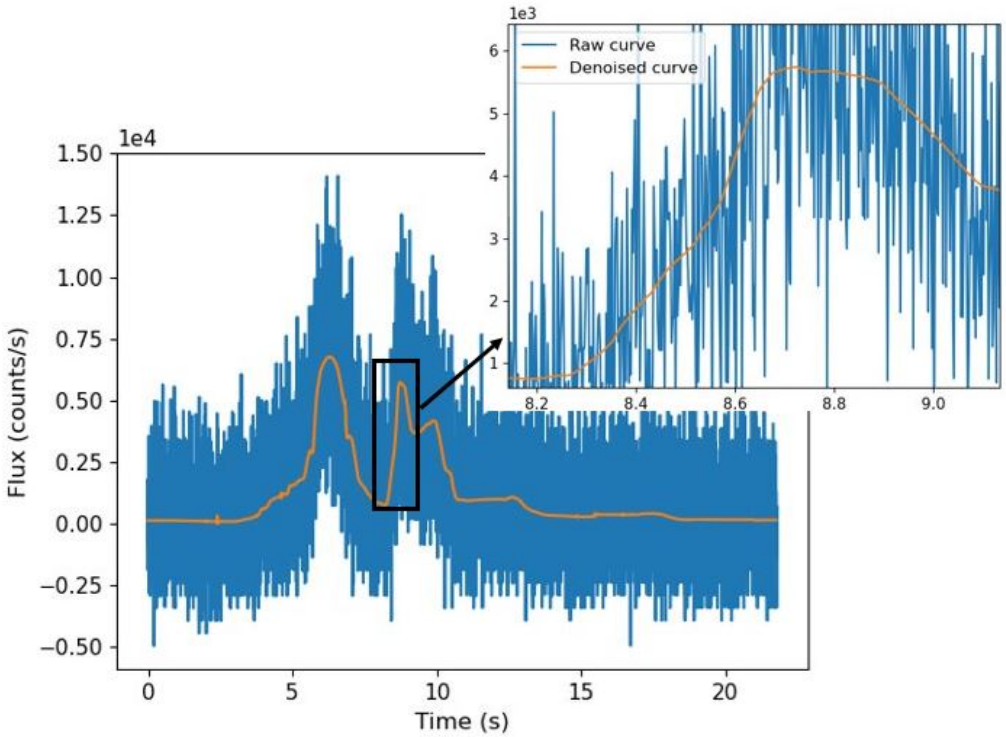

Figure 3.56: Lighcurve of GRB080730B from the raw data and its denoised version. The region showing the shortest variability is identified with a black frame and zoomed in the stacked plot, where it can be seen that the variation starts around 8.3 s and ends between 8.6-8.65 s.

Depending on which is the first timescale above the 3σ lower limit (strongly correlated to the signal-to-noise ratio, SNR, of the burst) it is also possible that the linearity phase is never observed in the scaleogram. In this case the first point above the limit is considered as an upper limit of the microvariability. However

it can also happen that there are no values above the threshold (again for GRB SNR reasons). In this case the approach is different between the two methods. The Butler method checks for the last four timescales below the threshold if the structure function value is higher than 1σ. Generally this operation ends up finding an upperlimit value for the microvariability. In some cases this value is too high to be realistic (like in the example shown in Figure 3.57). Instead, in this work it has been decided to eliminate these GRBs since it is not clear how meaningful the upperlimit value obtained is.

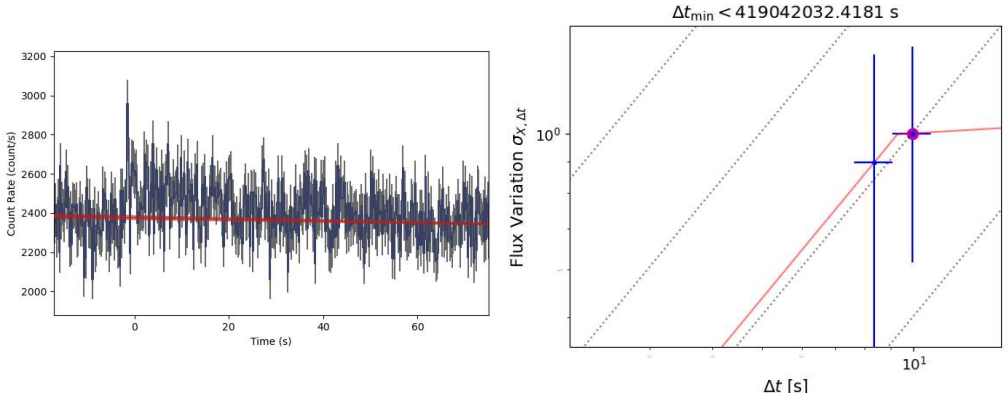

Figure 3.57: Example of a case with no values above the 3σ threshold. The GRB represented here is GRB101202, its lightcurve is shown on the left. The GRB start at 0s and has a T_{90} of approximatively 18s. It is a very faint GRB as it can be seen. Consequently the scaleogram should not show any $\sigma_{X,\Delta t}$ values above the threshold (which is the case with the new method). On the right image is shown the result of the solution adopted by the Butler method, in this case obtaining a too high upperlimit.

3.3.3 Microvariability for GBM GRBs

The analysis reported here has been conducted on the GRBs detected by Fermi GBM between the 2008 July 14th and 2021 October 18th. During this period of time, the telescope observed 3155 bursts. To ensure that the results are consistent for every GRB, if the data files of the detectors do not contain the full GRB or not enough data to estimate properly the background that GRB is discarded. This is the case for 93 GRBs. For twelve of them there is no file at all to download from the archive. The remaining 3062 GRBs, divided in 511 short and 2551 long, are subjected to the process described above for the calculation of the microvariability. Except for a few GRBs with unrealistic upperlimit value (too high) the Butler

method finds the microvariability (or an upper limit) for all the GRBs. With the new method there are 41 GRBs that are not bright enough to extract their variability from the noise, leaving 504 short GRBs and 2517 long GRBs to analyze. The initial analysis is done covering the full energy range observed by the NaI detectors, which goes from 8 keV to 1 MeV, even if the effective area drops rapidly below 20 keV, as shown in Figure 3.58.

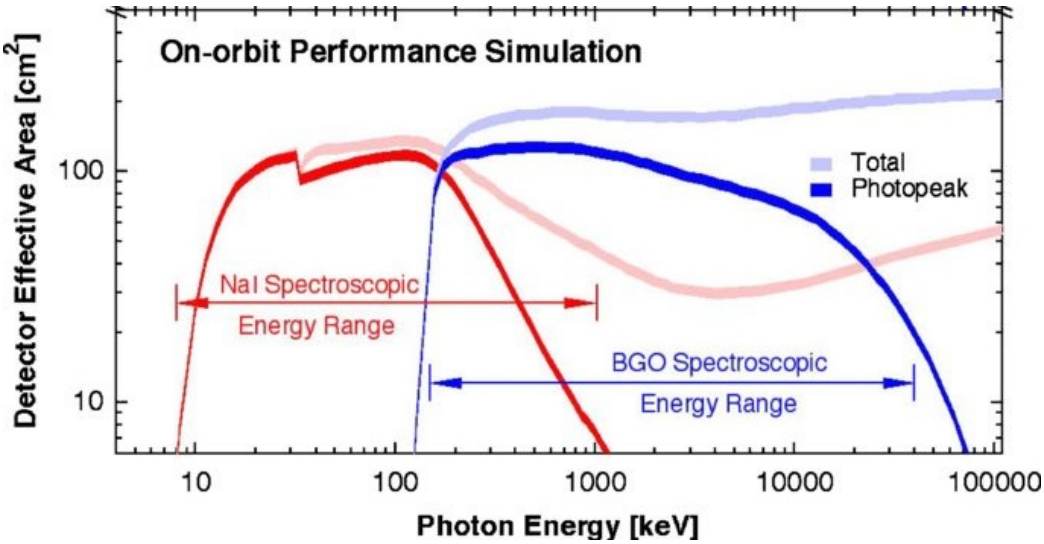

Figure 3.58: Fermi GBM effective area, for both detector types, determined at normal incidence. The shadowed region shows the increase of the effective area above a few hundreds keV due to photon scattering inside the spacecraft into the detectors [60].

The first results presented are the histograms showing the distribution of the microvariabilities for both methods. This demonstrate what was anticipated before, that the Butler method finds lower microvariability timescales. The median value obtained for long GRBs is 582 ms, with values contained between 6.2 ms and 126 s, while for short GRBs it is 53 ms, with values contained between 2.3 ms and 2.40 s. These values are higher than those presented in paper 4 because the upper limits value are considered as the microvariability of the bursts, contrary to what was done in paper 4 where the median was calculated using a Kaplan-Meier survival anlysis. However looking at Figure 3.60 it can be seen that considering separately the GRBs with measured microvariability and upperlimit, the distribution for the former is very similar to the one obtained in paper 4, while the latter is shifted to higher values. Considering only the measured microvariabilities, the median value is 411 ms for long GRBs and 41 ms for short ones.

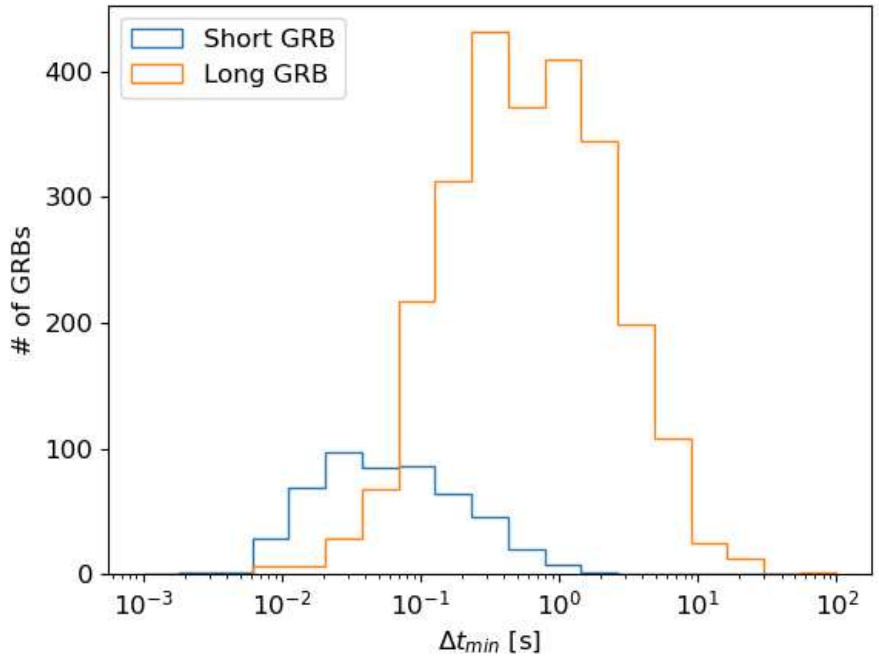

Figure 3.59: Histogram showing the distribution of the microvariability for short and long GRB, observed by Fermi GBM with the Butler method.

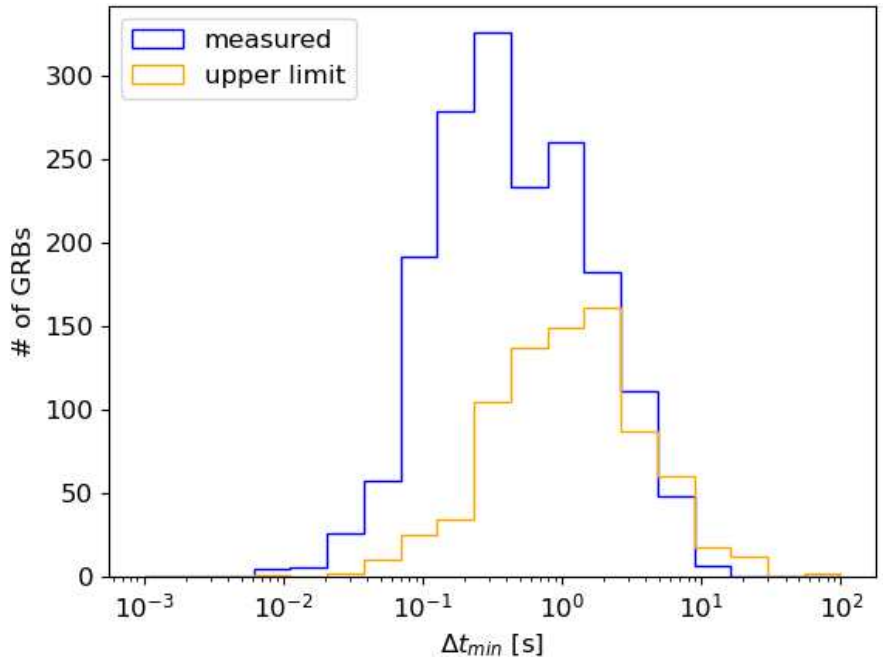

Figure 3.60: Histogram showing the distribution of the microvariability in both measured and upper limit cases, for long GRBs, with the Butler method.

Instead, with the new method the median value found for long GRBs is 738 ms, with values contained between 8 ms and 47.2 s, and for short ones is 78 ms, with values contained between 5.4 ms and 2.48 s. With this method there are no upper limit values. Between the values obtained with the Butler method and the new method there is a factor 1-3, but the shape of the histograms are very similar, confirming that the new method is more conservative. It becomes evident from Figure 3.62.

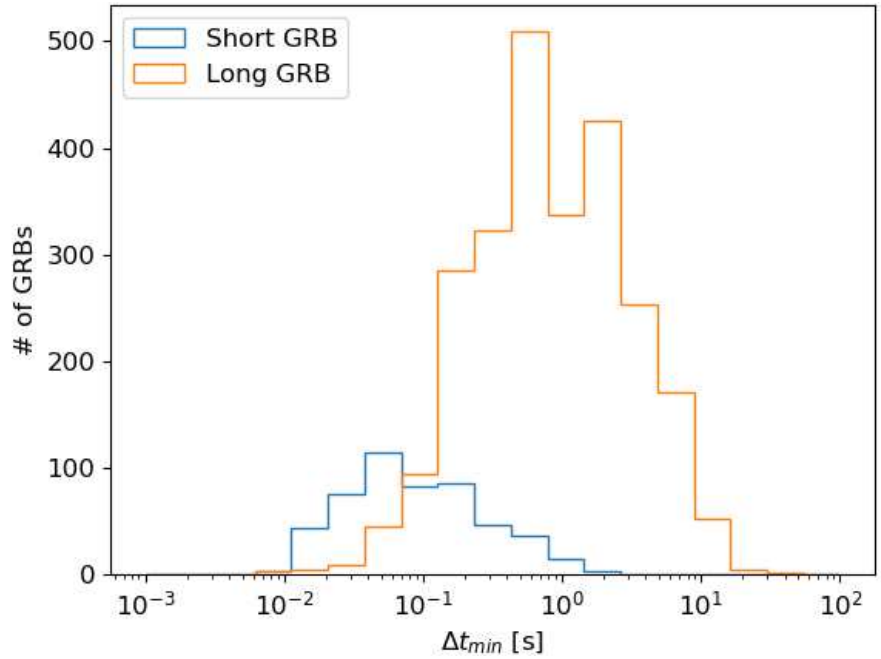

Figure 3.61: Histogram showing the distribution of the microvariability for short and long GRB with the new method.

The correlation between the microvariability and the duration of the bursts is not straightforward. Even if there seems to be a linear relation, especially for the short GRBs, the microvariability tends to stabilize below one second.

Over the last decades many studies have been pointing out that examining the spectrum of a GRB the peaks tend to become narrower for higher energies bands [61] [62]. Consequently it is expected that the same happens for the microvariability, since it was demonstrated before that the value found for the microvariability corresponds to the shortest rise time fluctuation. The full energy range is divided in two bands: the first one goes from 20 keV to 100 keV, the second one from 100 keV to 1000 keV. The results are shown for both the Butler method (Figure 3.64)

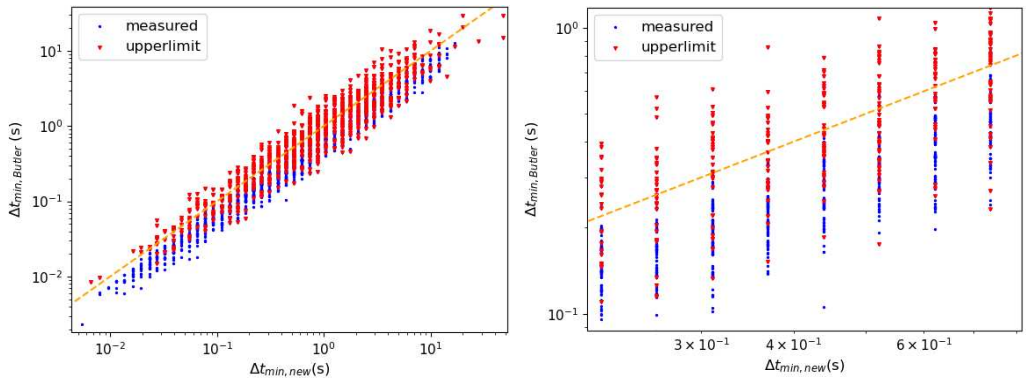

Figure 3.62: Comparison between the microvariability obtained with the Butler method and the one obtained with the new method for the same GRB, over all the GRBs analyzed with the new method. The dashed orange line represents the $\Delta t_{min,Butler} = \Delta t_{min,new}$ relation. It is apparent that for the majority of the GRBs the Butler method provides the shorter microvariability, and when this is not true it usually coincides with a case of upperlimit for the Butler method (there are no upperlimits for the new method).

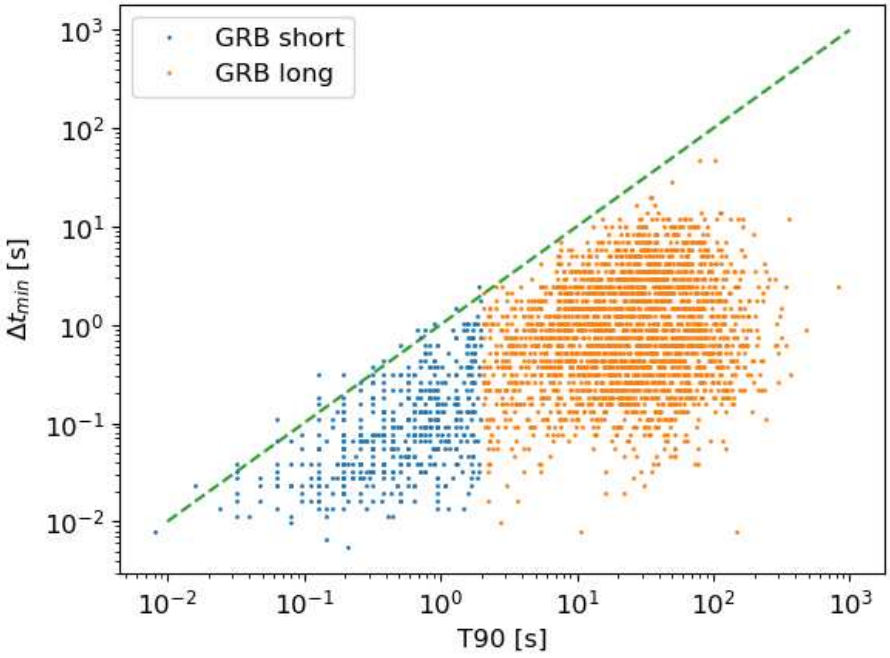

Figure 3.63: Plot of the microvariability versus the T_{90} for long and short GRBs. The dashed green line represents the $T_{90} = \Delta t_{min}$ relation. The errorbars on both x and y directions of the few points above this line intersect with this line justifying the fact that the Δt_{min} is longer than the burst itself.

and the new method (Figure 3.65). For short GRBs the behaviour is well defined: for higher energies (100-1000 keV) the distribution of the microvariability is shifted to lower values compared to the same distribution for lower energies (20-100 keV). This is true for both methods. The situation is different analyzing long bursts: the microvariability distribution at high energies has more important tails, showing not only more cases with low microvariability ($< 10^{-1}$s) than at lower energies, but also with high microvariability (> few seconds). Instead, the majority of the values measured at low energies is concentrated in the central region.

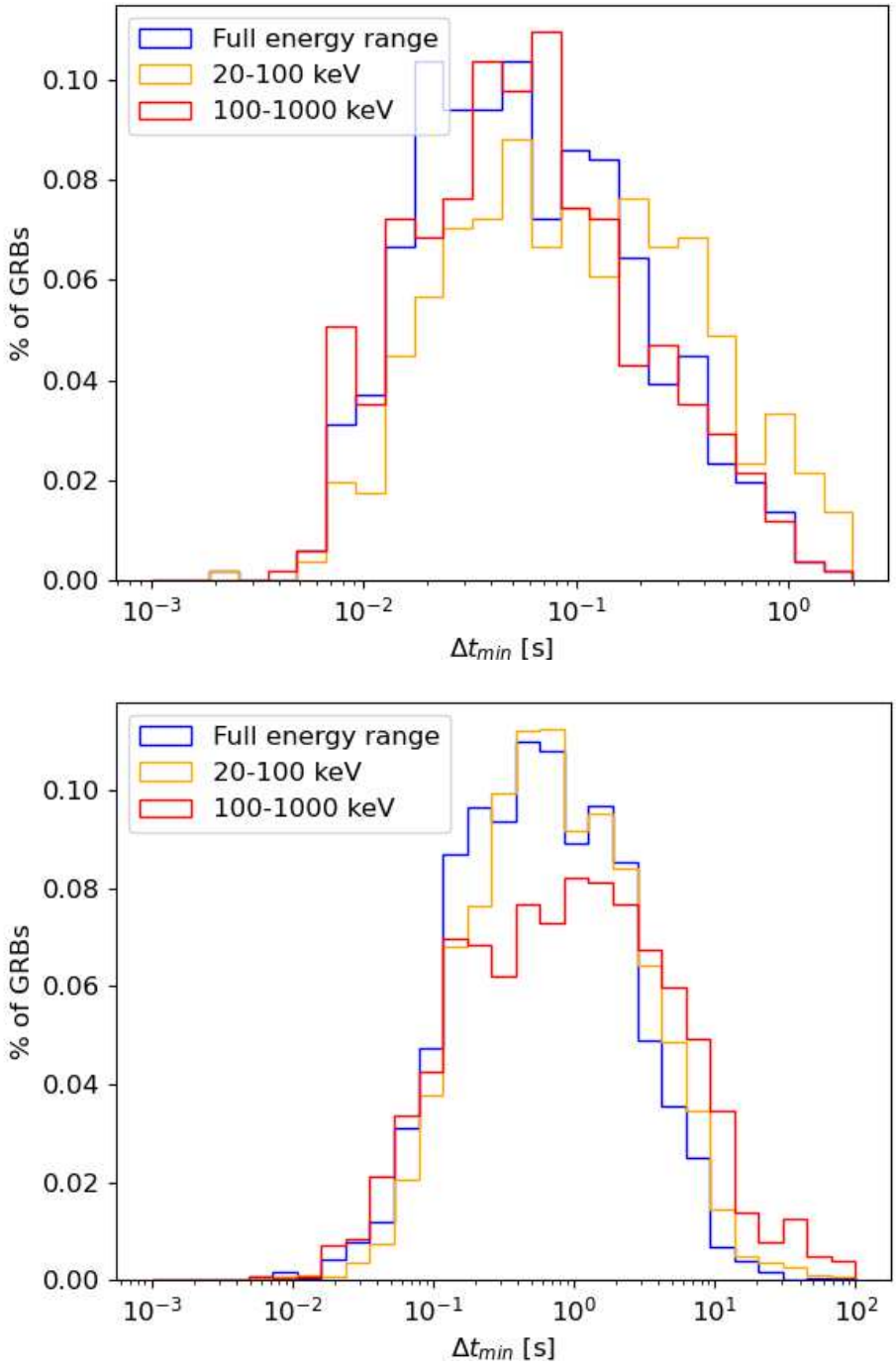

Figure 3.64: Histogram of the microvariability for the low energy (20-100 keV), high energy (100-1000 keV) and full energy range channels, obtained with the Butler method. On the top image is presented the distribution for short GRBs, in the bottom one for long GRBs.

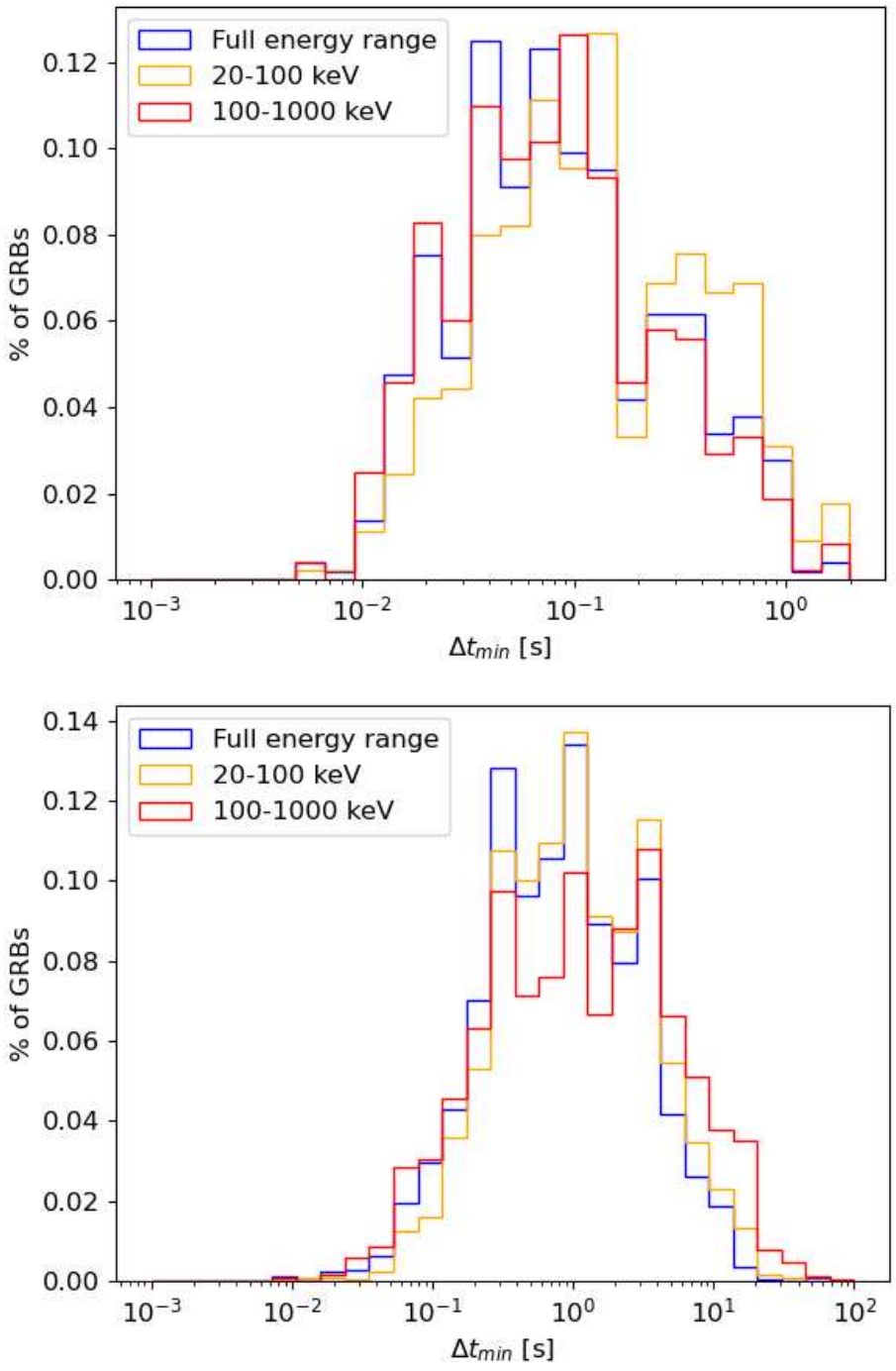

Figure 3.65: Histogram of the microvariability for the low energy (20-100 keV), high energy (100-1000 keV) and full energy range channels, obtained with the new method. On the top image is presented the distribution for short GRBs, in the bottom one for long GRBs, expressed in percentage since the number of GRBs for which the Δt_{min} is found can vary from one energy range to another.

3.3.4 Microvariability with redshift

To further explore the relation between energy (in particular the peak energy and the isotropic energy) and variability, it is necessary to have one more information about the GRBs, which is the redshift. Only for a small number of the selected set of GRBs this value is available (obtained from [63]). The "redshifted" set contains 171 GRBs, divided in 24 short and 147 long. Notice that the T_{90} has been recalculated in the cosmological rest frame dividing it by $1 + z$. For this reason there are short GRBs at very high redshift (even z$\sim$ 8). These GRBs are particularly interesting because their classification is the subject of much discussion since they present characteristics of both short [64] and long [65] [66] bursts. This contributes to the debate about keeping the traditional division short/long or moving towards using other characteristics to classify GRBs (e.g. the Amati relation [67]) [68] [69]. The microvariability could be an additional tool to assign the GRBs to a certain category. Using the T_{90} in the observer frame, the set composition is of 16 short and 155 long GRBs.

The first aspect investigated is a possible relation between the microvariability, in the rest frame as for the T_{90} ($\Delta t_{min,z}$), and the redshift itself (Figure 3.66). For both methods it seems that there are no particular distributions: both short and long minimum variabilities are visible at low and high redshifts.

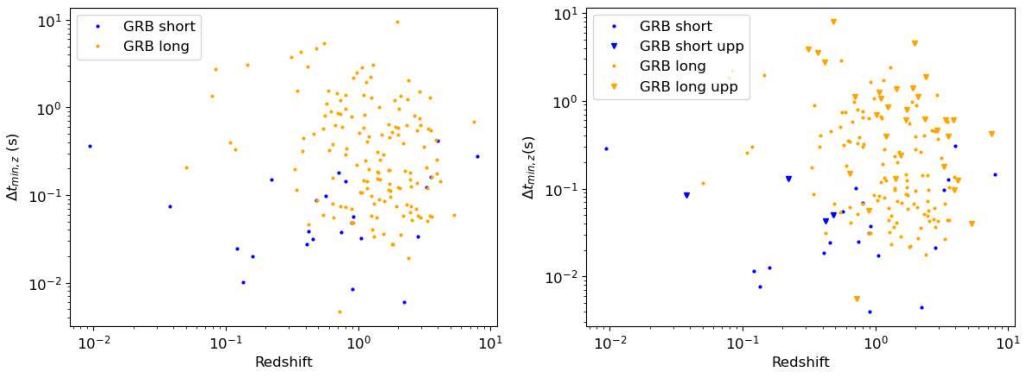

Figure 3.66: Plots showing redshift vs $\Delta t_{min,z}$ with the redshifted T_{90} division, obtained with the new method (left image) and the Butler method (right image).

The same plot, but with the division between short and long made using the observer frame T_{90}. With this division there are no more short GRBs at redshift higher than z$\sim$2. However this does not provide new information since again, for both long and short GRBs, the microvariability seems to be independent from the redshift.

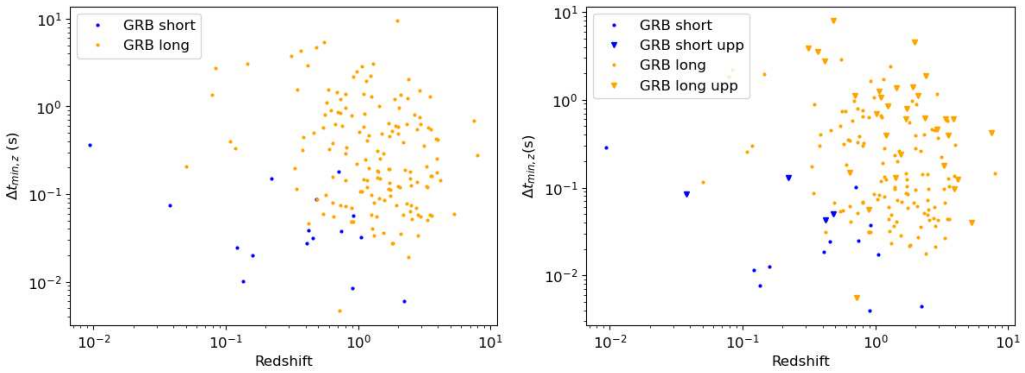

Figure 3.67: Plots showing redshift vs $\Delta t_{min,z}$ with the observer T_{90} division, obtained with the new method (left image) and the Butler method (right image).

Because of the relation between energy and narrowness of the peak, it is important to compare the isotropic energy, E_{iso}, which is the total energy radiated during the burst, with the corresponding $\Delta t_{min,z}$ for each burst. From now on the division short/long is done using the T_{90} calculated in the cosmological rest frame. The E_{iso} is obtained as follows:

$$E_{iso} = \frac{4\pi D_L^2 S_{bol}}{1+z}$$

where D_L represent the luminous distance of the GRB from the observer, calculated from the redshift using $H_0 = 70$ km s^{-1} Mpc^{-1}, $\Omega_m = 0.3$ and $\Omega_\Lambda = 0.7$ [70], and S_{bol} is the bolometric fluence calculated between 10 keV and 1 MeV, provided by the Fermi GBM catalog.

There are two main information to retain from the E_{iso} vs $\Delta t_{min,z}$ plots (Figure 3.68). The first one concerns long GRBs, for which higher isotropic energies correspond to lower microvariability values, with a power law trend. It could be asserted that this relation is true also for the fluence. For this reason another study E_{iso} vs $\Delta t_{min,z}$ is provided showing only the GRBs with an high fluence ($> 2 \cdot 10^{-5}$ erg/cm^2). As it can be seen in Figure 3.69, these GRBs are not all concentrated at high isotropic energies/low microvariability, but the power law behaviour is still evident, suggesting that the dependence of E_{iso} on $\Delta t_{min,z}$ is genuine.
The reason of this relation is not yet clear. It can be speculated that higher isotropic energies correspond to more collimated beam. It has also been pointed out that the microvariability is related to the activity of the inner engine. In an internal shock model, where two shells emitted at different times with different velocities collide,

the microvariability can be used to estimate the jet angular opening distance, L, equal to $c\Delta t_{min,z}$. This quantity is related to the distance of the central engine from the γ-ray production site, defined as $R \sim 2\Gamma^2 L$, where Γ is the velocity of the the shell resulting from the collision. Consequently the microvariability is related to all of these physical parameters that regulate the inner engine. This will be subject of a follow up study.
There are a few outlayers, corresponding to GRBs with low redshift that display a lower isotropic energy than what could be expected. It is speculated that these GRBS could be observed off-axis, resulting in a lower isotropic energy, or even GRBs classified as long, but actually but with a central engine characteristic of short GRBs.
The second interesting aspect concerns the short GRBs (in the rest frame) at high redshift. Comparing Figure 3.66 and Figure 3.67, one notices that above $z = 2$ there are six short GRBs in the former image and only one in the latter one. For both methods in Figure 3.68, it is simple to identify these same GRBs, from the dimension of the points and the minimum variability value. As it can be seen in the images, the five GRBs oscillating between large and short, depending on the chosen frame, are separated from the other short bursts and behave like the long ones, while the one always classified as short is far from this region. This could be another element in favor of the argument that these bursts should be classified with the long ones, despite their T_{90} in the rest frame, and consequently supporting the idea that the traditional division is becoming obsolete. Considering the other three GRBs (at $z < 2$, identified by a circle) characterized as short in the rest frame but not in the observer one, one of them is again on the border of the long GRBs region, while the other two are more similar to the other short GRBs.

Another characteristic value of the GRB is the peak energy, the energy at which their νF_ν spectrum shows the highest value. In order to have an peak energy associated to it, the spectrum must be of one the two following types that are used in the Fermi GBM catalog: Band and Compton. The first model was already presented in the first chapter, the second one is consists in an exponentially attenuated power law. Unfortunately, requesting only the GRBs that have their spectrum best fitted with one of these two models (information available requesting 'flnc_best_fitting_model') further reduces the set of GRB with redshift available, since there are GRB spectra best fitted with only one power-law. Consequently there are only 98 GRBs, 10 short and 88 long, to analyze. The energy peak is calculated in the rest frame by simply multiplying the value found (model name + '_epeak') in the calatog by $(1 + z)$.

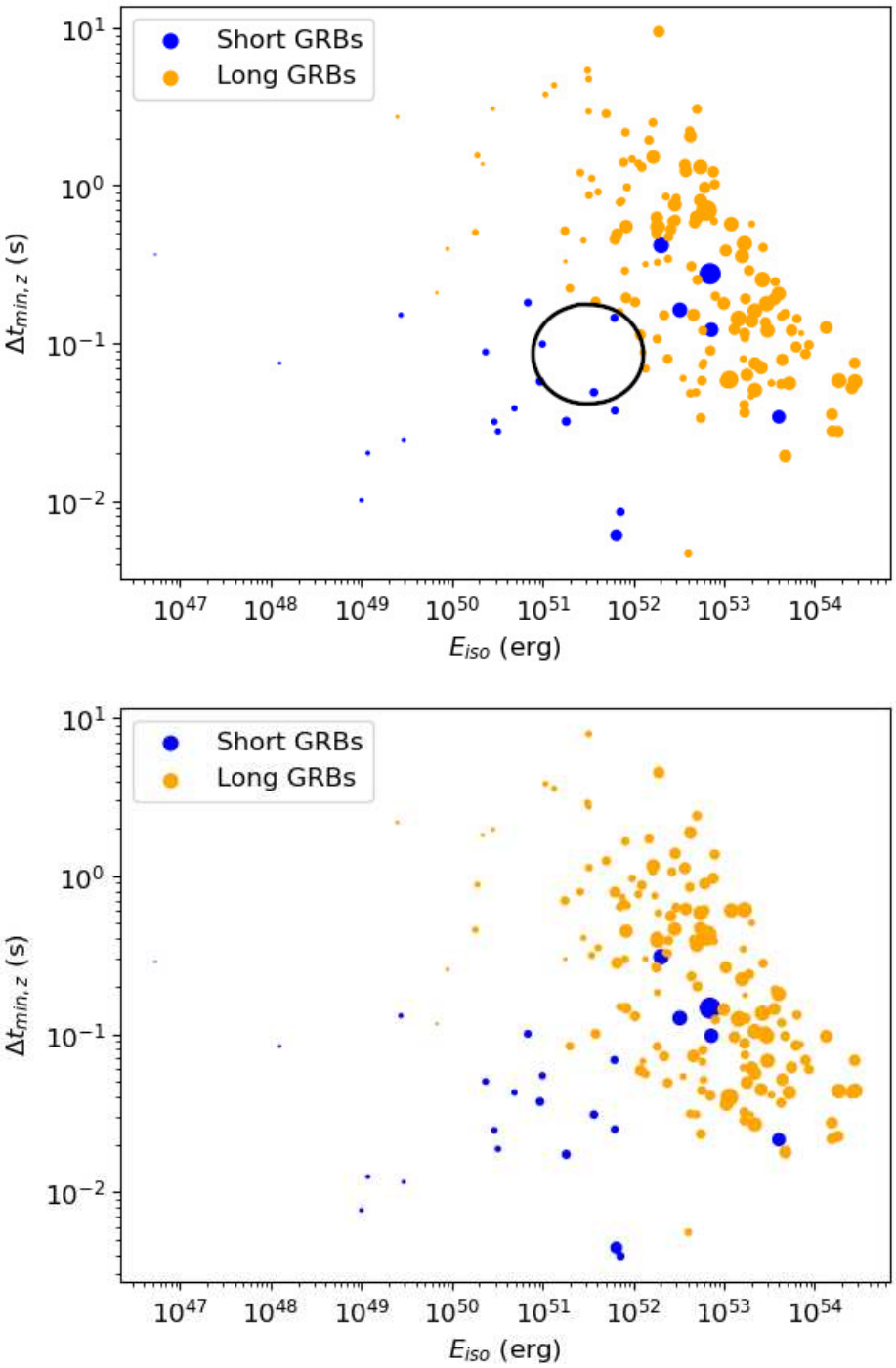

Figure 3.68: The images show the dependence on the isotropic energy of the microvariability, obtained with the new method (top image) and Butler method (bottom). The dimension of the points is proportional to the redshift.

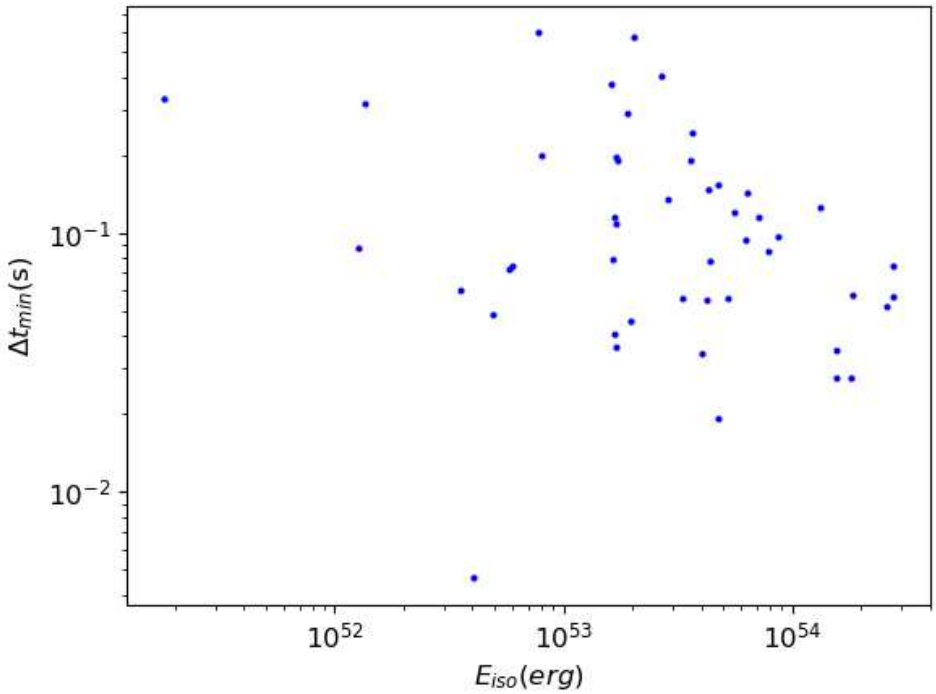

Figure 3.69: Plot showing the dependence on the isotropic energy of the microvariability, obtained with the new method, for long GRBs with high fluence ($> 2 \cdot 10^{-5}$ erg/cm^2).

What is extrapolated from the plots is again a relation between the energy and the narrowness of the peaks.There is no clear division between short and long GRBs, but this could be due to the low amount of cases, especially for the short bursts. It will be possible to investigate further on this aspect when a larger number of of such bursts will be detected. However, it must be noticed that the short bursts values seems to follow a power-law relation. The long GRBs too display shorter microvariabilities at higher peak energies, but the values are more spread out.

Using a linear regression separately on the short and long GRBs, the two following relations are found: for the short GRBs the power-law goes as $\Delta t_{min,z} \propto E_{peak}^{-0.93}$, for the long GRBs as $\Delta t_{min,z} \propto E_{peak}^{-0.60}$. The linear regression is done only on the new method values since the presence of upperlimits in the Butler method requires another type of analysis.

Finally, the last intensity parameter that was compared to the microvariability is the peak luminosity (again, only for the GRBs with redshift). From studies car-

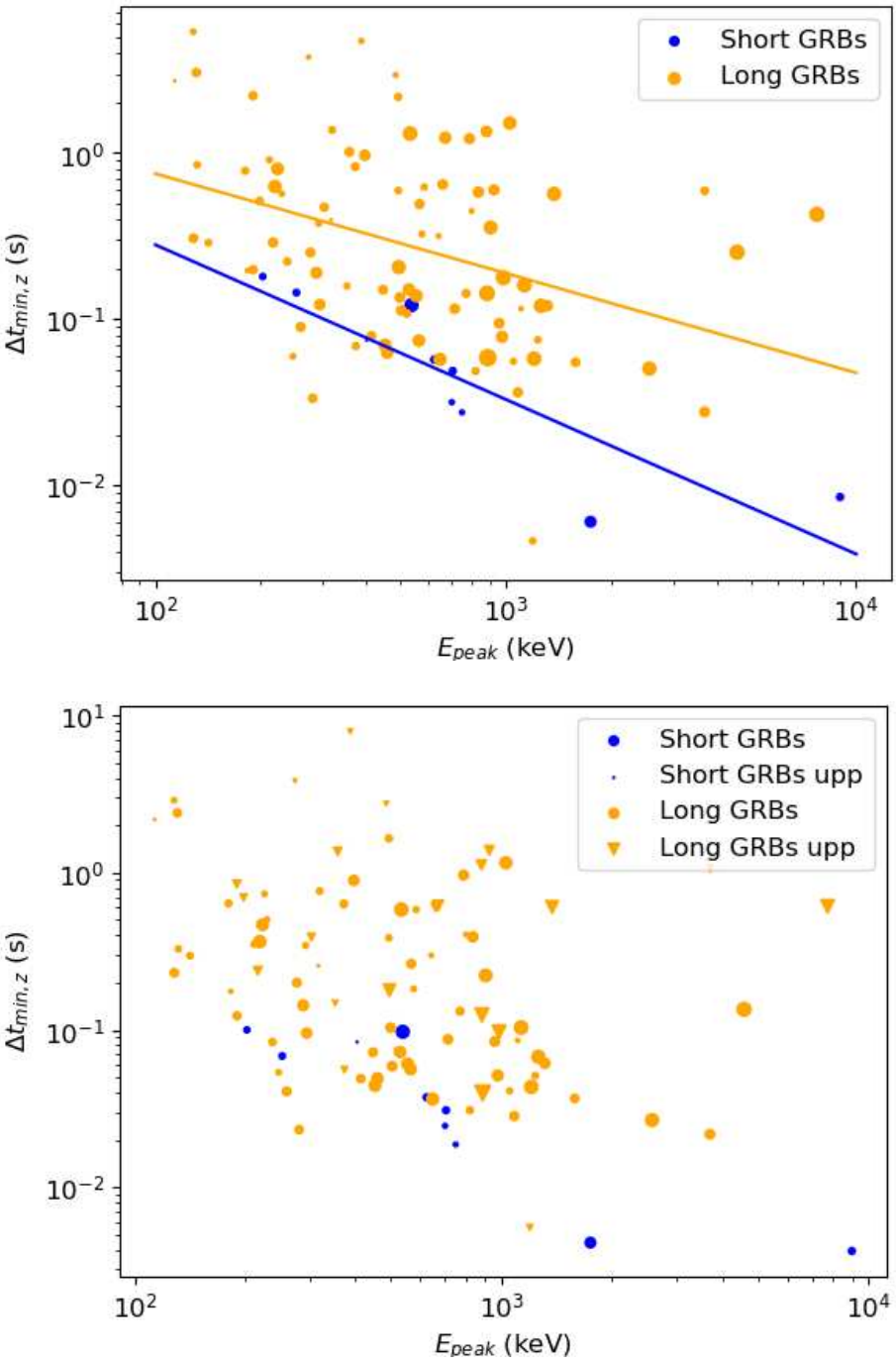

Figure 3.70: The images display the peak energy for each burst, with a Band or Compton-type νF_ν spectrum and with redshift, compared to its microvariability, obtained with the new method (top image) and Butler method (bottom). The dimension of the points is proportional to the redshift. In the top image, the blue line represents the linear regression for the short GRBs, while the orange line the one for long GRBs.

ried out a couple of decades ago, prevalently on BATSE GRBs with a pseudo redshift [71][72][73], it was found out that there is a power-law relation between the variability of the GRB lightcurve and the peak luminosity. In these articles the variability is obtained in a similar way to the normalized activity but only for one fixed timescale for all the GRBs analyzed, corrected for the time dilatation. The objective is to investigate if this relation exist also for the minimum variability. The peak flux, F_p, requested from the catalog is the one measured at a time binning of 256 ms ('flux_256'). This provides the value in counts s^{-1} cm^{-2}. To obtain the energy flux, F_E, the following relation is used:

$$F_E = 1.6 \cdot 10^{-9} \frac{\int_1^{10^4} N(E) E\, dE}{\int_1^{10^4} N(E) dE} F_p$$

where $1.6 \cdot 10^{-9}$ is the conversion factor from keV to erg, $N(E)$ is the time-integrated spectrum obtained from a Band model with $\alpha = -1$, $\beta = -2$ and energy peak provided by the catalog for each GRB.
From that value the peak luminosity is obtaines as follows:

$$L_{peak} = 4\pi D_L^2 F_E$$

Looking at (Figure 3.71) the relation between the microvariability and the peak luminosity is not as well defined as in the articles cited above. Two lines with a slope of -0.5 are plotted to guide the eye and identify a relation between the two quantities, which is that the microvariability decreases for higher values of peak luminosity. The reason for this more scattered distribution could be due to the limited information provided by the Fermi catalog.

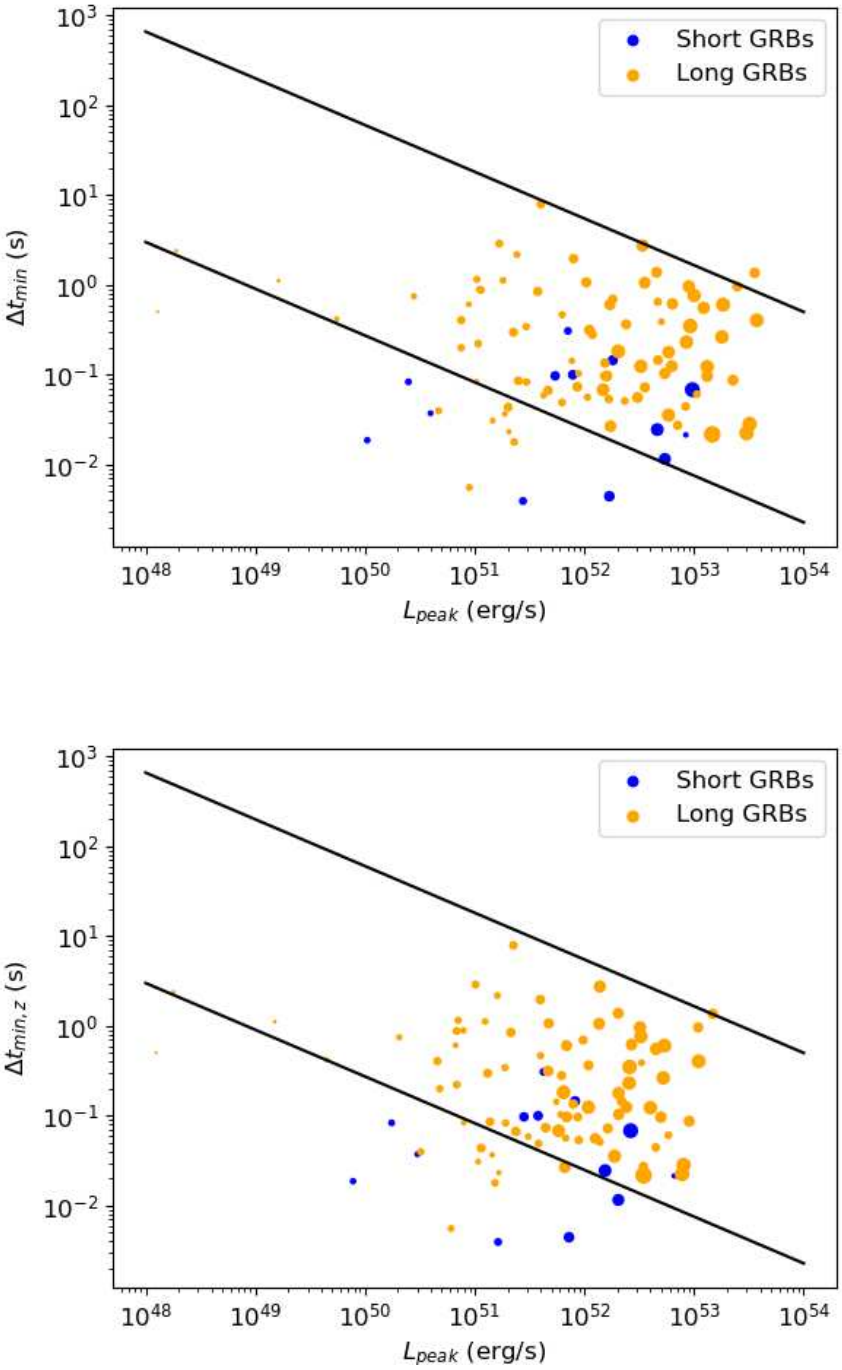

Figure 3.71: The images display the peak luminosity compared to the microvariability, obtained with the new method (top image) and Butler method (bottom). The dimension of the points is proportional to the redshift. The black lines, with slope -0.5 are there only to guide the eye along the decreasing microvariability as luminosity increases.

3.3.5 HERMES Pathfinder results

Until now, it has been always considered that there is no microvariability below tenths of millisecond. What if this is actually possible? The GRB221009A, with its extreme brightness and very narrow peaks could be a possible candidate. However since it saturated the detectors the analysis is complicated, and having been discovered towards the end of this doctorate work the study of that GRB had to be postponed. This kind of GRB nourishes the hope that it is possible to find microvariability of the order of microseconds. Moreover, the HERMES Pathfinder nanosatellites will provide a better time resolution compared to Fermi GBM or Swift, making it possible to explore the time structure of the lightcurve up to 1µs (maybe even lower). It is therefore interesting to verify if the tool developed to obtain the microvariability is capable of identifying these very low values.

Using a script developed during this doctoral work, a GRB was simulated. This program allows to create as many peaks as required, by providing the scale of the exponential growth (faster) and then decrease (slower) for each of them, and their positions in time. For this study a GRB with three peaks was simulated, two of them wider (of the order of seconds) separated by a few tens of seconds, and the third one very short (few microseconds) in the middle. The GRB created is shown in Figure 3.72.

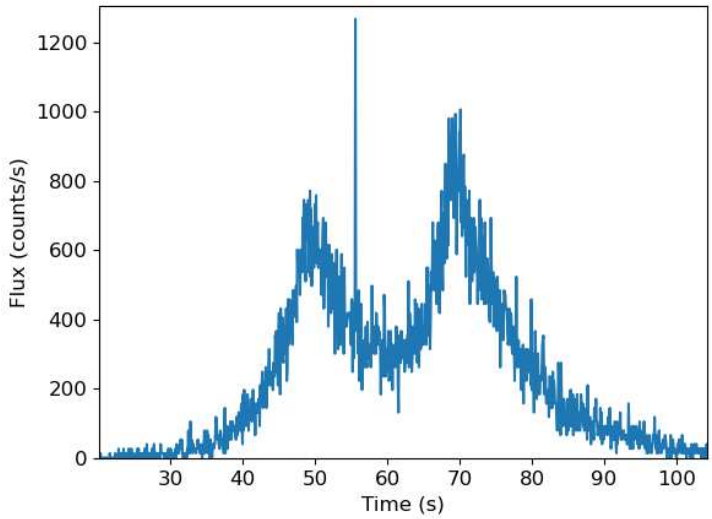

Figure 3.72: Lightcurve of a simulated GRB displaying a microsecond variability.

This lightcurve is then analyzed with both methods and the results obtained are very satisfying. Performing the calculation with the new method the value obtained for the microvariability is about 5 µs, while with the Butler method it

is equal to 4 µs, The result difference is consistent with the previous measures of the microvariability. The conclusion reached is that it is possible to measure microsecond variability using the tools presented in this chapter.

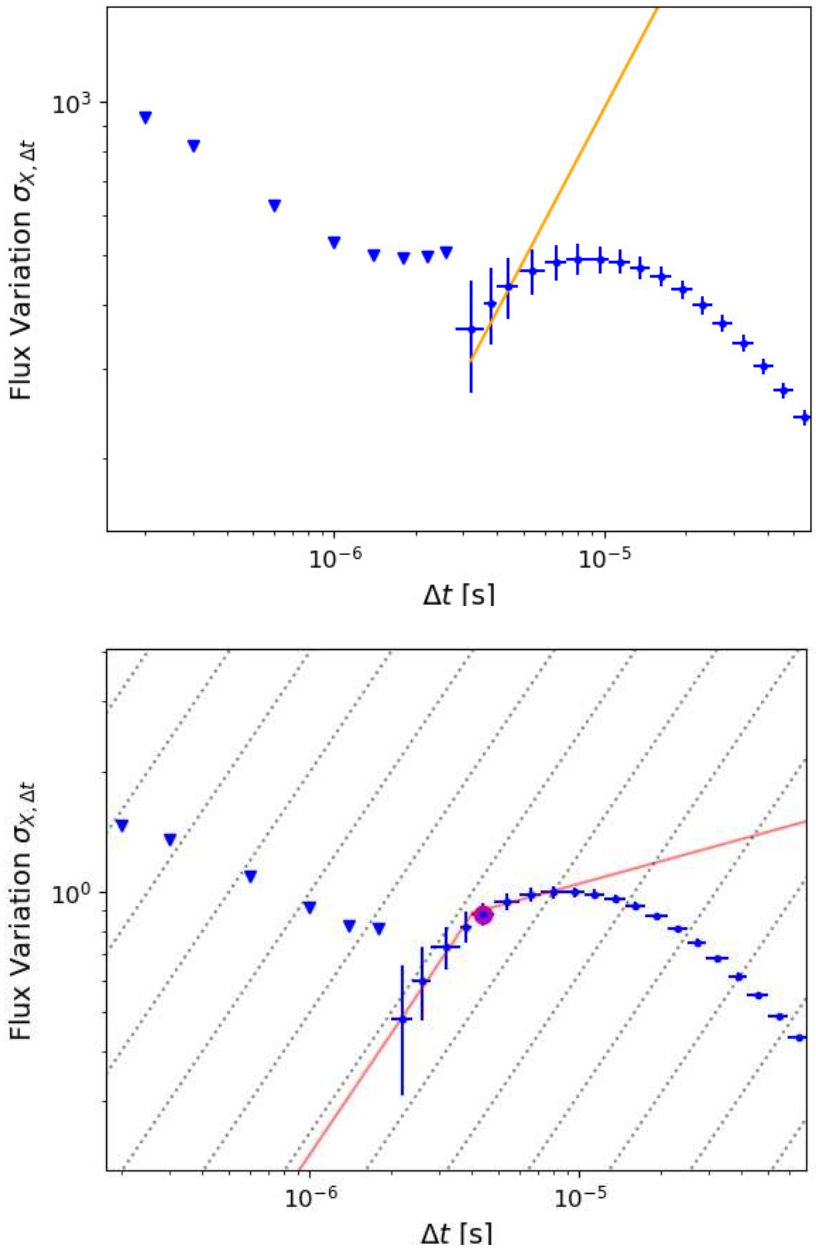

Figure 3.73: Scaleograms of the variability of the simulated GRB, to find a microsecond microvariability, with the new method (top image) and Butler method (bottom).

Conclusion

The HERMES Pathfinder mission has the ambitious goal to study the high energy transient sources using an innovative constellation of nanosatellites, that requires only a few years to be developed and with a cost at least one order of magnitude lower than the presently used satellites with the same scientific objectives. To satisfy the dimension requisites, a novel detector combination, based on the "siswich" architecture, consisting in coupling a crystal scintillator with a silicon detector, was employed, requiring a proper characterization. The study of the residual luminescence generated by the crystal scintillator, required the development of a sophisticated experimental apparatus to perform the characterization in optimal conditions. The experimental layout built to this purpose proved to be perfectly working, providing all the necessary information on the afterglow generated by the crystal, when irradiated with an UV LED light or with a beam of protons through several steps. The empirical model developed to explain the afterglow mechanism has proven to be correct, within the instrumental limitations. The fits carried out provided the parameters necessary to verify that the current generated by the afterglow in the SDDs, acting like a leakage current, does not prevent the proper funtioning of the electronics. Using a software for the simulation of the space environment (IRENE9), it was demonstrated that the afterglow current so generated reaches a peak value of a few pA (at 20 °C), which is largely below the imposed limit value (100 pA) for the leakage current. A second estimate was performed at 5 °C providing again comforting results.

With their launch currently planned for the end of the 2023/early 2024, the integration and calibration phase of the HERMES Pathfinder nanosatellites is underway. The first part of this study presented the analysis carried out after every step of the assembling of the detector for three of the flight models. During the functionality tests a few problems in the hardware were found out and solved. At the end of these functionality tests, the large majority of the channels ($\sim$ 90%) of each flight model displayed a correct read out. The effective light output also proved to be consistent with the expectations. The second part of the study consisted in the calibration of the Flight Model 1 nanosatellite fully integrated. The

calibration was performed at several temperatures between −20 °C and +20 °C. The calibration in both X-mode and S-mode provided excellent results.

Finally, the concept of microvariability of a gamma-ray burst was deepened in this work. A new method was developed from the study of previous papers, to extract the shortest time variation in the GRB lightcurve. The new method, more conservative, provides higher values (by a factor 1-3) compared to the previous method. The new method was then applied to a large set of GRBs (> 3000) observed by Fermi GBM, finding for the microvariability a median value of about 0.7 s for long GRBs, with a minimum of 8 ms and a maximum of 47.2 s, and 0.08 s for short ones, with a minimum of 5.4 ms and a maximum of 2.48 s. This study has confirmed the dependence of the microvariability from the energy range chosen: there is a tendance of the microvariability for short GRBs to provide shorter values at higher energies. Instead, for long GRBs the situation is more complex, with a broader distribution for higher energies at both shorter and longer microvariabilities.
The set of GRBs taken into consideration was then reduced to only those for which the evaluation of the redshift was possible. For these GRBs it is possible to calculate quantities like the isotropic energy, the peak energy (in the rest frame), and the luminosity peak. The dependence of the microvariability on the isotropic energy was demonstrated at least for long GRBs, finding that higher isotropic energies correspond to lower microvariabilities, although with a large scatter, and this does not depend on the fluence. It was also observed that some high redshift GRBs, that could be considered short in the rest frame for their T_{90} and long for other characteristics, present a long GRB behaviour. The peak energy study also provided an interesting relation with the microvariability. In particular, for the short GRBs a linear regression was attempted obtaining the following relation: $\Delta t_{min,z} \propto E_{peak}^{-0.93}$. For long GRBs the values are more dispersed, but a similar analysis provides the relation $\Delta t_{min,z} \propto E_{peak}^{-0.60}$.
Finally, this study verified that the developed tool is able to identify the microsecond variability observable by HERMES Pathfinder with its improved time resolution.

Appendix A

Mescal algorithm

The mescal general alghoritm proceeds as follow:

1. *Data readout*
   The input data is readout and organized in a Python `pandas` data frame, i.e., a table with rows representing a photon event and columns storing the relevant information.

2. *Event type discrimination and tagging, multiplicity filtering and histogram building*
   Events are tagged as "X-mode" or "S-mode", to discriminate between events generated directly in the SDDs and events generated in the scintillators. The logic behind the event discrimination process consists of looking at the list of the channels readout in the same trigger cycle, and tag events seen simultaneously by both channels reading the same crystal as 'S', otherwise as 'X'. Tags are defined and stored for each individual event. It is worth noting that this tag does not consider event multiplicity. Two spectra are then obtained, by building the histogram of 'X'- and 'S'-tagged events, respectively. These spectra only include events with multiplicity of exactly 1, for the former, and with multiplicity of exactly 2 for the latter.

3. *X-mode calibration*
   If at least one of the user-input radioactive sources is listed as a X-ray emitting calibration source, then the algorithm will attempt to perform energy calibration on the X-mode spectra. To achieve this, the relative differences between all known X-ray lines of all the radioactive sources are measured, in the energy space. Then, a peak-finding filter is run on the data. The peaks are chosen by comparing each local maxima to their immediate surroundings, defining a ranking of prominence for each line. These positions are

used as input for a Gaussian-profile fitting algorithm (using the `lmfit` package), which returns the best-fit peak position and full-width half maximum (FWHM) for each line.

The differences between these peak positions in the ADC space and in the energy space for each line are then compared, for different sets of N data lines, where N is the number of all the X-mode calibration lines that are being used. The set of N data lines with the smallest distance dispersion with respect to the calibration lines will be chosen, and identified with the respective calibration lines.

The set of pairs composed of the ADC value for the centroid of a data line and the energy value of its corresponding calibration line are given as input to a least-squares linear fit algorithm. The fit will return gain, offset and their errors for each channel. The console will list for which channels, if any, this calibration step failed.

Each event will then be separately calibrated for each channel in energy units, and a final calibrated X-mode event list will be created.

4. *S-mode calibration*
   If at least one of the user-input radioactive sources is listed as a γ-ray emitting calibration source, the algorithm will attempt to perform energy calibration on the S-mode spectra. Since the scintillator effective light output is referenced to the 661.67 keV ^{137}Cs line, the algorithm automatically uses the peak finding procedure to find this line, assuming it is the only line present. Then, a Gaussian-profile fitting algorithm is run on the position given by the peak finder, which returns the position of the center of the line and its FWHM.

   Then, for each channel, the algorithm takes the gain and offset parameters found during the X-mode calibration and converts the S-mode spectrum in units of electrons. This spectrum is then used to derive the light output for each single channel by fitting the 661.67 keV line.

   Finally, for each pair of channels reading the same crystal, the events are summed event-by-event in electrons and normalized to the sum of the light output of both coupled channels. This returns a crystal-summed event list in energy units. The console will list the channels, if any, for which this calibration step failed.

5. *Visualization plots and output writing*
   The program will ask the user to define what results to write as output tables, and which plots to be saved as output (Figure A.1)).

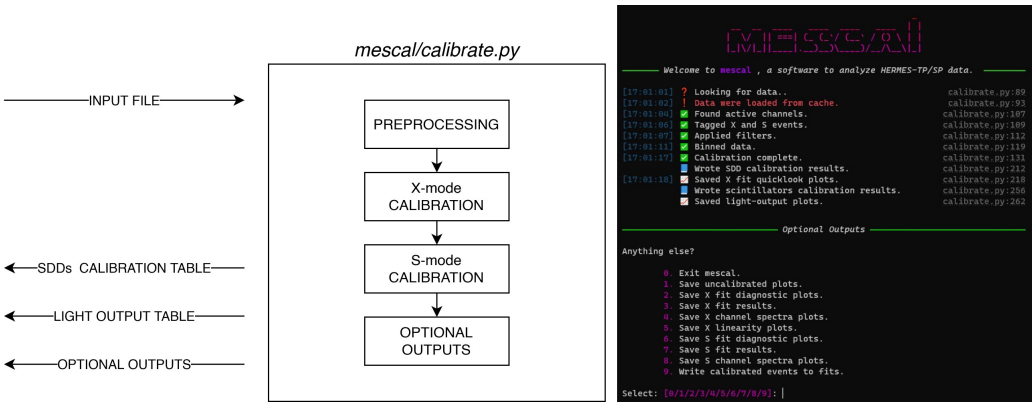

Figure A.1: Block diagram of the `mescal` logic structure (left image)and output option menu given by `mescal` (right image).

Bibliography

[1] The Fourth BATSE Gamma-Ray Burst Catalog (Revised)., W. S. Paciesas, et al., 1999, The Astrophysical Journal Supplement Series, Volume 122, Issue 2, p. 465-495, DOI: 10.1086/313224, arXiv:astro-ph/9903205

[2] Discovery of an X-ray afterglow associated with the γ-ray burst of 28 February 1997, E. Costa, et al., 1997, Nature, Volume 387, Issue 6635, p. 783-785, DOI: 10.1038/42885, arXiv:astro-ph/9706065

[3] Transient optical emission from the error box of the γ-ray burst of 28 February 1997, J. van Paradijs, et al., 1997, Nature, Volume 386, p. 686–689, DOI: 10.1038/386686a0

[4] SAX, the wide band mission for X-ray astronomy, L. Piro, 1996, Memorie della Societa Astronomica Italiana, Vol. 67, p. 575-591

[5] Spectral constraints on the redshift of the optical counterpart to the γ-ray burst of 8 May 1997, M. R. Metzger, et al., Nature, Volume 387, Issue 6636, p. 878-880, DOI: 10.1038/43132

[6] The Swift Gamma-Ray Burst Mission, N. Gehrels, et al, 2004, The Astrophysical Journal, Volume 611, Issue 2, p. 1005-1020, DOI: 10.1086/422091, arXiv:astro-ph/0405233

[7] A Photometric Redshift of z 9.4 for GRB 090429B, A. Cucchiara, et al., 2011, The Astrophysical Journal, Volume 736, Issue 1, article id. 7, 12 pp., DOI: 10.1088/0004-637X/736/1/7, arXiv:1105.4915

[8] A short γ-ray burst apparently associated with an elliptical galaxy at redshift z = 0.225, N. Gehrels, et al., 2005, Nature, Volume 437, Issue 7060, p. 851-854, DOI: 10.1038/nature04142, arXiv:astro-ph/0505630

[9] The Large Area Telescope on the Fermi Gamma-ray Space Telescope Mission, Fermi/LAT Collaboration: W. B. Atwood, et al., 2009, The Astrophysical Journal, Volume 697, Issue 2, p. 1071-1102, DOI:10.1088/0004-637X/697/2/1071, arXiv:0902.1089

[10] An Ordinary Short Gamma-Ray Burst with Extraordinary Implications: Fermi-GBM Detection of GRB 170817A, A. Goldstein et al., 2017, The Astrophysical Journal Letters, Volume 848, Issue 2, article id. L14, 14 pp., DOI: 10.3847/2041-8213/aa8f41, arXiv:1710.05446

[11] Teraelectronvolt emission from the γ-ray burst GRB 190114C, MAGIC Collaboration, 2019, Nature, Volume 575, Issue 7783, p. 455-458, DOI: 10.1038/s41586-019-1750-x, arXiv:2006.07249

[12] The HERMES-technologic and scientific pathfinder, F. Fiore, et al., 2020, Proceedings of the SPIE, Volume 11444, id. 114441R 15 pp., DOI: 10.1117/12.2560680, arXiv:2101.03078

[13] The Deep and Transient Universe in the SVOM Era: New Challenges and Opportunities - Scientific prospects of the SVOM mission, J. Wei, et al., 2016, arXiv preprint, 67 pp., DOI: 10.48550/arXiv.1610.06892, arXiv:1610.06892

[14] The SVOM Mission, J-L. Atteia, et al., 2022, International Journal of Modern Physics D, Volume 31, Issue 5, id. 2230008, 19 pp., DOI: 10.1142/S0218271822300087, arXiv:2203.10962

[15] https://www.svom.eu/en/the-svom-mission/ (last visited 04/05/2023)

[16] Introducing the CTA concept, B.S. Acharya, et al., 2013, Astroparticle Physics, Volume 43, p. 3-18, DOI: 10.1016/j.astropartphys.2013.01.007

[17] The THESEUS space mission concept: science case, design and expected performances, L. Amati, et al., 2018, Advances in Space Research, Volume 62, Issue 1, p. 191-244, DOI: 10.1016/j.asr.2018.03.010, arXiv:1710.04638

[18] The THESEUS space mission: science goals, requirements and mission concept, L. Amati, et al., 2021, Experimental Astronomy, Volume 52, Issue 3, p.183-218, DOI: 10.1007/s10686-021-09807-8, arXiv:2104.09531

[19] BATSE observations of gamma-ray burst spectra. I - Spectral diversity, D. Band, et al., 1993, Astrophysical Journal, Volume 413, pp. 281–292, DOI: 10.1086/172995

[20] A Comprehensive Analysis of Fermi Gamma-ray Burst Data. I. Spectral Components and the Possible Physical Origins of LAT/GBM GRBs, B.-B. Zhang, et al., 2011, The Astrophysical Journal, Volume 730, Issue 2, article id. 141, 33 pp, DOI: 10.1088/0004-637X/730/2/141, arXiv:1009.3338

[21] Detection of a Spectral Break in the Extra Hard Component of GRB 090926A, M. Ackerman et al., 2011, The Astrophysical Journal, Volume 729, Issue 2, article id. 114, 12 pp., DOI: 10.1088/0004-637X/729/2/114, arXiv:eprint arXiv:1101.2082

[22] The Bright and the Slow – GRBs 100724B & 160509A with high-energy cutoffs at $\lesssim$ 100 MeV, G. Vianello, et al., 2018, The Astrophysical Journal, Volume 864, Issue 2, article id. 163, 26 pp., DOI:10.3847/1538-4357/aad6ea, arXiv:1706.01481

[23] Detection of Low-energy Breaks in Gamma-Ray Burst Prompt Emission Spectra, G. Oganesyan et al., 2017, The Astrophysical Journal, Volume 846, Issue 2, article id. 137, 22 pp., arXiv:1709.04689, DOI: 10.3847/1538-4357/aa831e

[24] An Analysis of Gamma-Ray Burst Spectral Break Models, B. Zhang and P Mészáros, 2002, The Astrophysical Journal, Volume 581, Issue 2, pp. 1236-1247, DOI: 10.1086/344338, arXiv:astro-ph/0206158

[25] The Physics of Gamma-Ray Bursts and Relativistic Jets, P. Kumar et al., 2015, Physics Reports, Volume 561, p. 1-109, DOI: 10.1016/j.physrep.2014.09.008, arXiv:1410.0679

[26] Hubble Space Telescope Observations of Short GRB Host Galaxies: Morphologies, Offsets, and Local Environments, W. Fong, et al., 2010, The Astrophysical Journal, Volume 708, Issue 1, pp. 9-25, DOI: 10.1088/0004-637X/708/1/9, arXiv:0909.1804

[27] An enigmatic long-lasting gamma-ray burst not accompanied by a bright supernova, M. Della Valle, et al., 2006, Nature, Volume 444, Issue 7122, p. 1050-1052, DOI: 10.1038/nature05374, arXiv:astro-ph/0608322

[28] To be short or long is not the question, L. Amati, 2021, Nature Astronomy, Volume 5, p. 877-878, DOI: 10.1038/s41550-021-01401-4, arXiv:2111.13379

[29] Multi-messenger Observations of a Binary Neutron Star Merger, B. P. Abbott, et al., 2017, The Astrophysical Journal Letters, Volume 848, Issue 2, article id. L12, 59 pp., DOI: 10.3847/2041-8213/aa91c9, arXiv:1710.05833

[30] The SpIRIT mission: Multiwavelength detection and follow-up of cosmic explosions with an Australian space telescope, K. Auchettl, et al., 2022, Bulletin of the AAS, Volume 54, Issue 3, https://baas.aas.org/pub/2022n3i305p02

[31] Payload Design Description Report of HERMES, Y. Evangelista, et al., 2022

[32] A pulse shape discrimination gamma-ray detector based on a silicon drift chamber coupled to a CsI(Tl) scintillator: prospects for a 1 keV-1 MeV monolithic detector, M. Marisaldi, et al., 2004, IEEE Transactions on Nuclear Science, Volume 51, Issue 4, p. 1916 - 1922, DOI: 10.1109/TNS.2004.832679

[33] A broad energy range wide field monitor for next generation gamma-ray burst experiments, M. Marisaldi, et al., 2008, Nuclear Instruments and Methods in Physics Research Section A, Volume 588, Issue 1-2, p. 37-40, DOI: 10.1016/j.nima.2008.01.053

[34] Semiconductor drift chamber—An application of a novel charge transport scheme, E. Gatti and P. Rehak, 1984, Nuclear Instruments and Methods in Physics Research, Volume 225, Issue 3, p. 608-614, DOI: 10.1016/0167-5087(84)90113-3

[35] X-/γ-Ray Detection Instrument for the HERMES Nano-Satellites Based on SDDs Read-Out by the LYRA Mixed-Signal ASIC Chipset, M. Grassi, et al., 2020, 2020 IEEE International Instrumentation and Measurement Technology Conference (I2MTC), DOI: 10.1109/I2MTC43012.2020.9129520

[36] VEGA: A low-power front-end ASIC for large area multi-linear X-ray silicon drift detectors: Design and experimental characterization M. Ahangarianabhariab, et al., 2015, Nuclear Instruments and Methods in Physics Research, A, Volume 770, p. 155-163, DOI: 10.1016/j.nima.2014.10.009

[37] Evaluation of GAGG:Ce scintillators for future space applications, M. Yoneyama, et al., 2018, Journal of Instrumentation, Volume 13, Issue 2, pp. P02023, DOI: 10.1088/1748-0221/13/02/P02023

[38] Space applications of GAGG:Ce scintillators: a study of afterglow emission by proton irradiation, G. Dilillo, et al., 2022, Nuclear Instruments and Methods in Physics Research, B, Volume 513, p. 33-43, DOI: 10.1016/j.nimb.2021.12.006, arXiv:2112.02897

[39] Photomultiplier tubes and assemblies for scintillation counting and high energy physics, Hamamatsu, 2017, https://www.hamamatsu.com/content/dam/hamamatsu-photonics/sites/documents/99_SALES_LIBRARY/etd/High_energy_PMT_TPMZ0003E.pdf (last visited on 30/01/2023)

[40] 4-Channel Fast Interface Bipolar Picoammeter with Integrated Voltage Bias Source, User's Manual, CAEN ELS s.r.l., 2022,

https://www.caenels.com/wp-content/uploads/2015/04/TetrAMM_UsersManual_v2.2.pdf (last visited on 30/01/2023)

[41] Study for a passive scattering line dedicated to radiobiology experiments at the Trento Proton Therapy Center, F. Tommasino et al., 2019, Radiation Protection Dosimetry, Volume 183, Issue 1-2, p. 274–279, DOI:10.1093/rpd/ncy238

[42] Radiation Detection and Measurement, fourth ed., G.F. Knoll, 2010, John Wiley and Sons, ISBN: 978-0-470-13148-0

[43] An explanation of the power-law decay of luminescence, D. J. Huntley, 2006, Journal of Physics: Condensed Matter, Volume 18, Issue 4, p. 1359-1365, DOI: 10.1088/0953-8984/18/4/020.

[44] Irradiation studies of a multi-doped GdAlGaO12 scintillator, V.Alenkov, et al., 2018, Nuclear Instruments and Methods in Physics Research, A, Volume 916, p. 226-229, DOI: 10.1016/j.nima.2018.11.101

[45] Observation of high intensity radiation by satellites 1958 alpha and gamma, J. A. Van Allen, et al., 1958, Journal of Jet Propulsion, Volume 28, Number 9, p. 588–592, DOI: 10.2514/8.7396

[46] The South Atlantic Anomaly: The Key for a Possible Geomagnetic Reversal, F. J. Pavón-Carrasco and A. De Santis, Frontiers in Earth Science, Volume 4, id.40, DOI: 10.3389/feart.2016.00040

[47] AE9, AP9 and SPM: New Models for Specifying the Trapped Energetic Particle and Space Plasma Environment, G. P. Ginet, et al., 2013, Space Science Reviews, Volume 179, Issue 1-4, p. 579-615, DOI: 10.1007/s11214-013-9964y

[48] A comparison of trapped particle models in low earth orbit, J. Řípa, et al., 2020, Proceedings of the SPIE, Volume 11444, id. 114443P, 10 pp., DOI: 10.1117/12.2561011, arXiv:2101.03090

[49] Calibration of the first detector flight models for the HERMES constellation and the SpIRIT mission, R. Campana, et al., 2022, Proceedings of SPIE, Space Telescopes and Instrumentation 2022: Ultraviolet to Gamma Ray, Volume 12181, 121815K, DOI: 10.1117/12.2629031, arXiv:2210.13860

[50] Electron–hole pair creation energy and Fano factor temperature dependence in silicon, M. N. Mazziotta, 2008, Nuclear Instruments and Methods in Physics Research, A, Volume 584, Issues 2–3, p. 436-439, DOI: 10.1016/j.nima.2007.10.043

[51] On-ground calibrations of the GRID-02 gamma-ray detector, H. Gao, et al., 2022, Experimental Astronomy, Volume 53, Issue 1, p. 103–116, DOI: 10.1007/s10686-021-09819-4, arXiv:2109.00669

[52] Gamma-ray bursts have millisecond variability K. C. Walker, et al., 2000, The Astrophysical Journal, Volume 537, Issue 1, p. 264-269, DOI: 10.1086/308995

[53] Zur Theorie der orthogonalen Funktionensysteme, A. Haar, 1910, Mathematische Annalen, Volume 69, p. 331–371, DOI:10.1007/BF01456326

[54] Non-decimated Wavelet Transform for a Shift-invariant Analysis, G.O.N. Brassarote, et al., 2018, TEMA (São Carlos), Volume 19, Number 1, p. 93-110, DOI:10.5540/tema.2018.019.01.93

[55] Minimum variability time-scales of long and short GRBs, G. A. MacLachlan, et al., 2013, Monthly Notices of the Royal Astronomical Society, Volume 432, Issue 2, p. 857-865, DOI: 10.1093/mnras/stt241, arXiv:1201.4431

[56] Uncovering the intrinsic variability of gamma-ray bursts, V. Z. Golkhou and N. R. Butler, 2014, The Astrophysical Journal, Volume 787, Issue 1, article id. 90, 9 pp., DOI: 10.1088/0004-637X/787/1/90, arXiv:1403.4254

[57] The energy-dependence of GRB minimum variability timescales, V. Z. Golkhou, et al., 2015, The Astrophysical Journal, Volume 811, Issue 2, article id. 93, 11 pp., DOI: 10.1088/0004-637X/811/2/93, arXiv:1501.05948

[58] GRB minimum variability timescale with Insight-HXMT and Swift. Implications for progenitor models, dissipation physics, and GRB classifications, A. E. Camisasca et al., 2023, Astronomy and Astrophysics, Volume 671, id.A112, 18 pp., DOI: 10.1051/0004-6361/202245657, arXiv:2301.01176

[59] Nonparametric Estimation of Gamma-Ray Burst Intensities Using Haar Wavelets, Eric D. Kolaczyk, 1997, The Astrophysical Journal, Volume 483, Issue 1, p. 340-349, DOI: 10.1086/304243

[60] The Fermi Gamma-Ray Burst Monitor, C. Meegan, et al., 2009, The Astrophysical Journal, Volume 702, Number 1, p. 791-804, DOI: 10.1088/0004-637X/702/1/791, arXiv:0908.0450

[61] Gamma-Ray Burst Peak Duration as a Function of Energy, E. E. Fenimore, et al., 1995, Astrophysical Journal Letters, Volume 448, pp. L101, DOI: 10.1086/309603, arXiv:astro-ph/9504075

[62] Prompt and Delayed Emission Properties of Gamma-Ray Bursts Observed with BeppoSAX, F. Frontera, et al., 2000, The Astrophysical Journal Supplement Series, Volume 127, Issue 1, p. 59-78, DOI: 10.1086/313316, arXiv:astro-ph/9911228

[63] `https://user-web.icecube.wisc.edu/~grbweb_public/Summary_table.html` (last visited 25/01/2023)

[64] Detection of the high z GRB 080913 and its implications on progenitors and energy extraction mechanisms, D. Perez-Ramirez, et al., 2010, Astronomy and Astrophysics, Volume 510, id.A105, 6 pp., DOI: 10.1051/0004-6361/200811151, arXiv:0810.2107

[65] GRB 080913 at Redshift 6.7, J. Grenier, et al., 2009, The Astrophysical Journal, Volume 693, Issue 2, p. 1610-1620, DOI: 10.1088/0004-637X/693/2/1610, arXiv:0810.2314

[66] GRB090423 at a redshift of z 8.1, R. Salvaterra, et al., 2009, Nature, Volume 461, Issue 7268, p. 1258-1260, DOI: 10.1038/nature08445, arXiv:0906.1578

[67] Intrinsic spectra and energetics of BeppoSAX Gamma–Ray Bursts with known redshifts, L. Amati, et al., 2002, Astronomy and Astrophysics, Volume 390, Number 1, p. 81-89, DOI: 10.1051/0004-6361:20020722, arXiv:astro-ph/0205230

[68] Gamma-ray Bursts, Classified Physically, J. S. Bloom, et al., 2008, GAMMA-RAY BURSTS 2007: Proceedings of the Santa Fe Conference. AIP Conference Proceedings, Volume 1000, p. 11-15, DOI: 10.1063/1.2943423, arXiv:0804.0965

[69] Statistical classification of gamma-ray bursts based on the Amati relation, Yi-Ping Qin, Zhi-Fu Chen, 2013, Monthly Notices of the Royal Astronomical Society, Volume 430, Issue 1, p. 163–173, DOI:10.1093/mnras/sts547, arXiv:1311.4713

[70] The Collimation-corrected Gamma-Ray Burst Energies Correlate with the Peak Energy of Their νF_ν Spectrum, G. Ghirlanda, et al., 2004, The Astrophysical Journal, Volume 616, Number 1, DOI: 10.1086/424913, arXiv:astro-ph/0405602

[71] Redshifts For 220 BATSE Gamma-Ray Bursts Determined by Variability and the Cosmological Consequences, E. E. Fenimore and E. Ramirez-Ruiz, 2000, DOI: 10.48550/arXiv.astro-ph/0004176, arXiv:astro-ph/0004176

[72] A Possible Cepheid-like Luminosity Estimator for the Long Gamma-Ray Bursts, Daniel E. Reichart, et al., 2001, The Astrophysical Journal, Volume 552, Issue 1, p. 57-71, DOI: 10.1086/320434, arXiv:astro-ph/0004302

[73] The slope of the GRB Variability/Peak Luminosity Correlation, C. Guidorzi, et al., 2006, Monthly Notices of the Royal Astronomical Society, Volume 371, Issue 2, p. 843–851, DOI: 10.1111/j.1365-2966.2006.10717.x, arXiv:astro-ph/0606526